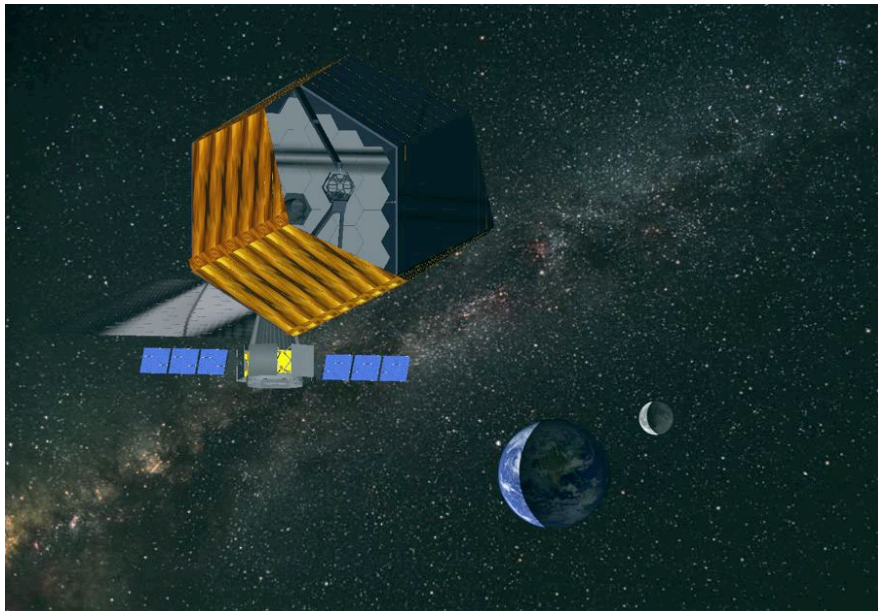


# ADVANCED TECHNOLOGY LARGE-APERTURE SPACE TELESCOPE (ATLAST): A TECHNOLOGY ROADMAP FOR THE NEXT DECADE

A NASA Astrophysics Strategic Mission Concept Study

May 2009

Dr. Marc Postman, Principal Investigator  
Space Telescope Science Institute



## Co-Investigators

Vic Argabright<sup>1</sup>, Bill Arnold<sup>11</sup>, David Aronstein<sup>3</sup>, Paul Atcheson<sup>1</sup>, Morley Blouke<sup>1</sup>, Tom Brown<sup>4</sup>, Daniela Calzetti<sup>5</sup>, Webster Cash<sup>6</sup>, Mark Clampin<sup>3</sup>, Dave Content<sup>3</sup>, Dean Dailey<sup>7</sup>, Rolf Danner<sup>7</sup>, Rodger Doxsey<sup>4</sup>, Dennis Ebbets<sup>1</sup>, Peter Eisenhardt<sup>8</sup>, Lee Feinberg<sup>3</sup>, Ed Freymiller<sup>1</sup>, Andrew Fruchter<sup>4</sup>, Mauro Giavalisco<sup>5</sup>, Tiffany Glassman<sup>7</sup>, Qian Gong<sup>3</sup>, James Green<sup>6</sup>, John Grunsfeld<sup>9</sup>, Ted Gull<sup>3</sup>, Greg Hickey<sup>8</sup>, Randall Hopkins<sup>2</sup>, John Hraba<sup>2</sup>, Tupper Hyde<sup>3</sup>, Ian Jordan<sup>4</sup>, Jeremy Kasdin<sup>10</sup>, Steve Kendrick<sup>1</sup>, Steve Kilston<sup>1</sup>, Anton Koekemoer<sup>4</sup>, Bob Korechoff<sup>8</sup>, John Krist<sup>8</sup>, John Mather<sup>3</sup>, Chuck Lillie<sup>7</sup>, Amy Lo<sup>7</sup>, Rick Lyon<sup>3</sup>, Scot McArthur<sup>1</sup>, Peter McCullough<sup>4</sup>, Gary Mosier<sup>3</sup>, Matt Mountain<sup>4</sup>, Bill Oegerle<sup>3</sup>, Bert Pasquale<sup>3</sup>, Lloyd Purves<sup>3</sup>, Cecelia Penera<sup>7</sup>, Ron Polidan<sup>7</sup>, Dave Redding<sup>8</sup>, Kailash Sahu<sup>4</sup>, Babak Saif<sup>4</sup>, Ken Sembach<sup>4</sup>, Mike Shull<sup>6</sup>, Scott Smith<sup>2</sup>, George Sonneborn<sup>3</sup>, David Spergel<sup>10</sup>, Phil Stahl<sup>2</sup>, Karl Stapelfeldt<sup>8</sup>, Harley Thronson<sup>3</sup>, Gary Thronson<sup>2</sup>, Jackie Townsend<sup>3</sup>, Wesley Traub<sup>8</sup>, Steve Unwin<sup>8</sup>, Jeff Valenti<sup>4</sup>, Robert Vanderbei<sup>10</sup>, Penny Warren<sup>1</sup>, Michael Werner<sup>8</sup>, Richard Wesenberg<sup>3</sup>, Jennifer Wiseman<sup>3</sup>, Bruce Woodgate<sup>3</sup>

### AFFILIATION CODES:

1 = Ball Aerospace & Technologies Corp.

3 = Goddard Space Flight Center

5 = Univ. Massachusetts, Amherst

7 = Northrop Grumman Aerospace Systems

9 = Johnson Space Flight Center

2 = Marshall Space Flight Center

4 = Space Telescope Science Institute

6 = University of Colorado, Boulder

8 = Jet Propulsion Laboratory, California Institute of Technology

10 = Princeton University

11 = Jacobs ESTS Group @ MSFC

## TABLE OF CONTENTS

Executive Summary .....	4
1. Scientific Motivations for <i>ATLAST</i> .....	5
1.1) Does Life Exist Elsewhere in the Galaxy?.....	5
1.2) Exploration of the Modern Universe .....	7
1.3) Constraining Dark Matter.....	9
2. ATLAST Technical Overview .....	10
2.1) 8-meter Monolithic Mirror Telescope.....	11
2.2) Segmented Mirror Telescope Options .....	12
3. Top Three <i>ATLAST</i> Technology Drivers.....	15
4. Summary of the <i>ATLAST</i> Technology Development Plan.....	18
4.1) ATLAST Mission Life Cycle Cost Estimates .....	21
Acknowledgements.....	22
Appendix A: Table of Acronym Definitions.....	23
Appendix B: Synergy with Other Astronomical Facilities .....	24
Appendix C. Summary of the <i>ATLAST-8m</i> Engineering Team Study.....	25
Appendix D. <i>ATLAST-8m</i> Thermal Analysis .....	26
Appendix E: Solar Torque Mitigation Systems for <i>ATLAST-16m</i> .....	30
Appendix F. Optical Design and Active Optics System for the <i>ATLAST-16m</i> Concept .....	34
Basic Optical Design.....	34
Active Optics System.....	36
Active Optics Architecture .....	37
Wavefront Sensing and Control: Initialization and Updates .....	40
Wavefront Maintenance Control .....	42
Wavefront Error Budget for ATLAST-16m.....	46
Appendix G: Summary of <i>ATLAST-9.2m</i> Design Study.....	49
Appendix H: Actuated Hybrid Mirrors.....	50
Appendix I: <i>ATLAST</i> Gigapixel Camera: Focal Plane Packaging and Electronics.....	53
Appendix J: Summary of Visible Light Detector Technologies for <i>ATLAST</i> .....	57
Requirements of the ATLAST Focal Plane Array.....	57
Detector Architectures.....	58
Conventional CCDs.....	59
e2v L3CCD™ .....	62
“Impactron” from Texas Instruments.....	68
CMOS Arrays .....	71
P-channel, Fully-depleted CCDs.....	73
Future Work.....	76
Summary of Technologies.....	76
Appendix K: Evaluation of Coronagraphic Techniques for <i>ATLAST</i> .....	80
Classical Lyot coronagraphs (amplitude focal plane masks) .....	80
Multi-stage Lyot coronagraphs.....	83
Lyot coronagraphs with focal plane phase masks .....	83
Pupil apodization .....	84
Phase modification in the pupil .....	85
Shaped Pupils.....	85

Off-axis vs. On-axis Lyot Coronagraphy and a Comparison to the VNC Performance with a Segmented Telescope.....	87
Appendix L: <i>ATLAST</i> Starshade Design and Technology .....	93
Starshade Sizing.....	93
Starshade Orbits.....	95
Starshade Targeting Efficiency.....	96
Starshade Fuel Consumption Considerations .....	97
Starshade Launch Vehicle Requirements.....	97
Appendix M: Exoplanet Science with <i>ATLAST</i> 8-m and 16-m Concepts .....	99
Appendix N: <i>ATLAST</i> Communications and Telemetry Considerations.....	103
Appendix O: Servicing Benefits for <i>ATLAST</i> .....	107
References .....	108

## Executive Summary

For four centuries new technology and telescopes of increasing diameter have driven astronomical discovery for the simple reason that astronomy is a photon-limited field. The *Hubble Space Telescope (HST)*, to date the largest UV/optical astronomical space telescope, has demonstrated the breadth of fundamental astrophysics that can be extracted from space-based observations in the UV-optical-near IR. *HST's* versatility has allowed it to be used to make pioneering discoveries in fields never envisioned by its builders. The paradigm-shifting discoveries in the next two decades will be made with ever more capable instruments and facilities. Here we outline the technology developments and mission concepts required for the next step – a highly versatile UV-optical-near IR observatory in space, larger and more capable than either *HST* or its IR-optimized successor, the *James Webb Space Telescope (JWST)*. Although substantial investments are required for the next steps, the basic technologies needed either already exist or we understand the path forward, allowing us to construct schedules, budgets, and the main decision points.

The **Advanced Technology Large-Aperture Space Telescope (ATLAST)** is a set of mission concepts for the next generation of UVOIR space observatory with a primary aperture diameter in the 8-m to 16-m range that will allow us to perform some of the most challenging observations to answer some of our most compelling questions, including “Is there life elsewhere in the Galaxy?” We have identified two different telescope architectures, but with similar optical designs, that span the range in viable technologies. The architectures are a telescope with a monolithic primary mirror and two variations of a telescope with a large segmented primary mirror. This approach provides us with several pathways to realizing the mission, which will be narrowed to one as our technology development progresses. The concepts invoke heritage from *HST* and *JWST* design, but also take significant departures from these designs to minimize complexity, mass, or both.

Our report provides details on the mission concepts, shows the extraordinary scientific progress they would enable, and describes the most important technology development items. These include the mirrors, the wavefront sensing and control system, the starlight suppression system (for exoplanet observations and other high-contrast imaging applications), and the detectors. Experience with *JWST* has shown that determined competitors, motivated by the development contracts and flight opportunities of the new observatory, are capable of achieving huge advances in technical and operational performance while keeping construction costs on the same scale as prior great observatories.

The main body of this report consists of sections 1 through 4. These 18 pages provide a concise summary the critical findings and results of our study. *Complete details on many of the investigations performed during this study are provided in the appendices that follow these initial sections.* Three of the sub-reports are substantial in length and are, thus, provided as separate volumes on-line. These three separate volumes are 1) our detailed technology development plan for *ATLAST*, 2) a summary of the *ATLAST-8m* engineering and design study, and 3) a summary of the *ATLAST-9.2m* engineering and design study. To access these additional volumes, go to <http://www.stsci.edu/institute/atlast> and click on “*ATLAST* Mission Concept Study.”

## 1. Scientific Motivations for *ATLAST*

Conceptual breakthroughs in understanding astrophysical phenomena happen when our observatories allow us to detect and characterize faint structure and spectral features on the relevant angular scales. By virtue of its  $\sim 12$  milli-arcsecond angular resolution at  $\sim 500$  nm coupled with its ultra high sensitivity, superb stability and low sky background, *ATLAST* will make these breakthroughs – both on its own and in combination with other telescopes with different capabilities. *ATLAST* has the performance required to detect the potentially rare occurrence of biosignatures in the spectra of terrestrial exoplanets, to reveal the underlying physics that drives star formation, and to trace the complex interactions between dark matter, galaxies, and the intergalactic medium. Because of the large leap in observing capabilities that *ATLAST* will provide, we cannot fully anticipate the diversity or direction of the investigations that will dominate its use – just as the creators of *HST* did not foresee its pioneering roles in characterizing the atmospheres of Jupiter-mass exoplanets or measuring the acceleration of cosmic expansion using distant supernovae. It is, thus, essential to ensure *ATLAST* has the versatility to far outlast the vision of current-day astronomers. We discuss briefly a small subset of the key scientific motivations for *ATLAST* that we can conceive of today.

### 1.1) Does Life Exist Elsewhere in the Galaxy?

We are at the brink of answering two paradigm-changing questions: *Do other planets like Earth exist? Do any of them harbor life?* The tools for answering the first question already exist (e.g., *Kepler*); those that can address the second can be developed within the next 10-20 years [1]. ***ATLAST* is our best option for an extrasolar life-finding facility** and is consistent with the long-range strategy for space-based initiatives recommended by the Exoplanet Task Force [2]. *ATLAST* has the angular resolution and sensitivity to characterize the atmosphere and surface of an Earth-sized exoplanet in the Habitable Zone (HZ) at distances up to  $\sim 45$  pc, including its rotation rate, climate, and habitability. These expectations are based on our simulated exoplanet observing programs using the known stars, space telescopes with aperture diameters ranging from 2 m to 16 m, and realistic sets of instrumental performance parameters and background levels.

We start by selecting spectral type F,G,K stars from the Hipparcos catalog and identify, for each telescope aperture,  $D$ , those stars whose HZ exceeds an inner working angle (IWA) of  $3\lambda/D$  at 760 nm (the  $O_2$  absorption feature). As a detection goal, we assume that each star has an Earth-twin in its HZ (with  $\Delta mag = 25$ ), realizing that super Earths will be easier targets. We include plausible instrumental efficiencies and noise properties, and assume a 3-zodi background (local plus exosolar). We assume that our starlight suppression system (either internal coronagraph or external occulter) is capable of achieving a suppression of at least 25 mags ( $10^{-10}$ ) and include residual background from the star as an additional noise source. We then compute the number of stars for which an  $R=70$  spectrum with signal-to-noise

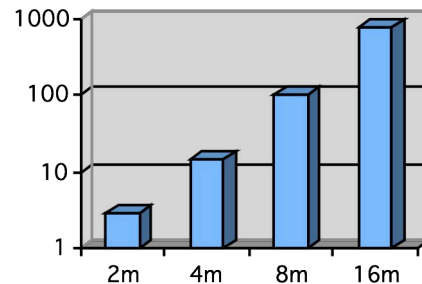


**Figure 1.** The average number of F,G,K stars where  $SNR=10$   $R=70$  spectrum of an Earth-twin *could* be obtained in  $< 500$  msec as a function of telescope aperture,  $D$ . The growth in the sample size scales as  $D^3$ .

ratio (SNR) of 10 at 760 nm could be acquired in 500 msec or less. The results, averaged over different simulations done using various starlight suppression options (internal coronagraphs of various kinds as well as an external occulter), are shown in Figure 1. To estimate the number of potentially inhabited worlds detected, one must multiply the numbers in Figure 1 by the fraction of the FGK stars that have an Earth-sized planet in their HZ ( $\eta_{\oplus}$ ) and also by the fraction of those exo-Earths that have detectable biosignatures. The values of these fractions are currently not constrained but their product is not likely to be close to unity. One must conclude that **to maximize the chance for a successful search for life in the solar neighborhood requires a space telescope with an aperture size of at least 8 meters.**

Estimates of the SNR of habitability and biosignature features in an Earth-twin spectrum, achievable with *ATLAST*, are shown in Table 1. For these calculations we use a fully validated model of the Earth's spectrum [3,4], in combination with the observed visible reflection spectrum of the present Earth. We assume that the exoplanet is at maximum elongation and that the planet is observed for a length of time sufficient to achieve an SNR of 10, at a spectral resolution  $R = 70$ , in the red continuum. The Rayleigh (air column) signal is the blue enhanced albedo from atmospheric molecules. The  $O_3$  and  $O_2$  signals are biosignatures. The cloud/surface signal around 750 nm will vary with time as the planet rotates, and is therefore a rotation signature. The vegetation signal is the enhanced albedo of the Earth, from land plants, for wavelengths longer than  $\sim 720$  nm [5], with a modest SNR. The  $H_2O$  signal is a prime habitability indicator. Column 3 gives the width of the spectral feature. All of these SNR values can easily be improved with re-visits. In addition, *ATLAST* will allow us to glean substantial information about an exo-Earth from temporal variations in its features. Such variations inform us about the nature of the dominant surface features, changes in climate, changes in cloud cover (weather), and, potentially, seasonal variations in surface vegetation [6]. Constraints on variability require multiple visits to each target. **The 8-m *ATLAST* (with internal coronagraph) will be able to observe  $\sim 100$  different star systems 3 times each in a 5-year interval and not exceed 20% of the total observing time available to the community. The 16-m version (with internal coronagraph) could visit up to  $\sim 250$  different stars 3 times each in a 5-year period. The 8-m or 16-m *ATLAST* (with a single external occulter) can observe  $\sim 85$  stars 3 times each in a 5-year period, limited by the transit times of the occulter.** Employing multiple occulters would remove this limitation.

**Table 1: Habitability and Bio-Signature Characteristics**

Feature	$\lambda$ (nm)	$\Delta\lambda$ (nm)	SNR	Significance
Reference continuum	$\sim 750$	11	10	
Air column	500	100	4	Protective atmosphere
Ozone ( $O_3$ )	580	100	5	Source is oxygen; UV shield
Oxygen ( $O_2$ )	760	11	5	Plants produce, animals breathe
Cloud/surface reflection	750	100	30	Rotation signature
Land plant reflection	770	100	2	Vegetated land area
Water vapor ( $H_2O$ )	940	60	16	Needed for life

With *ATLAST*, we will be able to determine if HZ exoplanets are indeed habitable, and if they show signs of life as evidenced by the presence of oxygen, water, and ozone. *ATLAST* also will provide useful information on the column abundance of the atmosphere, the presence of continents and oceans, the rotation period, and the degree of daily large-scale weather variations.

## 1.2) Exploration of the Modern Universe

We know that galaxies form and evolve but we know little about how this happens. The physical processes involve complex interactions between the baryonic matter in the galaxies, the energy exchanged during the birth and death of stars, the gas outside the galaxies in the intergalactic medium (IGM), other neighboring galaxies, and the dark matter that dominates and shapes the underlying gravitational potential. Revealing the physics behind galaxy formation and evolution requires making a broad array of observations from the current epoch to the epoch of the first stars. *ATLAST* will provide many of the key pieces needed to solve this puzzle, particularly in the redshift range  $z < 4$  when the cosmic star formation rate peaks and then fades, and galaxies develop their current morphologies.

***ATLAST* will enable extensive probes of the local IGM in the UV, revealing the nature of its interaction with galaxies.** Understanding how gas in the IGM gets into galaxies and how galaxies respond to inflow lies at the heart of understanding galactic evolution. The mode of accretion depends on the depth of the potential well (galaxy type) and the location at which the intergalactic gas is shocked as it encounters that potential [7,8]. Depending on the mass of the galaxy halo, the infalling gas may be shocked and heated or accrete in “cold mode” along narrow filaments. Gas can also be removed from galaxies via tidal and ram pressure stripping, or during the accretion of gas-rich dwarfs onto giant galaxies. Metal-enriched gas introduced into the IGM by these processes will be dynamically cool.

All of these accretion and gas removal theories have observational consequences (e.g., Fig. 2) that can be tested if the distribution of gas in the cosmic web around galaxies can be characterized through absorption and emission line spectroscopy. The observational challenge is to acquire datasets of sufficient sample size and with enough diagnostic power (**i.e., spectral resolution**) to identify and characterize the various processes at work. The number of suitable background sources available for absorption line measurements is presently limited by the sensitivity of current instrumentation (*HST/COS*).

*ATLAST*'s dramatically increased absorption line sensitivity at UV and optical wavelengths is crucial for reaching the required background source densities. There are  $\sim 100$  quasars per square degree that are brighter than a *GALEX* flux of  $m_{\text{FUV}} \sim 24$  [10]. At this sampling, one can select sight lines next to thousands of examples of any common galaxy, group, or cluster. *ATLAST* could then be used to produce a high-resolution map of the gas and metals surrounding these structures, which could be used to compare directly against simulation predictions [11,12]. With *ATLAST* one could also use multiple quasars *and* distant galaxies as background continuum sources to dissect the gas distribution in fields known to have galaxies and gas at the same redshift [13]. *ATLAST*'s large aperture will enable contiguous regions of  $\sim 10$  Mpc on a side (like in Fig. 2) to be surveyed in about 2 weeks of exposure time (with an 8-m *ATLAST* with enhanced UV detectors) or in  $\sim 3$  days (with a 16-m *ATLAST* with enhanced UV detectors) [14]. *ATLAST* could also be used systematically to target individual nearby galactic

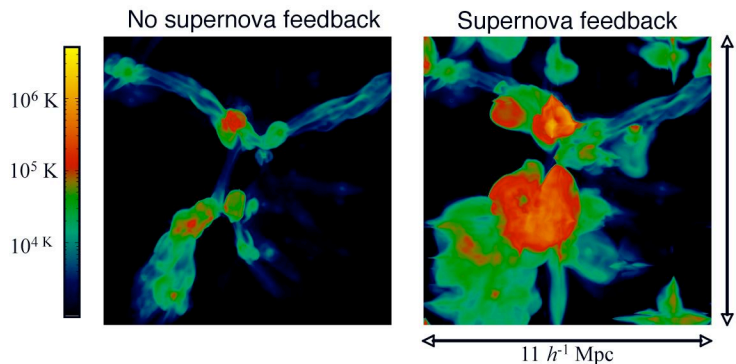


**Figure 2.** IGM gas temperature distribution for cosmological models with and without supernova feedback [9].

coronae and groups of galaxies, for which it would be possible to observe the production sites of heavy elements (star-forming regions, SNe, emission nebulae), follow the processes by which the elements are transported within galaxies, and trace the expulsion of metals into the IGM.

Determining whether the stellar initial mass function (IMF) is universal or environment-dependent places further stringent constraints on the evolution of the baryonic component of galaxies. *ATLAST* will uniquely be able to measure the IMF down to  $1 M_{\text{SUN}}$  out to 10 Mpc over the full range of star forming environments (which are outside the range of *HST* and *JWST*), including environments similar to those found in high redshift galaxies. This will yield fundamental predictions for a comprehensive theory of star formation [15].

***ATLAST* will, for the first time, enable star formation histories to be reconstructed for hundreds of galaxies beyond the Local Group, opening the full range of star formation environments to exploration.** A comprehensive and predictive theory of galaxy formation and evolution requires that we accurately determine how and when galaxies assemble their stellar populations, and how this assembly varies with environment. By definition the dwarf galaxies we see today are not the same as the dwarf galaxies and proto-galaxies that were disrupted during assembly. Our only insight into those disrupted building blocks comes from sifting through the resolved field populations of the surviving giant galaxies to reconstruct the star formation history, chemical evolution, and kinematics of their various structures [16]. **Resolved stellar populations are cosmic clocks.** Their most direct and accurate age diagnostic comes from

resolving both the dwarf and giant stars, including the main sequence turnoff. But the main sequence turnoff rapidly becomes too faint to detect with any existing telescope for any galaxy beyond the Local Group. This greatly limits our ability to infer much about the details of galactic assembly because the galaxies in the Local Group are not representative of the galaxy population at large. *ATLAST* will allow us to reach well beyond the Local Group as shown in Figure 3. *HST* and *JWST* cannot reach any large galaxies besides our Milky Way and M31 (see Figure 3). An 8-meter space telescope can reach 140 galaxies including 12 giant spirals and the nearest giant elliptical. A 16-meter space telescope extends our reach to the Coma Sculptor Cloud, netting a total of 370 galaxies including 45 giant spirals and 6 ellipticals. Deriving ages and other galactic properties from color-magnitude data requires photometry for thousands of stars spanning 4 orders of magnitude in luminosity. **This implies the need for a wide-field imager on *ATLAST* with half-Nyquist sampling over a field of view of at least 4 arcminutes.** *ATLAST* will work in concert with 30m-class ground-based telescopes (e.g., *TMT*), expanding our reach to other well-populated galaxy groups, with *ATLAST* obtaining photometry of  $V \sim 35$  magnitude G dwarf stars and *TMT* obtaining kinematics of much brighter giants out to the Coma Sculptor Cloud. The dwarf stars in the Coma Sculptor Cloud are effectively inaccessible to *TMT*, requiring gigaseconds of integration even for an isolated star.

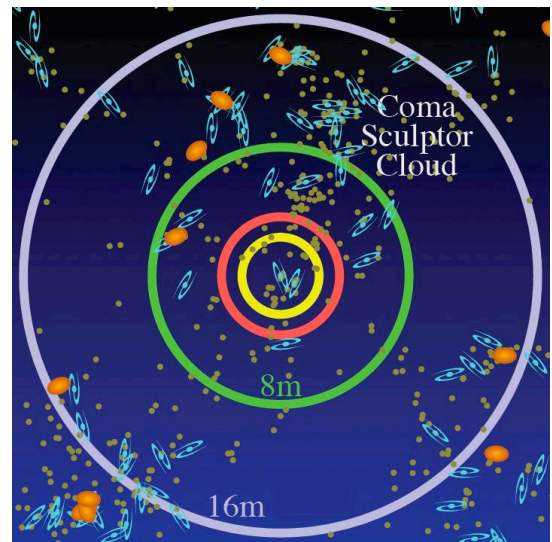


**Figure 3.** Map of local universe (24 Mpc across) shown with the distances out to which *HST* (yellow), *JWST* (orange), and *ATLAST* (8-m, 16-m), can detect solar analogs in V and I passbands at SNR=5 in 100 hours. Giant spirals, like M31, are indicated by the blue galaxy symbols, giant ellipticals as orange blobs, and dwarf galaxies as small green dots.

### 1.3) Constraining Dark Matter

Dwarf spheroidal galaxies (dSph), the faintest galaxies known, are extraordinary sites to explore the properties of non-baryonic dark matter (DM). There are several reasons for this. First, their mass is dominated by DM – they are observed to have mass-to-light ratios 10 to 100 times higher than the typical  $L^*$  galaxy, such as M31 or the Milky Way [31,32,33]. Second, they are relatively abundant nearby – to date 19 dSph galaxies have been found in the Local Group and more will be discovered. Third, and perhaps most striking, is the discovery that all nineteen dSph satellites, covering more than four orders of magnitude in luminosity, inhabit dark matter halos with the *same* mass ( $\sim 10^7 M_{\text{SUN}}$ ) within their central 300 pc [33] (see Figure 4).

The ability of DM to cluster in phase space is limited by intrinsic properties such as mass and kinetic temperature. Cold dark matter particles have negligible velocity dispersion and very large central phase-space density, resulting in cuspy density profiles. Warm dark matter halos, in contrast, have smaller central phase-space densities, so that density profiles saturate to form constant central cores. Owing to their small masses, dSphs have the highest average phase space densities of any galaxy type, and this implies that for a given DM model, phase-space limited cores will occupy a larger fraction of the virial radii. Hence, **the mean density profile of dSph galaxies is a fundamental constraint on the nature of dark matter.**

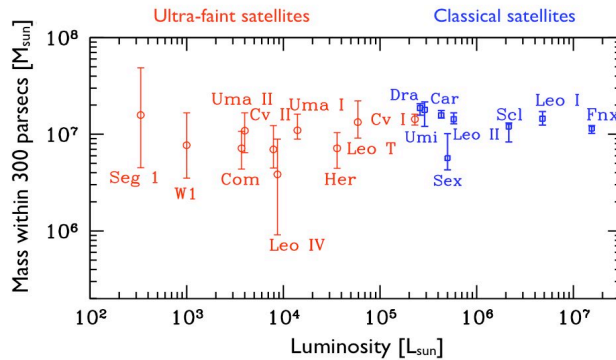


**Figure 4.** The integrated mass within the inner 300 pc of local dSph galaxies as a function of the luminosity.

Current observations are unable to measure the density profile slopes within dSph galaxies because of a strong degeneracy between the inner slope of the DM density profile and the velocity anisotropy of the stellar orbits. Radial velocities alone cannot break this degeneracy even if the present samples of radial velocities are increased to several thousand stars [34]. Combining proper motions with the radial velocities is the only robust means of breaking the anisotropy-inner slope degeneracy. The

required measurements include proper motions for  $\sim 100$  stars per galaxy with accuracies better than 10 km/sec ( $< 40 \mu\text{as/yr}$  at 60 kpc) and  $\sim 1000$  line-of-sight velocities. In the case of the brightest of these dSph galaxies, such as Fornax and Sculptor, sufficient velocities and proper motions can be obtained using stellar giants. Ground-based 8-m class telescopes could measure the spectra, and *SIM-Lite* could measure the proper motions. For the less massive dwarfs, where the dark matter dominance is the greatest, main sequence stars will have to be used to obtain the numbers of velocity and proper motion measurements needed. This will require larger (30-m class) ground-based telescopes for the velocities. The 30-m class telescopes may also be able to obtain the necessary proper motions but it will be extremely challenging: it will require precisely stitching many fields together, most of which are unlikely to contain background quasars of sufficient brightness to be useful as astrometric references. However, the necessary astrometric precision would be readily achieved with *ATLAST*, given its comparatively wide field of view and stability. ***ATLAST* will, thus, provide some of the best constraints on the nature of dark matter.**

## 2. ATLAST Technical Overview

The *ATLAST* technology development plan is based on three point designs the team developed using funding from NASA’s Astrophysics Strategic Mission Concept Study program, NASA/MSFC, NASA/GSFC, and related studies at JPL, Northrop Grumman, and Ball Aerospace. Two of the concepts, the 8-m monolithic mirror telescope (hereafter *ATLAST-8m*) and the 16.8-m segmented mirror telescope (*ATLAST-16m*), span the range of UVOIR observatories that are enabled by NASA’s proposed Ares-V launch vehicle. *ATLAST-8m* is studied because of the inherent advantages offered by a monolithic aperture telescope in terms of high-contrast imaging and wavefront error (WFE) control. *ATLAST-16m* is studied because it represents a pathway to truly large apertures in space and uses the largest extrapolation of a *JWST*-like chord-fold primary mirror packaging. However, the *ATLAST* mission is not solely dependent on Ares V. Our third concept, a 9.2-m segmented telescope (*ATLAST-9.2m*), is compatible with an Evolved Expendable Launch Vehicle (EELV) and also adopts *JWST* design heritage.

All *ATLAST* concepts require many of the same key technologies. **We believe these designs compose a robust set of options for achieving the next generation of UVOIR space observatory in the 2020 era.** Their technologies also will enable a new generation of more capable small and medium class space-based and balloon-borne observatories.

Key to the *ATLAST-8m* and *ATLAST-16m* is NASA’s proposed Ares V heavy lift launch vehicle planned for 2019. Ares V (configuration LV 51.00.48) is projected to have the ability to launch an 8.8 m diameter, ~65,000 kg payload into a Sun-Earth Lagrange point (SE-L2) transfer orbit. The current baseline Ares V shroud is a biconic fairing with a 10 m outer diameter and a height of 21.7 m. Ares V will have an 8.8-m diameter by 17.2-m tall dynamic envelope, and a payload volume of 860 cubic meters – nearly three times the volume of the Space Shuttle payload bay. NASA is considering a ‘stretch’ fairing that would measure 26 m in height, with a volume of 1410 cubic meters. Finally, a serious trade is underway to replace the biconic nose cone with an ogive-shaped structure. The ogive configuration would provide even more payload volume and useable internal vertical height [21].

**There are several fundamental features common to all our designs.** All *ATLAST* concepts are designed to operate at SE-L2. The optical designs are diffraction limited at 500 nm (36 nm RMS WFE) and the optical telescope assembly (OTA) operates near room temperature (280K – 290K). All OTAs employ two, simultaneously usable foci – a three-mirror anastigmat (TMA) channel for multiple, wide field of view (FOV) instruments, and a Cassegrain channel for high-throughput UV instruments and instruments for imaging and spectroscopy of exoplanets (all designs have RMS WFE of <5 nm at <2 arcsec radial offset from Cass optical axis).

**Table 2: Tentative ATLAST Science and Facility Instruments and their FOV**

Telescope	TMA Focal Plane Instruments				Cass Focal Plane Instruments		
	Vis/NIR Wide-field Imager	Vis/NIR Multi-Object Spectrograph	Vis/NIR IFU	FGS (FOV per FGS unit)	UV IFU & Spectrograph	Starlight Suppression	Exoplanet Imager & Spectrograph
<b>8-m, 9.2-m</b>	8x8 arcmin	4x4 arcmin	2x2 arcmin	3x3 arcmin	30 arcsec	Internal Coronagraph or Starshade Sensor	~10 arcsec
<b>16.8-m</b>	4x4 arcmin	3x3 arcmin	1x1 arcmin	~1x3 arcmin	15 arcsec		~10 arcsec

All instruments are modular and could be replaceable on orbit. Fine guidance sensors (FGS) are deployed on the TMA focal plane. Nominal designs incorporate three to four FGS units. Table 2 summarizes potential instrument suites for *ATLAST*. The WF visible/NIR imager employs a beam splitter to simultaneously send light to visible CCD (450-1000 nm) and NIR HgCdTe (1-2.5 microns) detector arrays. The CCD array requires ~1 gigapixels to permit half-Nyquist (*a.k.a.* critical) sampling at 500 nm.

Finally, all *ATLAST* concepts have propellant loads sized to provide ten years of on orbit station keeping and momentum unloading. *ATLAST* can be designed to enable on-orbit servicing to extend the mission lifetime via autonomous rendezvous and docking technology, which Orbital Express recently demonstrated. However, *ATLAST* can achieve high scientific impact without servicing. We summarize the *ATLAST* design concepts below and in Table 3.

**Table 3: Summary of *ATLAST* Point Designs**

Aperture (meters)	Wavelength Coverage	Orbit	Primary Mirror	Secondary Mirror	Pointing (mas)	Launch Vehicle	Total Mass (kg)	Total Power (kW)
<b>8.0</b>	110 – 2500 nm	SE-L2 Halo Orbit	Monolithic	On-axis or Off-axis	1.6	Ares V	~59,000	11
<b>9.2</b>			Segmented	On-axis	1.4	EELV	~15,700	5.7
<b>16.8</b>			Segmented	On-axis	0.8	Ares V	~30,000	~10

(Total Mass and Total Power values include at least a 28% contingency)

### 2.1) 8-meter Monolithic Mirror Telescope

The *ATLAST-8m* mission concept takes advantage of the volume capacity of the Ares V’s fairing to launch an 8-meter monolithic mirror. The Ares V’s enormous mass capacity significantly reduces cost and risk by allowing a simple high-mass margin high-TRL design approach. *ATLAST-8m* could be flown early in the 2020 decade.

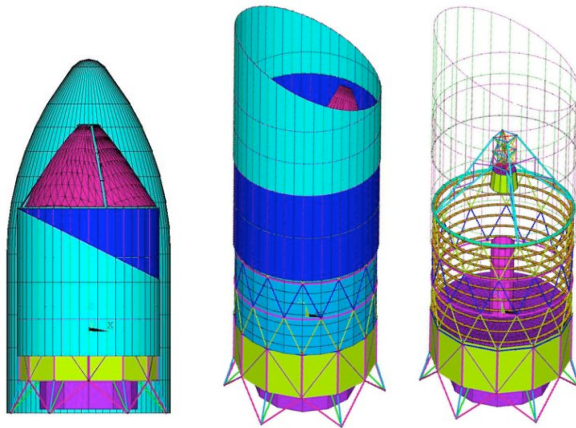


**Figure 5.** (Left) 8-m *ATLAST* in Ares V fairing. (Center) After deployment of the sunshield. (Right) Cutaway view.

*ATLAST-8m* uses a modified *HST*-style optical bench for stable primary to secondary mirror alignment. Behind the primary mirror is a 4 m diameter by 4.5 m long bay in which modular science instruments have direct access to the Cassegrain focus and **two** off-axis wide fields of view. A *Kepler*-style 60-degree scarfed sunshield provides thermal isolation, stray-light rejection and environmental protection (see Fig. 5). The sunshade stabilizes the telescope at 135K and active zonal heating raises its temperature to 280K ± 0.1K. The primary mirror’s uniform CTE, mass and thermal capacity provides a thermal figure stability of 1 nm with a 500-hour thermal time constant. *ATLAST-8m* offers exceptional

thermal stability for long-duration observations regardless of slew or roll angle.

The single most important element of *ATLAST-8m* is the primary mirror. While a *HST*-style lightweight mirror could be used with a *JWST*-class design-margin structure, the Ares V’s mass capacity allows us to reduce risk and cost by using a solid meniscus glass mirror – the kind

typically used for ground based telescopes (e.g., *Gemini*, *VLT*). In fact we propose to space qualify and launch the existing *VLT* spare or a new off-axis mirror blank. **This approach saves cost because the handling infrastructure exists and the ability to fabricate the mirror to 8 nm RMS has been demonstrated.** Facilities to fabricate lightweight 4-m to 8-m class mirrors do not exist. Additionally, *ATLAST-8m* uses large design margins, which reduce cost and risk. An iso-grid truss-structure support maintains primary mirror launch loads below 600 psi, which is well below the 7000 psi design limit for polished glass meniscus substrates. By comparison, lightweight mirrors have a design limit of only 1000 psi.

The entire observatory (telescope, science instruments and spacecraft) has an estimated dry mass of ~51,400 kg with a 45% margin against the Ares V 65,000 kg capacity (excluding the primary mirror whose mass can only decrease as material is removed). If the Ares V mass capacity were to decrease, our design mass can be reduced to maintain a minimum mass margin of 30%. The spacecraft reaction wheels are sized to provide a maximum slew rate of 0.67 deg per minute, roll rate of 0.5 deg per minute and a maximum uninterrupted observation period of 75 hours between momentum dumps. This observation time is assisted by using the 72 m<sup>2</sup> of solar panels, mounted behind the observatory on a rotary arm, as a kite tail to balance the solar radiation pressure. Body pointing the telescope using active isolation between the spacecraft and telescope achieves fine pointing stability of 1.6 mas. Four *JWST*-style ‘staring’ FGS units (two in each corner of the two TMA foci) provide pointing control, roll control and redundancy.

We also examined an off-axis monolithic telescope concept (to optimize the performance of an internal coronagraph for exoplanet observations). A 6 x 8 meter off-axis elliptical mirror is feasible in an Ares V fairing. But, because the cylindrical portion of the Ares V fairing is only 9.7 m tall (compared to 17.2 m in the center), it is not possible to have a fixed secondary mirror. Instead, a deployed tower is required. See the separate volume (Appendix C) for a full report on the *ATLAST-8m* design.

## 2.2) Segmented Mirror Telescope Options

A segmented-mirror space telescope is the only viable architecture for filled aperture sizes greater than 8 meters. We explored two designs, with apertures of 9.2 m and 16.8 m, which are derived from the *JWST* architecture.

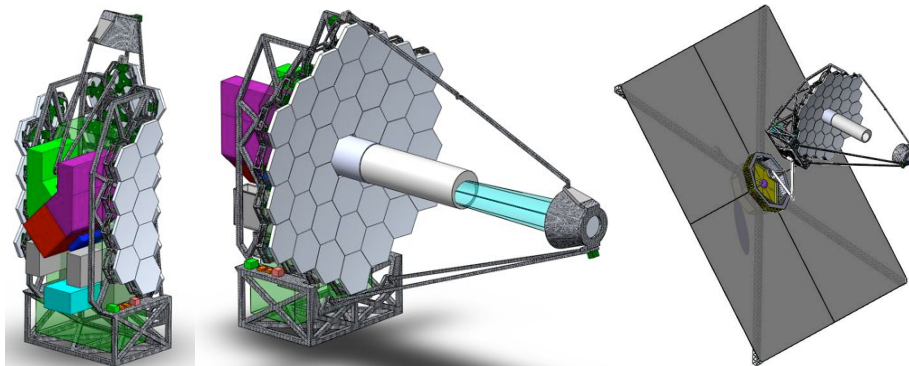


**Figure 6.** (Left) Stowed 9.2-meter OTA. Colored boxes are instrument envelopes. (Center) 9.2-m *ATLAST* Deployed. (Right) Sunshield and arm-mounted OTA. Spacecraft bus is on sun side of sunshield.

***ATLAST 9.2-meter:*** The *ATLAST-9.2m* (see Figure 6) draws heavily on *JWST*, taking advantage of engineering and technologies already developed for that mission. The OTA has a segmented 9.2 m aperture, consisting of 36 hexagonal ultra low expansion (ULE) glass mirrors

(1.315 m in size, flat-to-flat) on actuated hexapods. This technology was demonstrated early in the development of *JWST*. The OTA is thermally controlled using heaters on its backplane. The chord-folding of the primary mirror, similar to the *JWST* design, stows within the 6.5 m (outer diameter) fairing of an upgraded EELV. Upgraded EELVs with fairings of this size, coupled with lift capacity of more than 15,000 kg to SE-L2 are in the planning stages.

The TMA channel includes a wide-field camera, four combined fine-guidance sensors (FGS) and wavefront sensor (WFS) cameras, and accommodation for two additional science instruments (see Table 2). A continuous guide-star based wavefront sensing and control architecture that leverages the high TRL *JWST* technology is used in this design. Light from the telescope is fed to the FGS/WFS cameras for continuous guiding and wavefront sensing. A guide star selection mirror accesses a  $4 \times 4$  arcminute FOV and steers an isolated, bright star onto the FGS and WFS detectors. The FGS produces centroids with 0.5 milli-arcsecond noise equivalent angle at 5 Hz. Two separated FGSs provide roll sensing. For wavefront sensing, the light is divided into two beams, and each beam is sent through a narrow band ( $\Delta\lambda/\lambda \approx 1\text{-}5\%$ ) filter and a weak lens. One path uses a positive lens while the other uses a negative lens producing an out-of-focus image on either side of focus. To update the primary mirror positions and curvatures every five to twenty minutes, these images are processed onboard using phase retrieval. The secondary mirror position is adjusted as needed, using data obtained by three separated WFS cameras to break degeneracy with the primary mirror. A fourth FGS/WFS provides redundancy.

A thorough stray-light study concluded that a planar sunshield plus a central primary mirror baffle was sufficient to limit stray light to less than 10% of the zodiacal sky brightness while also eliminating “rogue path” light that would otherwise skirt around the secondary mirror. The deployed sunshield consists of four square-shaped layers of opaque Kapton film measuring 28 m on a side. To ease manufacturing, integration and test (I&T), and stowage procedures, each of the four layers is subdivided into four quadrants that are connected during I&T so that each deployed layer is continuous. Four 18-meter booms extend in a cruciform configuration to deploy the membranes.

The OTA is mounted on a multi-gimbal arm that provides OTA pitch motion, roll about the OTA line of sight, and center of mass trim for solar torque control while allowing the attitude of the spacecraft and sunshield to remain fixed relative to the Sun. This enables a very large field of regard with allowed pointing from 45 to 180° from the Sun. An active isolation system between the arm and OTA isolates spacecraft disturbances and, using the FGS sensor, provides a total image motion of  $\sim 1$  milli-arcsec. The spacecraft bus provides coarse attitude control, propulsion, power, communication and data handling modeled after the *JWST* approach, but employs a modular architecture that allows servicing and reduces risk during I&T. *See the separate volume (Appendix G) for a full report on the ATLAST-9.2m design.*

***ATLAST 16.8-meter:*** The OTA of *ATLAST-16* also consists of 36 hexagonal segments, in a 3-ring arrangement (see Fig. 7), but in this case each segment is  $\sim 2.4$  m (flat-to-flat) producing an edge-to-edge primary-aperture diameter of 16.8 m. The mass of *ATLAST-16* can easily be kept within the Ares V lift capacity by using low areal density ( $15 \text{ kg/m}^2$ ) mirror material. One option is actuated hybrid mirrors [22]. AHMs consist of metallic nanolaminate facesheets that provide a highly reflective, optical quality surface on a SiC substrate with embedded actuators for figure control. The orientation of the segments is controlled in six degrees-of-freedom by rigid body actuators.

## Advanced Technology Large-Aperture Space Telescope (ATLAST)

The segment rigid body and figure actuators are part of a wavefront sensing and control system required to maintain the telescope's optical performance. In addition, certain instruments will require a fine-steering mirror to stabilize images on a detector or spectrometer slit. The sensor for the segment rigid body actuators is an optical truss (*i.e.*, metrology system) that connects the segments to the secondary mirror. This truss provides a continuous update of the telescope configuration [23]. Multiple fine guidance sensors control the telescope body pointing.

The optical design is intimately connected with the strawman instrument suite (see Table 2). The *ATLAST-16m* wide FOV channel consists of two powered elements and a three-element stage that produces a compressed, collimated beam at a re-imaged pupil. The compressed beam has a manageable diameter of 30 cm.

Packing the 16.8-m telescope and its instrument suite is a significant challenge, even with the large volume in an Ares V fairing. Minimizing the primary-secondary mirror despace reduces mass, increases telescope stability, and increases the packaging options. To this end, we constrained the primary mirror focal ratio to 1.5 during the optical design phase. The geometry for the instrument volume depends on the folding scheme used for the telescope. To date, we have identified the following folding schemes for the telescope: chord-fold and hub-and-spoke.

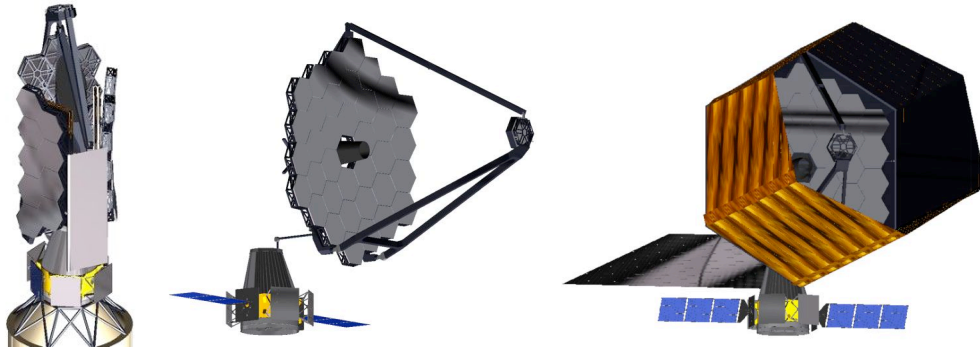


**Figure 7.** (Left) Stowed 16.8-meter OTA. (Center) 16.8-m *ATLAST* deployed but the sunshade and “kite tail” (to mitigate solar torque) are not shown. (Right) 16.8-m shown with sunshield, “kite tail,” and arm-mounted OTA.

The chord-fold design shares significant heritage with *JWST*. The primary mirror is folded to fit within the shroud and the secondary mirror is stowed along one edge. This architecture provides a cylindrical stowage volume 16 m in height x 8 m in width (see Fig. 7). Within this volume, a 16 m x 4.5 m diameter volume is available for instrument packaging. The disadvantages of this configuration are the increased center of gravity offset of the payload and reduced structural stiffness of the metering structure. In addition the secondary mirror must be replaced with a hexapod (vs. *JWST*'s tripod) to achieve reasonable (>10 Hz) decenter/despace frequencies.

The hub and spoke configuration folds the primary mirror around a 6.5 m diameter central hub, which supports petals on radial supports. The architecture provides a stowage volume 9 m in height x 8 m in width. The configuration provides a closer center of gravity offset of the payload and a simpler packaging for a conical sunshade. In addition, the structural stiffness of the primary mirror is greater and the secondary mirror support is simpler to package and deploy. The disadvantages of this configuration are the increased deployment complexity of the primary mirror and the reduced instrument packaging volume.

### 3. Top Three *ATLAST* Technology Drivers

The *ATLAST* technology development plan will bring the required technologies to readiness (Technology Readiness Level-TRL of six) as shown in Table 4. This section focuses on what we believe are the three most critical technology areas: 1) large-aperture space optics capable of diffraction-limited performance at 500 nm, 2) gigapixel focal plane arrays and high-efficiency UV detectors, and 3) starlight suppression systems for exoplanet studies.

**Table 4: *ATLAST* Technology Development Summary**

Technology	Need	Needed Product to Achieve TRL6	Current TRL	State of the Art
8-m Monolithic Telescope	Launch loads, zero gravity figure	Mirror blank vibration test and gravity calibration	N/A	Gemini, VLT
Lightweight, lower-cost mirror segments	1.3 to 2.5-m, < 15 kg/m <sup>2</sup> , > 20 m <sup>2</sup> /year, < \$1M/m <sup>2</sup>	Actuated Hybrid Mirror (AHM) or Glass Mirror at size, performance, and environments	4	JWST Architecture, AMSD Glass, AHM at 75 cm, Corrugated glass at 50 cm
Wavefront Sensing	Figure knowledge < 5 nm RMS	Laser metrology and/or image based sensing	4	SIM-derived gauges, JWST Testbed Telescope
Segment Actuation	Resolution < 2nm	Actuator hexapod test and environments	4	JWST, Moog, PI
Visible Detectors	8k x 8k arrays, and photon counting	Prototype performance and environments	3-4	E2V and TI photon counting CCDs
UV Detectors	Higher QE, 4 Mpix arrays	Prototype performance and environments	4	HST/ COS and STIS
UV Optics	UV IFS, coatings, dichroics	Prototype performance and environments	4	HST, FUSE
Internal Coronagraphs	10 <sup>-10</sup> contrast over 20% passband	Prototype performance and environments	4	JPL HCIT tests
Starshade	Deployment and shape control	Sub-scale and partial shade tests	3	Beamline tests, deployment design with high TRL parts

**Telescope Technology:** The diffraction-limited imaging at 500 nm that is needed for much of *ATLAST* science requires *HST*-quality mirror surface errors (5-10 nm RMS) to meet the overall system wavefront error of 36 nm RMS. For *ATLAST-8m*, solid meniscus monolithic glass, as demonstrated on ground-based telescopes, requires no new technology, but will require engineering to ensure survival of launch vibrations/acoustics and the proper gravity unloading. For the segmented *ATLAST* designs, hexagonal mirrors measuring 1.3 m and 2.4 m (flat-to-flat) are baselined for the 9.2-m and 16.8-m point designs, respectively. Some potential options for the mirror composition include the Advanced Mirror System Demonstrator (AMSD) ULE glass segments developed for *JWST*, Actuated Hybrid Mirrors (AHM), and corrugated glass technology [24]. Development goals for the segmented versions of *ATLAST* are primary mirror areal density of ~15 kg/m<sup>2</sup> and a systemic (including supporting structure and controls) areal density of ~30 kg/m<sup>2</sup>. Some growth in areal density is acceptable as segment cost and production rate are as important as mass in choosing the mirror technology.

Modest development of the AMSD mirrors would be required to achieve better surface error polishing and gravity error removal. Both AHM and corrugated glass are replicated and show promise for faster and less expensive mirror production than the current processes. JPL, in conjunction with Lawrence Livermore National Laboratory and Northrop Grumman/Xinetics,

have developed AHM over the last several years; see Figure 8. A metallic nanolaminate facesheet provides a high quality reflective surface, a SiC substrate provides structural support, and PMN surface parallel (in-plane) actuators provide surface figure control. Development is required to scale up segment size and improve surface figure. ITT has designed and tested corrugated glass mirror segments that promise faster and cheaper replicated production; however, they require development to demonstrate imaging quality, segment size and robustness in ULE glass. The TRL-6 milestone is a segment that meets environmental and wavefront error budget requirements.

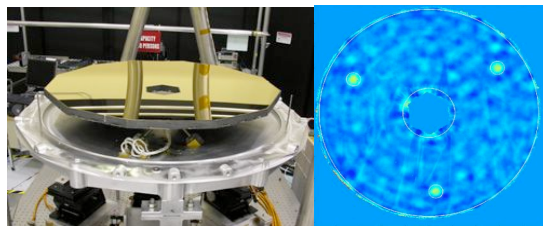


**Figure 8.** Actuated hybrid mirrors (AHM) of less than  $15 \text{ kg/m}^2$  have been tested and demonstrated 40 nm total WFE (gravity effect included), limited by high-spatial frequency mandrel polishing residual errors. With a higher quality mandrel, 10 nm surface figure error is achievable for meter-class segments.

Wavefront sensing and control (WFS&C) also needs to be advanced from *JWST* to meet visible image quality with an allocation of 10-15 nm RMS wavefront error for WFS&C residual. The segment's positions must be measured to a few nanometers at a rate faster than their support structure's time constants. For *ATLAST-16m*, a JPL-developed laser metrology truss technology, derived from the SIM laser distance gauges, measures each of the segment's six degrees of freedom location (relative to the secondary mirror) at very high rates (up to 1

kHz); additional gauges locate downstream optics. The current TRL is 4; development is needed to advance the stability of the metrology and shrink the size and mass of the fiber-fed beam launchers. Periodic image-based WFS employs phase retrieval to correct drifts in the laser metrology. Actuators supporting the segments require a modest technology development to reduce the resolution to less than 2 nm and increase bandwidth. A TRL-6 demonstration of the telescope's full system operation is proposed with a subscale (6-m class), partially populated (three-segment) testbed meeting error budgets under full thermal, vacuum, vibration, and jitter environments. For more details on the relevant telescope technologies, see also the Astro2010 Technology Development paper by Werner et al. [25]. See Appendices F, G, and H for more details.

**Detector Technology:** Gigapixel detector arrays for visible imaging and  $\sim 500$  Megapixel arrays for NIR imaging are required for studies of resolved stellar populations, galaxy evolution, and structure formation. Such arrays can be built with existing technology. However, development would result in better science performance (lower noise), lower risk (less complex electronics), lower cost, and lower power consumption. The wide field cameras in all *ATLAST* designs are envisioned to have  $\sim 1$  to 1.6 gigapixels per channel.

Exposure times invested in exoplanet and other faint object spectroscopy could be reduced by up to five times using photon counting detectors. Technology development of photon-counting CCDs is based on the low-light level CCDs built by E2V and the similar technology of Texas Instruments. The current TRL is 4; improvements in anti-reflection (AR) coatings, voltage swing, and charge induced clock noise would be demonstrated before the completion of a TRL-6 qualification program. In the longer term, CMOS based detectors are likely to be used. Detectors made by Fairchild, Sarnoff, and Fill Factory represent the state-of-the-art. Improvements in dark current, AR coating, in-pixel gain structure, and backside thinning would need to be demonstrated before the completion of a TRL-6 qualification program.

UV detectors have ample room for improvements in efficiency and format size. UV spectroscopy, in particular, requires coatings, optics and detectors that are highly efficient. Current flight UV imaging detectors use CsI and CsTe photocathodes with 10% - 30% quantum efficiencies (QE). Photocathodes with QE of 30% - 80% using cesiated p-doped GaN have been produced in the lab, but have not yet been integrated into detector systems. Materials such as p-doped AlGaIn and MgZnO should be developed for higher QE over a wider band, and better AR-coatings may be matched with p-channel radiation-hardened photon-counting CCDs. For the far UV, higher QEs also are required, and III/V materials are effective. All must be coupled with large-format intensifier and readout systems. EBCCDs and microchannel plate methods (ceramic and glass) compete for the highest QE and largest formats, and both should be pursued. The current TRL for high QE UV detectors is four; a downselect will precede TRL-6 qualification. *See Appendices I and J for more details.*

***Starlight Suppression Technology:*** An internal coronagraph or external occulter than can suppress starlight by a factor of  $10^{10}$  is required to characterize Earth-sized exoplanets. The best starlight suppression technology is not yet obvious. Fortunately, there are multiple options. The technology development plan addresses the viability of 1) a visible nulling coronagraph (VNC) that any telescope could use (development costs might be shared with large ground-based telescopes); 2) a Lyot-type coronagraph (for use with monolithic telescopes); and 3) an external starshade (a separate spacecraft creating a star shadow at the telescope). All three methods are currently at or below TRL-4 [26]. Recognizing the importance of *ATLAST* to exoplanet science, we would fund development of all three methods for starlight suppression, with a downselect 3-5 years before the scheduled TRL-6 milestone.

There are a number of coronagraphic configurations, each having tradeoffs between achievable contrast, IWA, throughput, aberration sensitivity, and ease-of-fabrication. Most techniques do not work on conventional (4-arm spider) obscured or segmented systems, but some non-conventional spider configurations (linear support) appear to allow performance competitive with off-axis systems. The VNC approach is probably the only viable solution for *internal* suppression with a segmented telescope. VNC development is required to demonstrate  $10^{-10}$  contrast over a 23% passband. This requires the development of a spatial filter array (1027 fiber bundle), deformable mirror (MEMS 1027 segment), and an achromatic phase shifter. Testbeds at JPL and GSFC have presently achieved  $10^{-7}$  contrast ratios. Coronagraphic technology development is critically dependent on advancements in high-precision, high-density deformable mirrors (>96 actuators across pupil and sub-Angstrom stroke resolution).

Starshade technology development is well described in the New Worlds Observer RFI response. Starshade theoretical performance has been validated by at least 4 independent algorithms and, in the lab, by two beamline testbeds. Detailed CAD models exist for the *NWO* 50-m starshade, which use high TRL-components (membranes, hinges, latches, booms). For *ATLAST*, larger starshades are required: 80 m and 90 m for our 8-m and 16.8-m telescopes, respectively. The key challenges are primarily deployment reliability and shape control. *ATLAST* starshade separations of 165,000 km to 185,000 km, while large, do not present any challenging formation flying or orbital dynamics issues but put additional requirements on the starshade propulsion system. The starshade technology developments are addressed through increasingly larger subscale models with TRL-6 being demonstrated through beamline tests, a half-scale quarter-section deployment, and a full-scale single petal deployment, performance, and environmental testing. The astrometric sensor and NASA's Evolutionary Xenon Thruster

# Advanced Technology Large-Aperture Space Telescope (ATLAST)

(NEXT) ion engine needed to align the starshade already will be TRL-6 or greater by other projects: USNO’s JMAPS and NASA’s in-space propulsion program. *See Appendices K and L for more details.*

## 4. Summary of the ATLAST Technology Development Plan

The ATLAST Technology Development Plan is summarized in Figure 9. This roadmap shows the TRL 5 and 6 milestones, downselect logic, funding profile, and interactions within the technology development tasks. Assuming a 2011 start for technology development, the project would initially begin funding high priority technology developments at a low level. The schedule is divided in to six periods. If we can afford a “full speed ahead” pace, each period would last one year and all technologies would reach TRL-6 in 2017. A slower schedule of 1.5 years per period would be completed by 2020. Milestones are placed at the TRL-5 level and coincide with downselects in three areas (mirror segment technology, visible detector technology, and starlight suppression technology). All technologies would plan to complete their TRL-6 milestones with at least a year margin before a mission PDR (NASA requires TRL-6 at PDR), allowing a healthy schedule margin of two months per year. A parallel pre-formulation mission study would inform the technology trades and downselects. Downselect decisions on the launch vehicle and primary mirror architecture (monolith versus segmented) are made by the end of period three.

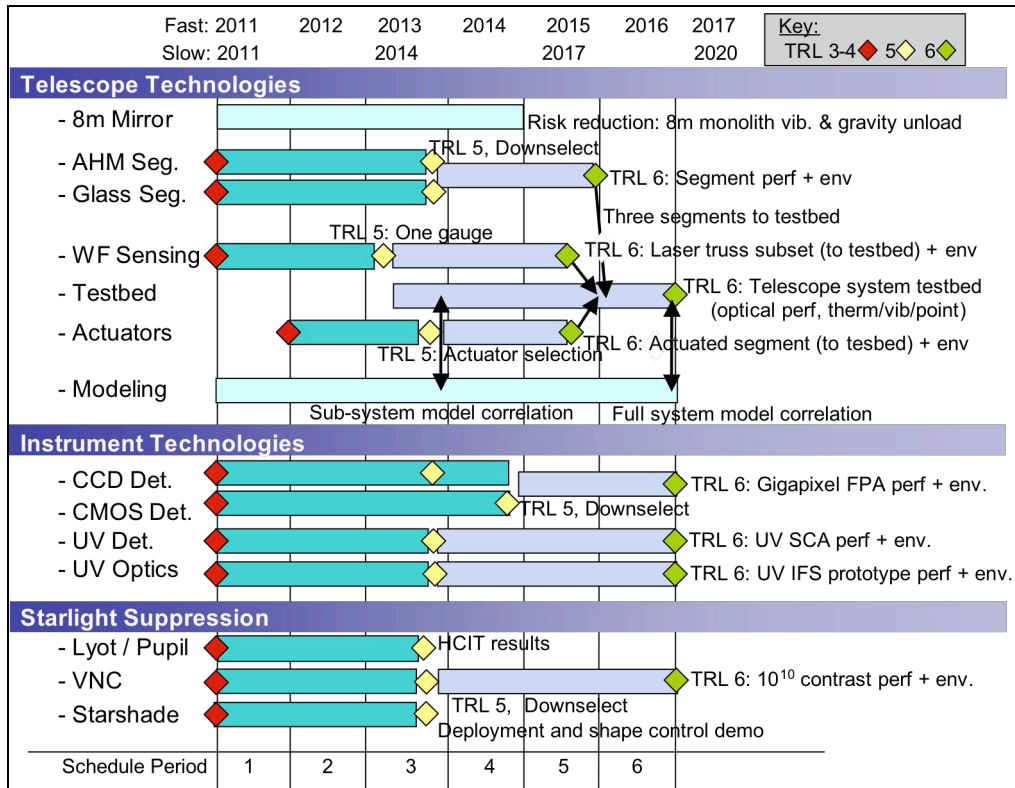


Figure 9. Proposed ATLAST Technology Development Plan & Schedule

The telescope technology roadmap includes funding for AHM and corrugated-glass segments through a TRL-5 downselect with AMSD segments as an offramp. One full size

segment is then taken through TRL-6 qualification and three 1.3-m segments are delivered to the testbed task for system validation. Wavefront sensing with laser metrology is matured to TRL-6 and a set of gauges delivered to the testbed; image based sensing and better thermal stability is an offramp. Actuators already are close to meeting their performance and flight qualification requirements so they only require modest funding to a TRL-6 demonstration of a hexapod-actuated segment; a set of actuators is delivered to the testbed. The testbed demonstrates the end-to-end performance thereby qualifying the full telescope system at TRL-6. Integrated modeling is a critical element of proving technology at full scale in space and is based on sub-scale ground testing. This effort iterates with other tasks to analyze the designs and shape the testing procedures so that uncertain elements of the model are tested, thus providing a “two-way street.” Technology investment in low-cost lightweight mirror benefits not only a large space telescope but also smaller missions; a single segment could serve a SMEX-class telescope.

The instruments section of the roadmap addresses detectors and some instrument technologies for UV optics (filters, gratings, and coatings). Advancements in all of these areas will improve SNR in a given exposure time or significantly reduce exposure time required to reach a given SNR. Investments on total throughput efficiency may be traded against aperture size, provided spatial resolutions are not degraded below the science requirements. The technology investments in detectors would again serve both *ATLAST* and smaller class missions.

The starlight suppression technology is advanced in all three methods through TRL-5 since the *ATLAST* optical telescope assembly architecture is still open. A strict downselect may not be warranted, as *ATLAST* is compatible with both an internal method and a starshade. If a separate exoplanet probe mission were selected to precede *ATLAST*, both could potentially share technology development costs, thus reducing *ATLAST*'s overall costs.

**Summary by Point Design:**

***ATLAST-8m:*** Because of the high-TRL of 8-m mirrors, no mirror technology development is required. Rather, we strongly suggest elimination of schedule risk by determining the mirror blank's ability to survive launch before Phase A. If the existing Zerodur blank is not suitable then a long-lead replacement blank procurement process could be initiated. Flight qualification for an 8-m primary mirror is accomplished by scaling-up and qualifying standard engineering methods proven on ground telescopes, *HST* and *Kepler*. Polishing all surfaces of the blank raises its stress design limit to 7000 psi and allows inspection of any internal defects which could limit its strength. Actual blank strength can be characterized via proof and sine-burst tests. Simultaneously, it is possible to mitigate on-orbit performance risk by absolutely calibrating the blank's g-release shape change.

***ATLAST-9.2m:*** Technology development would be moderately cheaper (vs. *ATLAST-16m*) for the telescope technology portion of the roadmap due to the higher reliance on existing AMSD segment and image-based wavefront sensing technologies.

***ATLAST-16m:*** This concept requires the full development investment because novel WFS&C systems and multiple mirror material and fabrication technologies need to be explored.

The major milestones of the technology development effort are the TRL-5 and 6 gates. A technology evaluation board made up of non-advocate experts in each of the areas would be formed for the duration of the effort. The board's first job would be to outline the exact demonstration that would satisfy the TRL-gates. Then, as the development efforts matured and completed these demonstrations, the test data and modeling would be presented back to the board for TRL-gate review. The board's final review is a Technology Non-Advocate Review that

## Advanced Technology Large-Aperture Space Telescope (ATLAST)

would validate all required mission technologies at TRL-6 or higher, thereby supporting a successful PDR and allowing the mission to proceed to implementation. Once technology development is complete and the key decision point given, the elapsed time between the start of phase A and launch is 8 to 12 years, depending on the design selected.

The cost estimates for the *ATLAST* Technology Development Plan (TDP) are given in Table 5. Experts in the 14 technology areas generated all our TDP costs. These experts, representing NASA/GSFC, NASA/MSFC, JPL, Ball Aerospace, Northrop Grumman, Xinetics, and ITT, have planned tasks to meet TRL-6.

**Table 5: Technology Development Cost Estimates (FY09 \$M, No Reserves)**

Period:	1	2	3	4	5	6		Totals
Fast:	2011	2012	2013	2014	2015	2016	2017	
Slow:	2011	2013	2014	2016	2017	2019	2020	
<b>8-m Telescope</b>								<b>20.0</b>
- Blank Vib. Test	5.0	5.0	5.0	5.0				20.0
<b>Segmented Telescope</b>								<b>147.8</b>
- AHM Seg.	4.6	5.8	6.4	9.3	12.9			39.0
- Glass Seg.	2.2	3.0	3.8	11.0	20.0			40.0
- [downselect savings]				-11.3	-20.9			-32.2
- Laser Truss	1.0	2.0	5.0	5.0	5.0			18.0
- Testbed			5.0	20.0	20.0	20.0		65.0
- Actuators		0.5	1.5	2.5	2.5			7.0
- Modeling	1.0	1.5	1.5	2.0	2.0	3.0		11.0
<b>Instruments</b>								<b>60.1</b>
- CCD Detectors	1.6	0.6	1.0	1.0	4.0	4.0		12.2
- CMOS Det.	0.9	1.2	0.9	0.9	4.0	4.0		11.9
- [downselect savings]					-4.0	-4.0		-8.0
- UV Detectors	3.0	5.0	6.4	5.3	5.5	2.7		27.9
- UV Optics	0.9	3.1	4.3	3.5	2.8	1.6		16.1
<b>Starlight Suppression System</b>								<b>59.5</b>
- Lyot / Pupil Cor.	6.3	7.7	5.6	6.0	5.5	4.0		35.1
- VNC	0.9	1.7	4.4	2.5	16.9	5.2		31.5
- Starshade	1.5	1.5	5.0	5.0	10.5	10.5		34.0
- [downselect savings]				-5.5	-20.9	-14.7		-41.1
<b>Technology Development Sub-Total:</b>								<b>287.4</b>
<b>Mission Study</b>								<b>48.0</b>
- Science WG & Studies	4.0	4.0	4.0	4.0	4.0	4.0		24.0
- Project Office & Eng. Studies	4.0	4.0	4.0	4.0	4.0	4.0		24.0
<b>Totals</b>	<b>36.9</b>	<b>46.5</b>	<b>63.8</b>	<b>70.2</b>	<b>73.8</b>	<b>44.3</b>		<b>335.4</b>

The tasks in our TDP are spread over six schedule periods. Downselects in three areas after period three allow higher funding on the most promising technology for the final three periods. Informing this downselect schedule requires mission decisions about launch vehicle and segmented versus monolithic telescope. All estimated costs are in constant FY2009 dollars and do not include reserves. The time phasing of the technology development cost grows nearly linearly from \$29M in the first period to \$66M in the fifth period. The segmented telescope technology investment area is the greatest, at \$148M. This value is consistent with the sum of cost estimates for lightweight large aperture and WFS&C given by the NASA Advanced Planning and Integration Office roadmap activity in 2005. That effort included members from NASA, industry, and the National Reconnaissance Office. The detector development benefits any space UVOIR instrument regardless of mission size. The starlight suppression technology builds, in part, on the investment in *TPF-C* at JPL over the last decade. The *ATLAST* TDP costs here assume full coverage of the VNC and starshade costs. We assume some of the Lyot/pupil internal coronagraph technology development costs will be shared with a smaller exoplanet probe mission; only 70% of the grass roots cost estimate is included for the first three periods; 100% in the last 3, post-downselect.

A total *ATLAST* technology development project would cost \$287M if all downselects were kept open until the TRL-5 milestones in period three. This does not include reserves, which would be held at the program level. The range of technology development cost estimates for *ATLAST-8m* spans \$55M - \$149M depending on the degree to which early downselects are taken. The cost estimate range for the *ATLAST* segmented-mirror concepts spans \$115M - \$267M, again, depending on the timeline for early downselects taken.

In addition to the cost estimates for technology development given above, there would be a parallel mission study integrated with the technology development work. This was roughly estimated at \$8M per period, with half supporting an *ATLAST* science working group and competitively awarded grants and half supporting a pre-formulation project team and competitively awarded engineering studies.

*The full details of our TDP are provided as a separate volume. It is available on-line. Go to <http://www.stsci.edu/institute/atlast> and click on “ATLAST Mission Concept Study.”*

#### 4.1) *ATLAST Mission Life Cycle Cost Estimates*

Mission costs and parameters for *ATLAST-8m* and *ATLAST-9.2m* have been studied at MSFC and GSFC, respectively.

The *ATLAST-9.2m* mission concept was studied in the Integrated Design Center (IDC) at Goddard Space Flight Center for three weeks during February and March 2009. A combination of parametric and “grassroots” estimates of mission cost were developed for the life cycle of the mission in **constant FY08 dollars**. The total cost for phases A through E, including 30% reserve on all mission elements, is **\$5.6B**.

This total includes 5 years of mission operation costs (\$200M) plus \$125M to the science community for research and analysis of the data. The total does not include the cost of the launch vehicle, which is not currently known; the IDC provided an approximate cost of \$400M for this item. The *ATLAST-9.2m* cost by mission phase is given in Table 6.

**Table 6**

<b><i>ATLAST-9.2m</i> (FY08 \$)</b>	
Phase A	340M
Phase B	1,400M
Phase C/D	3,470M
Phase E	375M

## Advanced Technology Large-Aperture Space Telescope (ATLAST)

The *ATLAST-8m* cost was studied at the Advanced Concepts Research Facility at Marshall Space Flight Center during the February – March 2009 timeframe. The result of this study was a cost estimate for the *ATLAST-8m* payload. The MSFC estimate is being reviewed for completeness and compared with the GSFC IDC cost methodologies to finalize a life cycle cost. The preliminary estimates indicate that the full life cycle cost (including a 5-year phase E period) for *ATLAST-8m* is \$4.5B to \$5B. However, final cost estimates were not available at the time this RFI response was submitted. They are expected prior to June.

The *ATLAST-9.2m* and *ATLAST-8m* life cycle costs do not include the cost of an external occulter and its spacecraft. The above costs, however, do include the estimated cost of an internal coronagraphic instrument. A life cycle cost estimate for *ATLAST-16m* has not been performed.

### **Acknowledgements**

The Goddard Space Flight Center managed the NASA Astrophysics Strategic Mission Concept Study of *ATLAST*. Portions of the work were performed at the Space Telescope Science Institute, Ball Aerospace & Technologies Corp., Goddard Space Flight Center, Marshall Space Flight Center, the Jet Propulsion Laboratory, the California Institute of Technology, Northrop Grumman Aerospace Systems, the University of Colorado at Boulder, the University of Massachusetts at Amherst, and Princeton University. The University of Alabama in Huntsville, ATK and Schott Glass provided additional support for the *ATLAST-8m* engineering study.

**Appendix A: Table of Acronym Definitions**

AHM	Actuated Hybrid Mirror	IDC	Integrated Design Center	SAFIR	Single Aperture Far-IR Telescope
AMSD	Advanced Mirror System Demonstrator	IFU	Integral Field Unit	SE-L2	Sun-Earth 2 <sup>nd</sup> Lagrange point
AO	Adaptive Optics	IGM	Intergalactic Medium	SIM	Space Interferometry Mission
ATLAST	Advanced Technology Large Aperture Space Telescope	IMF	Initial Mass Function	SM	Secondary Mirror
BL	Beam Launcher	IRU	Inertial Reference Unit	SMEX	Small Explorer Mission
CAD	Computer-Aided Design	ISS	International Space Station	SNR	Signal-to-Noise Ratio
CC	Corner Cube	IWA	Inner Working Angle	TDP	Technology Development Plan
CCD	Charge Coupled Device	JMAPS	Joint Milli-Arcsecond Pathfinder Survey	TMT	Thirty Meter Telescope
CM	Center of Mass	JPL	Jet Propulsion Laboratory	TPF-C	Terrestrial Planet Finder Coronagraph Mission
CMG	Control Momentum Gyro	JWST	James Webb Space Telescope	TRL	Technology Readiness Level
CMOS	Complementary Metal–Oxide Semiconductor	LDG	Laser Distance Gauge	ULE	Ultra Low Expansion
COS	Cosmic Origins Spectrograph	LT	Laser Truss	UV	Ultraviolet
CP	Center of Pressure	MEMS	Micro Electro-Mechanical Systems	UVOIR	The wavelength range from ~110 to ~2500 nm
CTE	Coefficient of Thermal Expansion OR Charge Transfer Efficiency	MLI	Multi-Layer Insulation	VDA	Vacuum Deposited Aluminum
DM	Dark Matter OR Deformable Mirror	MSFC	Marshall Space Flight Center	VLT	Very Large Telescope
DOF	Degrees of Freedom	NASA	National Aeronautics and Space Administration	VNC	Visible Nulling Coronagraph
DSN	Deep Space Network	NEXT	NASA's Evolutionary Xenon Thruster	WFC	Wavefront Control
EELV	Enhanced Expendable Launch Vehicle	NFOV	Narrow Field of View Channel	WFE	Wavefront Error
FGS	Fine Guidance Sensor	NWO	New Worlds Observer	WFOV	Wide-field of View Channel
FOV	Field of View	OSE	Optical State Estimator	WFS	Wavefront Sensing
FPA	Focal Plane Array	OTA	Optical Telescope Assembly	WFS&C	Wavefront Sensing and Control
FSM	Fast Steering Mirror	PDR	Preliminary Design Review		
FUSE	Far Ultraviolet Spectroscopic Explorer	PM	Primary Mirror		
GALEX	Galaxy Evolution Explorer	PSF	Point Spread Function		
GSFC	Goddard Space Flight Center	PWB	Printed Wiring Board		
HST	Hubble Space Telescope	RF	Radio Frequency		
HZ	Habitable Zone				

## Appendix B: Synergy with Other Astronomical Facilities

The impressive capabilities anticipated for the 20-m to 40-m optical/near infrared (NIR) ground-based observatories in the upcoming decade will redefine the existing synergy between ground and space telescopes. Adaptive optics (AO) may enable ground-based optical telescopes to achieve intermediate Strehl ratios (~40%-80%) over a field of view of up to 2 arcminutes at wavelengths longer than ~1000 nm [17,18,19,20]. Extreme AO may even enable diffraction-limited performance at ~600 nm in a ~2 arcsecond field of view, albeit with extremely limited sky coverage. Space telescopes, of course, provide exclusive access to UV wavelengths. But there are unassailable advantages of space telescopes for observations in the optical and NIR range:

- Ultra-deep panoramic imaging (tens of arcminutes or more)
- High Strehl ratios (>90%) that are highly stable (<2% variations) spatially and temporally
- Very high-contrast imaging (<10<sup>-8</sup>)
- Ultra precise photometry (<0.0001 magnitude) and astrometry (<<1 mas)
- Ability to achieve any of the above on demand (no day/night or weather at L2 orbit)

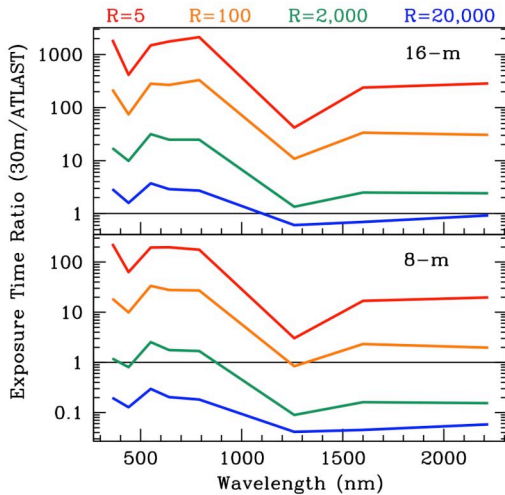


**Figure B-1.** Exposure time ratio to reach SNR=10 between a ground-based 30-m (with AO in the near-IR) and *ATLAST* 8-m and 16-m as a function of spectral resolution,  $R$ , and wavelength. *ATLAST* is faster when ratio is greater than 1. The ratios for  $R=5$ , 100, 2000, and 20000 are shown as red, orange, green, and blue, respectively.

faster than a 30-m on the ground for imaging; 20 to 300 times faster for  $R=100$  spectroscopy from 300 – 2500 nm and typically 10 to 30 times faster for  $R=2000$  optical spectroscopy. Large ground-based telescopes will, in general, be faster for most medium and high-resolution ( $R > 2000$ ) spectroscopy, at least for sources brighter than ~28 AB magnitude. *ATLAST* imaging would reach the depth of the *HST* Ultra Deep Field ~100 times faster (for 8-m) to >1300 times faster (for 16-m) than *HST* but with higher spatial resolution, enabling panoramic ultra deep fields covering hundreds of times the original UDF area.

*ATLAST*'s high spatial resolution, coupled with its sensitive high-resolution UV/optical spectroscopic capabilities, will make it an ideal companion to *ALMA* (e.g., to fully interpret proto-planetary disk chemistry and dynamics). *ALMA* will achieve 5 milli-arcsecond resolution at its highest frequency, 900 GHz. *ATLAST* will complement in-situ spacecraft by enabling long-term monitoring of the outer planets and small bodies within our Solar System. Its large collecting area will enable UV imaging, below 200 nm, of small bodies beyond Jupiter revealing subtle albedo variations and the possible presence of simple organic molecules.

### **Appendix C. Summary of the *ATLAST-8m* Engineering Team Study**

The *ATLAST-8m* engineering study was lead by NASA MFSC with guidance from the Space Telescope Science Institute and collaboration team members from NASA GSFC, NASA JPL, Northrop-Grumman, and Ball Aerospace. The University of Alabama in Huntsville, ATK and Schott Glass provided additional support. **The key conclusions were summarized earlier but the full details can be found in a separate volume that is available at <http://www.stsci.edu/institute/atlast>** (click on “*ATLAST* Mission Concept Study”).

**Appendix D. ATLAST-8m Thermal Analysis**

During the course of the *ATLAST* Advanced Strategic Mission Concept Study for NASA, Craig E Shimoda of Northrop Grumman Aerospace Systems performed a thermal analysis for *ATLAST-8m* to compare sunshade options and determine heater power requirements. The results of this analysis are summarized below.

**Sunshade Configuration.** Two sunshade design concepts were evaluated: the simple cylindrical sunshade shown in Figure D-1, and an alternate “new” sunshade design, consisting of a cylindrical telescope barrel with light baffles plus a three-layer “sugar scoop” sunshade, shown in Figure D-2.

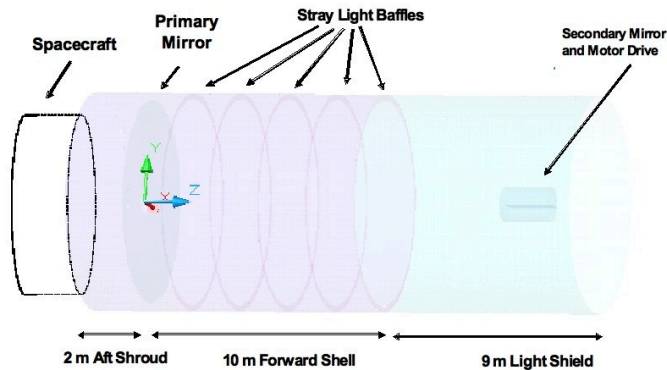


*Figure D-1.* The Original Sunshade Design

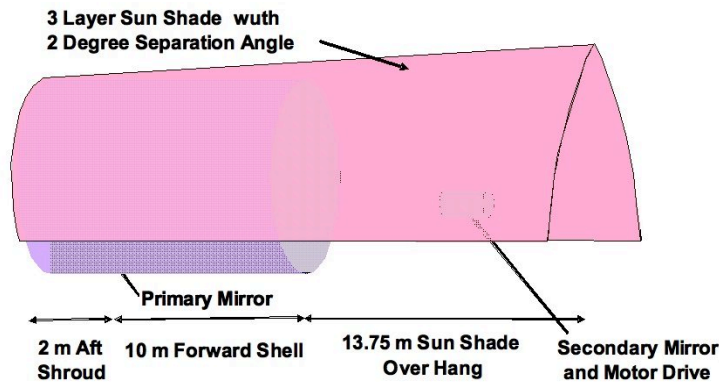


*Figure D-2.* Alternate “New” Sunshade Design Concept

The “Sugar Scoop” sunshade is shown in more detail in Figure D-3. The three layers are made from the 2-mil Kapton-E membrane material developed for the *JWST* sunshield, where the first two layers have highly specular (> 90%) coatings of Silicon on the outer side and vacuum deposited Aluminum (VDA) on the inner side, while the third layer has VDA coatings on both sides. The specular surfaces, low emissivity inner surfaces, and 2 degree dihedral between layers allows the infrared photons emitted by the membranes to “bounce” back and forth between layers until they “walk their way” to the open end of the shade and escape.

The three layer sunshade attenuates the incident solar radiation by a factor of ~6,000 and makes the telescope optics relatively insensitive to variations in the angle of incidence of sunlight on the sunshade.

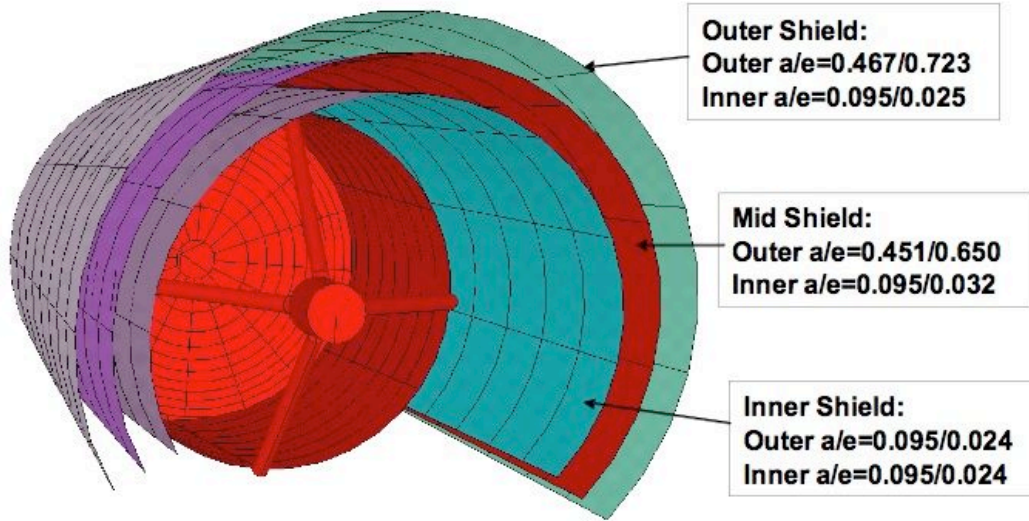


Figure D-3. Geometry of the Alternate “New” Sunshade Design

**Thermal Analysis.** The four cases for which steady state operational temperatures were determined are shown in Figure D-4. We assumed the solar constant is  $1,296 \text{ W/m}^2$  at L2, and that the telescope is wrapped with a 50-layer MLI blanket on its outer surfaces with  $\epsilon^* = .004$  on the sides, and  $\epsilon^* = .02$  on back of tube. The MLI blanket is covered with 10 mil thick silverized Teflon for low solar flux absorbance ( $\alpha = 0.09$ ,  $\epsilon = 0.82$ ). The primary mirror (PM) material is Zerodur, and its front surface is coated with Al MgF<sub>2</sub> ( $\alpha = 0.80$ ,  $\epsilon = 0.20$ ). The PM diameter is 8.2 m, its thickness is 17.5 cm, and its center hole diameter is 1.0 m. The inner barrel surface and baffles are covered in black Kapton film.

**Heater Power.** The optimum mirror temperature for a UVOIR telescope such as *ATLAST* is 300K. Our estimate of the heater power required to maintain this temperature does not include inefficiencies or contact resistance, and no spacecraft, instrument or avionics heat dissipation was considered in the analysis.

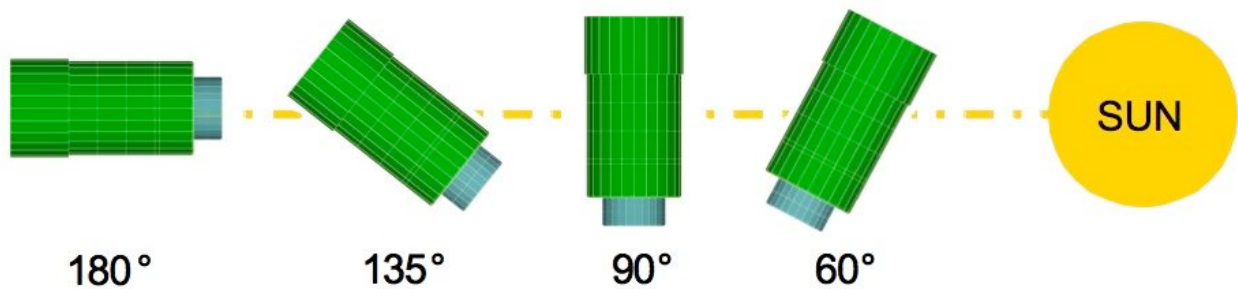
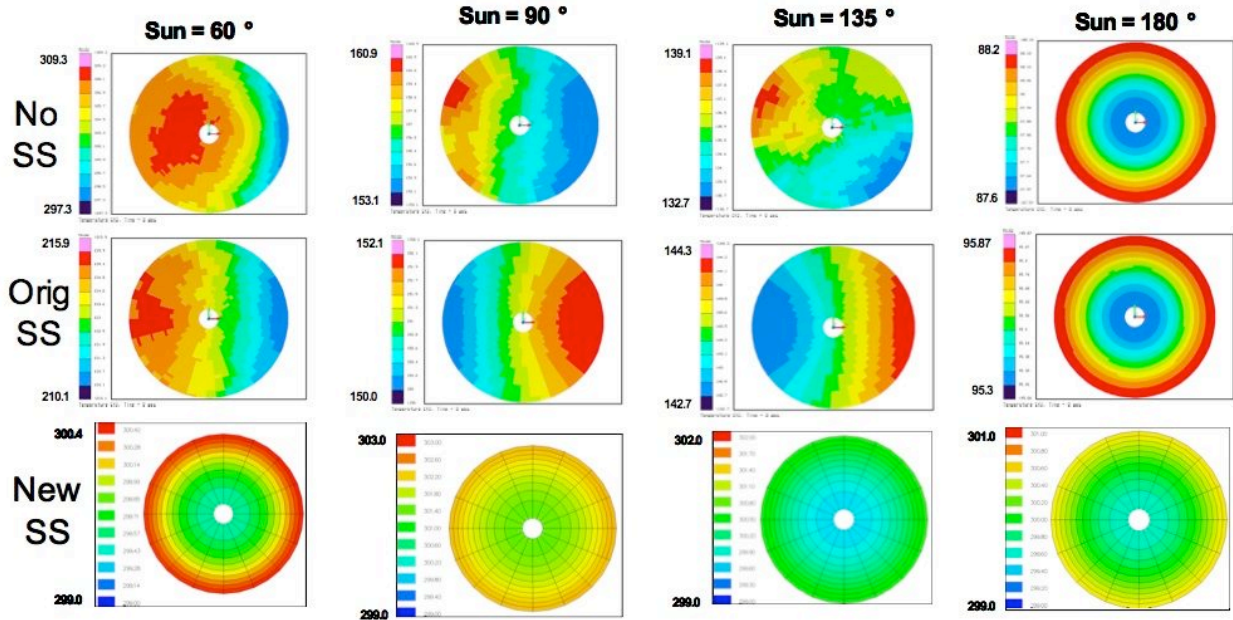


Figure D-4. Telescope Orientation for the Four Thermal Analysis Cases

The steady state temperature distributions of the primary mirror for the *ATLAST-8m* for the four orientations are shown in Figure D-5. From top to bottom the figure shows the temperature distribution for (1) the PM with no baffles or sunshade; (2) the original configuration with baffles and the cylindrical sunshade; and (3) the alternate “new” configuration with the three layer “Sugar Scoop” sunshade. From left to right, the figure shows the PM temperature

## Advanced Technology Large-Aperture Space Telescope (ATLAST)

distributions for the four orientations: 60°, 90°, 135°, and 180°. [Note the temperature scales are different in each case.]



**Figure D-5.** Two dimensional steady state operational temperatures for the *ATLAST* 8-m primary mirror for the four sun angles, and three configurations: “No SS” = No baffles and sunshade; “Orig SS” = Original sunshade and baffles; and “New SS” = multi-layer ‘sugar scoop’ sunshade.

The temperature gradient across the PM and heater power requirements for each case shown in Figure D-5 are summarized in Table D-1.

**Table D-1: ATLAST-8m Maximum Temperature Gradients and Heater Power Requirements**

Configuration	Parameter	Orientation			
		60°	90°	135°	180°
No Baffles or Sunshade	Max Gradient (°K)	12.0	7.8	6.1	0.6
	Heater Power (W)	~300	3774	3907	4047
Original Sunshade	Max Gradient (°K)	5.8	2.1	1.6	0.57
	Heater Power (W)	213.0	151.6	143.5	95.6
New Sugar Scoop Shade	Max Gradient (°K)	0.99	0.15	0.13	0.04
	Heater Power (W)	3500	3600	3520	3520

Shielding the PM from direct sunlight by cylindrical sunshade and baffles reduced the maximum thermal gradients across the mirror by a factor of ~3; adding the sugar scoop sunshade reduced the maximum gradients by another factor of ~12. Adding the sugar scoop sunshade also reduced the variation in heater power requirements from ~4400 Watts to ~100 W, significantly reducing the time to reach thermal equilibrium after a change in attitude of the telescope. The

heaters were “turned off” for our analysis of the original sunshade configuration, in order to see what temperature the optics would reach for the different orientations, i.e.: ~96 K when looking in the anti-solar direction without and heat transfer from the spacecraft bus or instruments.

**Sunshade Temperatures.** The temperature distributions for the outer sunshade layer were also calculated by our model, and are shown in Figure D-6. Peak temperatures varied from ~210 to 341 °C, and minimum temperatures from ~2 to 61 °C.

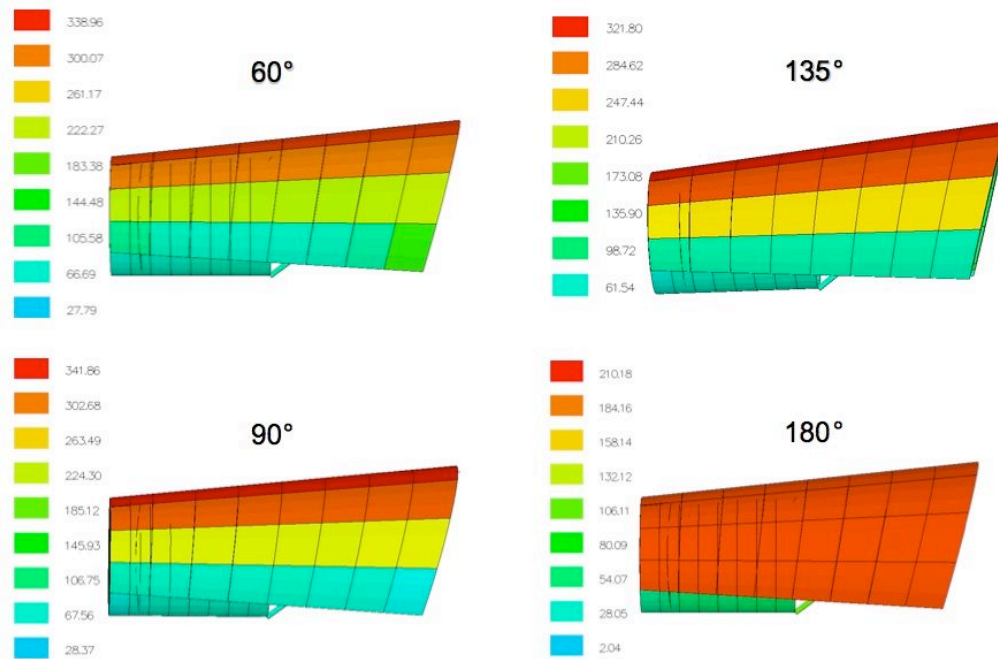


**Figure D-6.** Temperature Distribution on the Outer Layer of the Sugar Scoop Sunshade (in °C)

## Summary

The original sunshade and baffle design for the *ATLAST-8m* reduced the maximum thermal gradients across the primary mirror by a factor ~3 compared with the unshielded mirror. The addition of the Alternate “New” “Sugar Scoop” sunshade reduced the gradients by an additional factor of 10. The sugar scoop sunshade also reduced the peak heater power requirements ~11% (from ~4,050 to 3,600 Watts) and the variation in power settings by a factor of ~50, i.e.: to ~3,500 ± 50 Watts. Given the large thermal inertia of the (20,000 kg) 8-m primary mirror, there should be no change in its optical performance and point-spread-function (PSF) as the telescope moves from one target to the next. The *ATLAST-8m* PSF should be orders of magnitude more stable than that of the Hubble Space Telescope, greatly facilitating the high contrast imaging required for ExoPlanet detection and characterization.

**Appendix E: Solar Torque Mitigation Systems for *ATLAST-16m***

Solar radiation pressure is the primary disturbance source [27] for spacecraft in heliocentric orbits, including Sun-Earth L2 halo orbits and Earth trailing or leading drift-away orbits. Misalignment of the center of pressure (CP) and the center of mass (CM) of the spacecraft produces an external torque for which the spacecraft’s attitude control system must compensate in order to maintain the desired orientation in space.

The force exerted on a spacecraft by solar radiation is primarily influenced by the spacecraft’s geometry and its surface properties. The worst-case solar radiation torque produced by this constant force onto a specularly reflective surface is:

$$T_{SP} = P_s A_s L_s (1 + q) \cos(i)$$

where  $P_s$  is the solar constant,  $4.167 \times 10^{-6} \text{ N/m}^2$ ,  $A_s$  is the area of the surface,  $L_s$  is the CP to the CM offset,  $i$  is the angle of incidence of the sunlight, and  $q$  is the reflectance factor that ranges from 0 to 1. Typically,  $q = 0.6$  is used for these estimates. Calculation of this torque is important for sizing the spacecraft reaction wheels that are used to control the spacecraft’s attitude and store the momentum that builds up in them; and for sizing the thrusters and propellant used to dump this momentum.

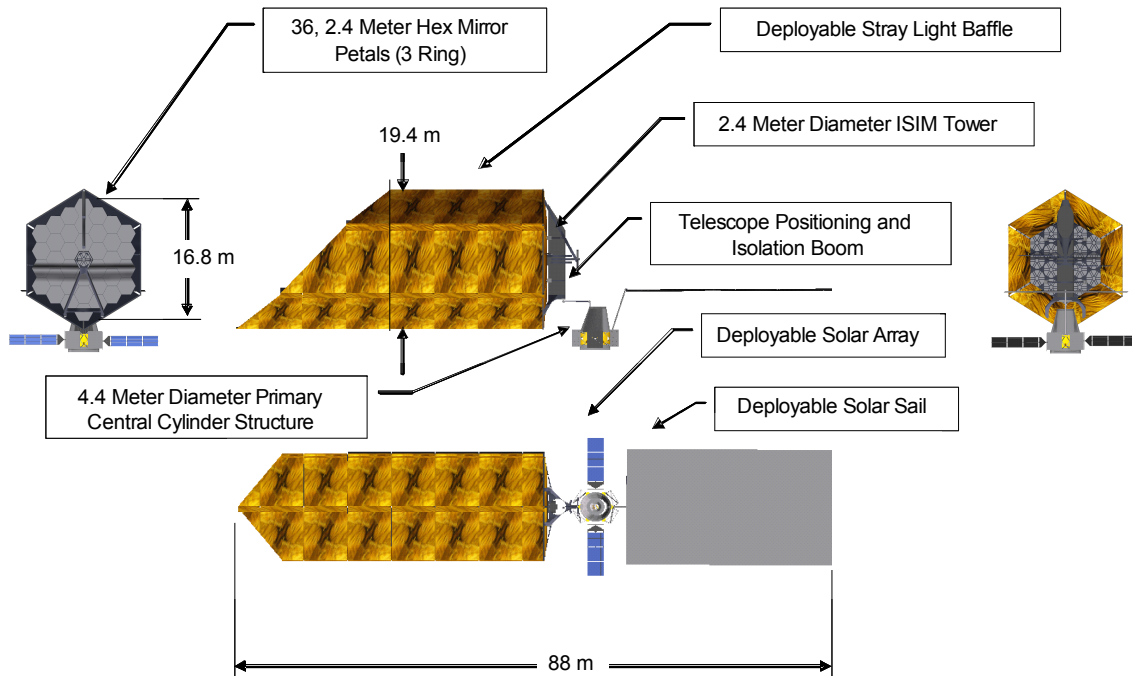


**Figure E-1.** *ATLAST* 16.8-meter Telescope Design Concept

Our conceptual design for the *ATLAST* 16.8-m telescope is shown in Figure E-1. The 36-segment, *JWST*-derivative chord-fold telescope is enclosed in a deployable sunshade, which provides a stray light baffle and shroud for telescope thermal control. The sunshade has a ~45 degree “scarf” so the telescope can observe as close as ~45° from the sun. An integrated science instrument module (ISIM) is mounted on the back of the telescope, which is attached to the spacecraft with a positioning boom that provides thermal and dynamic isolation for the payload.

The spacecraft bus has a 4.4-m diameter central cylinder that provides the primary load path from the launch vehicle to the payload during launch. The spacecraft subsystems are housed in modules attached to this central cylinder, as are two solar array wings and a large, lightweight solar sail. The solar sail is sized to compensate for the ~16-m CP-CM offset that would exist if the solar sail was eliminated. With the addition of a two-axis gimbal to the boom attaching the solar sail to the spacecraft bus, the sail could also be used to modulate the solar radiation torque and “unwind” the reaction wheels without using the spacecraft’s reaction control (propulsion) system.

The location of the CM and CP for the 16.8-m *ATLAST* the absence of the solar sail is shown in Figure E-2. Three quarters of the mass is concentrated in the primary mirror of the telescope, plus the ISIM and the spacecraft bus, while sunshade has ~ 80 % of the surface area.

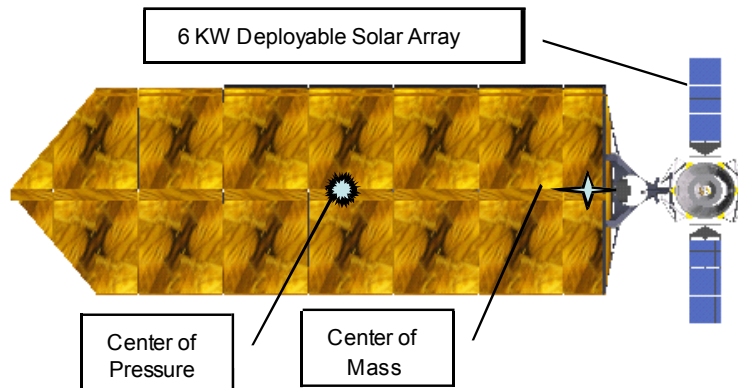


**Figure E-2.** CP – CM Offset for 16.8-m *ATLAST* without a Solar Sail

The solar torque acting on the 16.8-m *ATLAST* with and without a solar sail is shown in Table E-1. We assume that with the solar sail the CP-CM offset can be held to less than 10 cm, either by careful rigging of the solar sail before launch or by adjusting the solar sail’s orientation on-orbit with a two-axis gimbal at the end of the solar sail boom. Without the solar sail, the CP-CM offset will be ~16 meters and the solar torque will be ~100 times greater.

**Table E-1.** Solar Radiation Torque Acting on the *ATLAST* 16.8-m

Parameter	Symbol	With Sail	Without Sail	Units
Solar Constant	$P_S$	4.617E-06	4.617E-06	N/m <sup>2</sup>
Surface Area	$A_S$	1288	781	m <sup>2</sup>
CP-CM offset	$L_S$	0.1	16.1	m
Reflectance	$q$	0.6	0.6	
Angle of Incidence	$i$	0	0	deg
<b>Solar Torque</b>	<b><math>T_{SP}</math></b>	<b>9.52E-04</b>	<b>9.30E-02</b>	N-m

The momentum storage requirements for the two configurations are shown in Table E-2, and the specifications for some currently available reaction wheels and the space station control momentum gyros (CMG) s are shown in Table E-3. With the solar sail, six Honeywell HR-16 reaction wheels (among the largest wheels currently available) can easily meet the solar torque requirement, and can store the momentum buildup due to the solar torque for as long as 11 days. Without the solar sail, wheels with an order of magnitude greater momentum storage capacity would have to be developed to store the momentum buildup for just one day of operations.

Alternatively, we could use CMGs such as those developed for the International Space Station (*ISS*). Six of the *ISS* CMG’s could stabilize the 16.8-m *ATLAST* telescope for >3.5 days; a factor of three increase in their capacity would enable them to stabilize the telescope for ~11 days.

**Table E-2. Reaction Wheel/Momentum Storage Requirements for *ATLAST* 16.8-m**

Parameter	With Sail	w/o Sail (10x HR16)	w/o Sail (ISS wheels)	Units
Solar Torque	9.52E-04	9.30E-02	9.30E-02	N-m
Number of Days	11	1.12	3.55	days
Momentum Buildup	904	9000	28500	N-m-sec
Wheel Capacity	150	1500	4760	N-m-sec
<b>Number of Wheels</b>	<b>6.03</b>	<b>6.00</b>	<b>5.99</b>	

When the capacity of the reaction wheels is reached, the stored momentum must be “dumped” by firing the spacecraft thrusters. The mass of the propellant required to dump the momentum [28] is:

$$\Delta m = \frac{l}{(g I_{SP} r)}$$

where  $\Delta m$  is the mass of propellant,  $l$  is the stored angular momentum,  $g$  is the Earth’s gravitational acceleration (9.80665 m/sec<sup>2</sup>),  $I_{SP}$  is the specific impulse of the thruster, and  $r$  is the distance between the thruster and the center of mass.

**Table E-3. Specifications for Some Currently Available Reaction Wheels and the *ISS* CMGs**

Manufacturer	Model	Capacity (N-m-sec)	Torque (N-m)	Speed (rpm)
Honeywell	HR12	25	0.2	±6000
Ithaco	E	26	0.3	±2000
Teldix	RSI-30 280/30	30	0.28	±3000
Teldix	RSI-68 170/60	68	0.17	±6000
Honeywell	HR16	150	0.2	±6000
L3 Space & Nav.	DGCMG 4800/250	4760	280	6600

Table E-4 shows the propellant requirements for momentum dumping for the two *ATLAST* configurations. With a solar sail to align the CP and CM, a simple monopropellant propulsion subsystem would only require ~10 kg of hydrazine to dump the momentum during a ten year mission. By comparison, without a solar sail the *ATLAST* 16.8-m would require ~700 kg of propellant with a more complex bi-propellant propulsion subsystem, or > 1,000 kg of hydrazine.

Without the solar sail *ATLAST* would face several more challenges. In addition to requiring the development of a new reaction wheel, and the packaging challenges of accommodation the larger wheels and additional fuel, firing the thrusters every day would complicate tracking and navigation for *ATLAST* in its SE-L2 orbit. Since firing the thrusters invariably imparts some translation (delta-V) as well as rotation to the spacecraft, each thruster firing creates uncertainty in the tracking solution. For the *JWST* mission, the GSFC guidance and navigation group has limited thruster firings to once every 11 days, with a goal of once every 22 days. Developing a CMG with ~15,000 N-m-sec capacity would satisfy the tracking requirement, but would face similar packaging issues. Another factor to consider in the solar sail

trade is the disturbance force due to imbalances in the rotating wheels of the reaction wheels and CMG's. Vibration induced jitter should be a couple of orders of magnitude smaller with the 150 N-m-sec Honeywell reaction wheels and solar sail, avoiding the requirement for a complex vibration system.

**Table E-4. Momentum Dumping Propellant Requirements for *ATLAST* 16.8-m**

Parameter	Symbol	With Sail	w/o Sail (10x Honeywell HR16 capacity)	w/o Sail (ISS reaction wheels)	Units
Built up angular momentum	$l$	904	9000	28500	N-m-sec
Specific impulse of the fuel	$I_{SP}$	210	310	310	sec
Distance from thruster to CM	$r$	14.12	14.12	14.12	m
Mass of fuel required (per firing)	$\Delta m$	3.11E-02	2.10E-01	6.64E-01	kg
Type of fuel		Hydrazine	Bi-prop	Bi-prop	
Thruster model	M	MRE-1	SCAT	SCAT	
Thruster force	F	4.45	44.5	44.9	N
Burn Duration	t	14.40	14.33	45	sec
Days between Mom. Dumps	d	11	1.12	3.55	days
Observatory Lifetime	L	10	10	10	years
Number of thruster firings	n	332	3261	1029	
<b>Propellant required</b>	<b>P</b>	<b>10.3</b>	<b>684.8</b>	<b>683.3</b>	<b>kg</b>

The 8-m *ATLAST* telescope has a similar requirement for solar torque mitigation. The ISS CMG's should have sufficient momentum storage capability for the current 8-m *ATLAST* design, but will require several layers of vibration isolation to meet the  $\sim 1.6$  milli-arcsecond jitter requirement.

An alternative approach to solar torque mitigation has been adopted for the *ATLAST-9.2m* concept. It has a flat sunshield similar to that developed for *JWST*, with a segmented, chord-fold telescope mounted on a positioning boom similar to that proposed for *TPF-C* and *SAFIR* [29], and recently patented [30] by Northrop Grumman. Gimbals at the spacecraft and telescope ends of the boom allow the telescope to be pointed through a  $\sim 3\pi$  steradians field of regard while the sunshield remains normal to the sun-line. It also permits the center of mass of the telescope to be aligned with the center of pressure of the sunshield to minimize solar torque, or to misalign the CP and CM and use the solar torque to dump momentum stored in the reaction wheels of the spacecraft bus. The positioning boom has a natural frequency of  $\sim 0.3$  Hz, with also provides vibration isolation for the telescope and instruments.

## Appendix F. Optical Design and Active Optics System for the *ATLAST-16m* Concept

The initial *ATLAST-16m* conceptual design derives its basic configuration from *JWST*. At the time *ATLAST-16m* could be launched (ca. >2027), *JWST* will have completed its mission. Its lessons learned could be captured in an evolved, enlarged version, which would use or reuse similar deployment mechanisms, similar structures, and similar spacecraft subsystems.

### *Basic Optical Design*

The most obvious design requirement is a 16-m entrance pupil diameter (EPD). For the design we have chosen (see below), the entrance pupil is at the primary mirror. No launch vehicle proposed for the near future has the capability of launching a monolithic 16-m mirror. Therefore, the aperture size of the telescope dictates that it must be deployable and hence segmented. A segmented primary mirror is not a new concept but the telescope proposed here would be the largest segmented, space telescope ever built. We envision that the segments would be 2.4 meter, hexagonal mirrors and would be lightweight like the actuated hybrid mirrors (AHM) described in Appendix H. The primary/secondary mirror separation scales with EPD to some extent. In order to minimize mass and volume, we have constrained the focal ratio of the primary mirror to be less than 1.5. However, even with this fast primary mirror, the secondary mirror structure will have to be deployed. Note that a fast primary also increases the stability of the secondary mirror alignment. This is an important consideration given the wavefront requirement given below.

The minimum wavefront quality, derived from our science requirements, must yield images that are diffraction-limited at 500 nm. In terms of RMS wavefront error (WFE), this gives a total allowed error of 36 nm. That total WFE must be parsed between design, static, and drift. The static includes rigid-body misalignment and segment figure errors while the drift is mostly the result of changes to the bulk temperature and temperature gradient. As a strawman allocation, we have assigned 20 nm RMS WFE to the design. The static and drift terms are allocated 22 and 20 nm RMS respectively. It is the 20 nm RMS drift term that necessitates a wavefront sensing and control system (WFS&C). Sensors for the WFS&C subsystem consist of (1) a metrology system that forms an optical truss between the primary mirror segments and the secondary mirror, and (2) cameras for measuring the wavefront drift. The WFS&C system is discussed in more detail later in this appendix.

We have chosen a Ritchey-Chretien (RC) design form for the front-end telescope. This variation on the classical Cassegrain design uses a hyperbolic primary and secondary mirror. The light from the telescope is split into two channels by field: the center of the field goes to a narrow field-of-view (NFOV) channel that contains the UV spectrograph and exoplanet science instrument (e.g., a visible nulling coronagraph) and the remainder of the field goes to a wide-field (WFOV) channel that contains the gigapixel imaging array, an IFU, and a multi-object spectrograph. This division by field is accomplished using a fold mirror with a hole in the center. Light going to the NFOV channel passes through the hole while the light for the WFOV is reflected. This separation scheme is consistent with the desire to minimize the number of reflections in the NFOV channel.

The division of light going to the NFOV instruments can be handled in one of two ways. If the spectral bands of the two instruments do not overlap, then the light can be spectrally divided with a dichroic beam splitter. In this case one instrument would see an additional reflection and one a transmission through two interfaces. If there is spectral overlap, the separation can be done spatially with a fold mirror. In this case, only one instrument would see an additional reflection. The Cassegrain telescope that precedes the NFOV channel is shown in Figure F-1.

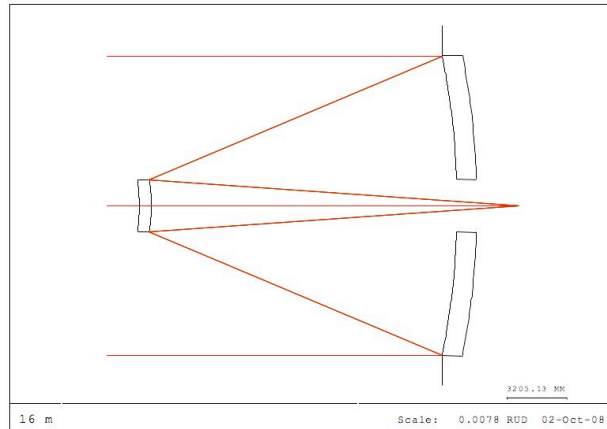


**Figure F-1.** The optical layout of the NFOV channel.

The WFOV channel is a more complicated design. The performance of the front-end RC telescope is not good enough over the required field and additional powered elements are necessary. Furthermore, by compressing the beam one can reduce the mass, volume and cost of the WFOV instruments. Thus, a three-element beam compressor follows the two powered elements. This combination of five elements performs the following functions: (1) significantly improves the wave front over the required field; (2) compresses the beam to 310 mm (a compression factor of  $\sim 52$ ); (3) produces an accessible pupil in collimated space. The WFOV channel is shown in Figure F-3 without the fold mirror (*i.e.*, unfolded) that separates it from the NFOV.

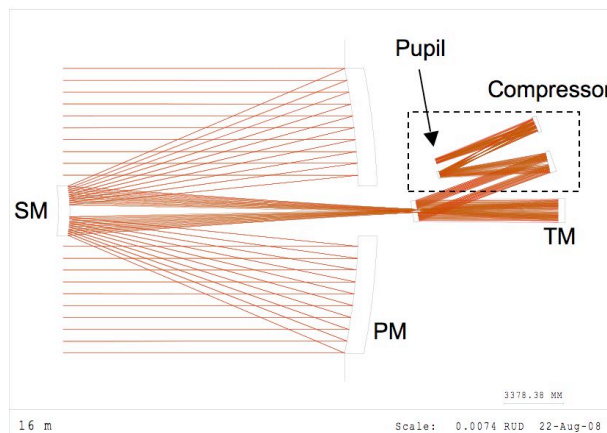


**Figure F-2.** The optical layout of the WFOV channel.

The optical performance for the NFOV and WFOV are shown in Figures F-3 and F-4, respectively. The WFE for the NFOV has azimuthal symmetry while the WFOV has symmetry about the vertical axis in Figure F-4. The NFOV wave front is evaluated at the Cassegrain focal

plane over a circular field 7.5-arcsec in radius. The WFOV wave front is evaluated at the re-imaged pupil over a square field of  $\pm 2$  arcminutes. The WFE for the NFOV is essentially zero (i.e.,  $< 0.003$  nm RMS) for all field points of interest. The performance for the WFOV channel, averaged over the field of interest, approximately meets the 20 nm RMS requirement although individual field points exceed this value.

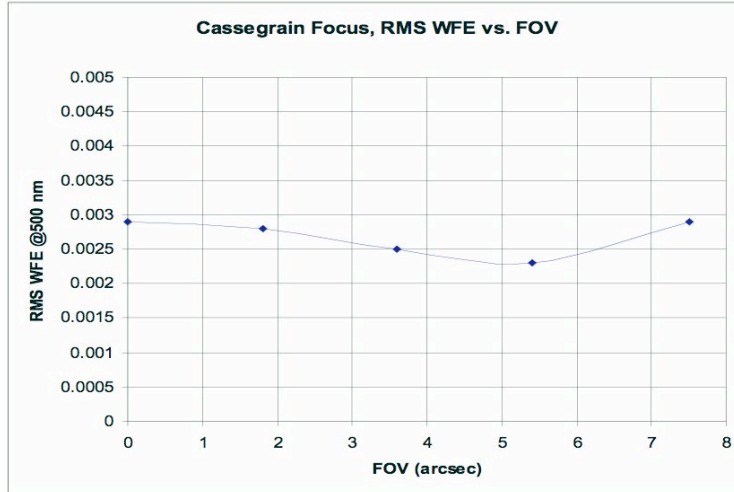


Figure F-3. Optical performance as a function of field position for the NFOV channel.

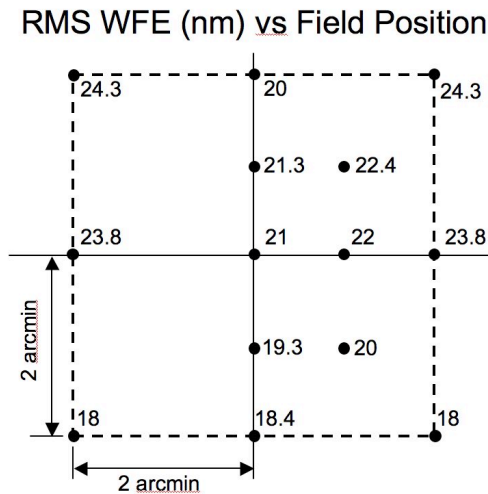


Figure F-4. Optical performance as a function of field position for the WFOV channel.

### Active Optics System

The *JWST* active optics architecture provides an appropriate starting point for an *ATLAST-16m*, but certain refinements will be needed. *JWST* is a cryogenic, infrared mission that is diffraction-limited at 2000 nm wavelength. *ATLAST-16m* will be a visible light telescope, with extension into the UV, that will be diffraction-limited at 500 nm wavelength for all imaging modes. In coronagraphic imaging modes it will need to be very much better, to provide the required contrast. The fundamental WF quality will need to improve from 140 nm to under 36 nm RMS, during all operations.

As noted, *ATLAST-16m* will be equipped to characterize the atmospheres of terrestrial-mass exoplanets. If the associated starlight suppression is performed using an internal coronagraph or

interferometric nuller than that instrument will require extremely good WF quality and stability (<0.001 waves WF error).

The particular method chosen for high-contrast imaging will have an impact on the requirements for telescope WF error and telescope WF stability:

- The possible inclusion of a second stage of active optical control in an internal coronagraph – one or more high-resolution Deformable Mirrors (DM) – would permit extremely good WF correction for the exoplanet science instrument field, as has been demonstrated on the *TPF* High Contrast Imaging Testbed. It would relax the required telescope WF performance by correcting the WF from the 40 nm residuals provided by the *ATLAST-16m* telescope, to the needed performance of well below 1 nm RMS. The need for telescope WF stability of  $\ll 1$  nm would remain.
- The further inclusion of an active WF sensing system in the coronagraphic instrument would potentially relax both the required telescope WF performance and the required telescope WF stability.
- Possible use of a “starshade” external occulter – a 90-meter class obscuring disk, precisely placed at a distance of ~180,000 km from the *ATLAST-16m* observatory – provides another option for high-dynamic range imaging. This completely separate spacecraft would need to be operated in close conjunction with *ATLAST-16m*, to keep it precisely positioned. The use of a Starshade would relax *ATLAST-16m* WF requirements substantially.

#### *Active Optics Architecture*

*ATLAST-16m* will utilize *JWST* technologies as a starting point for its adaptive optics. *JWST* active optics are of the “set-and-forget” variety. *JWST* will be launched, deployed, and then the Wavefront Sensing and Control (WFS&C) system will move the PM segments to align and phase the telescope. *JWST* segment Radius of Curvature (RoC) errors will be compensated by a single deforming actuator per segment. There is no continuous maintenance system for *JWST* – its optics will be reset only infrequently (1/day to 1/month), using WFS&C.

*ATLAST-16m* will exist in a different performance and environmental regime. *ATLAST-16m* WFE requirements are tighter, *ATLAST-16m* dimensions are larger, *ATLAST-16m* wavelengths are much shorter, and *ATLAST-16m* will not be cryogenic. *ATLAST-16m* WFE will be far more sensitive than *JWST*, and a purely passive approach will not work. This is especially true if the telescope active optics are required to meet exoplanet science WF and WF stability performance levels. As a result, we are baselining an active optical metrology system, to provide continuous, low-bandwidth segment “rigid-body” control, and segment thermal control, to keep the segments from changing shape.

Key features of the *ATLAST-16m* telescope architecture will likely include:

- Lightweight primary mirror segments, equipped with actuators to permit figure correction. Our baseline approach is to use Actuated Hybrid Mirrors with nanolaminate foil facesheets, as they have a high level of controllability and can be manufactured by replication. Figure F-5 shows an example. It will be desirable from an exoplanet imaging point of view to have the largest size segments possible, with 2 m or greater being a technology goal.

## Advanced Technology Large-Aperture Space Telescope (ATLAST)

- Wavefront Sensing and Control, for initial alignment and figure control, and for periodic wavefront maintenance.
- Metrology of the full beam train, to provide continuous low-bandwidth, full-field, real-time WF control. Our baseline approach is to use Laser Distance Gauges (LDGs) organized into a Laser Truss that is capable of measuring the full optical state of the telescope at high bandwidth. This approach builds on technology originally developed for the Space Interferometry Mission (*SIM*). We will discuss other options, such as edge sensors and full-time WF sensing.
- Active thermal control of key optical elements, namely the PM segments and the Secondary Mirror. Thermal control will preserve the figure of the segments without the need for frequent WF sensing.
- Integrated on-board data processing, using WF sensing, metrology, thermal, and inertial attitude measurements in an on-board Optical State Estimator/Active Alignment Control process. The OSE utilizes Kalman filtering to optimally exploit all available information to drive low bandwidth wavefront control, so as to assure highly stable WF and pointing performance even in a changing thermal environment.

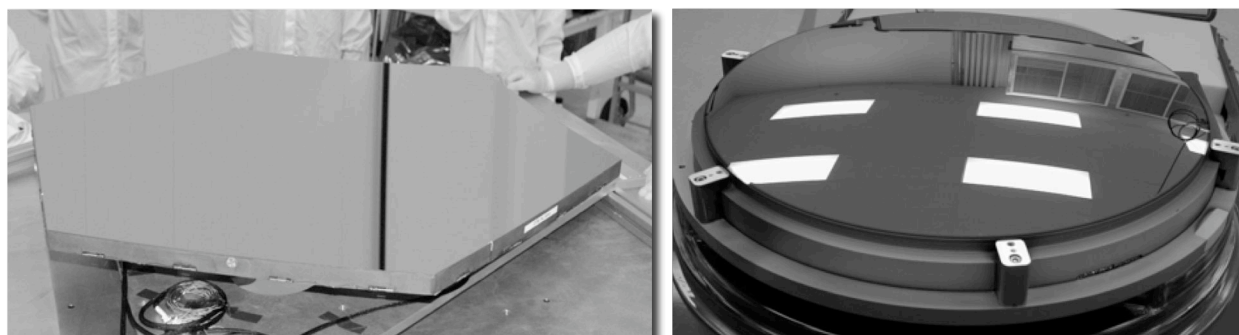


**Figure F-5.** Actuated Hybrid Mirror (AHM) segment and mandrel.

A sketch of this architecture is provided in Figure F-6. As shown, the major disturbances to the *ATLAST-16m* telescope WF quality include static fabrication errors, such as optical figure errors; slow thermal changes incurred as the telescope changes pointing angle and sun illumination; and fast dynamical errors imparted from on-board machinery such as attitude control actuators. Vibration effects will be compensated by isolation of the disturbance source and by damping of the spacecraft and telescope structures.

The actuators embedded in the AHM segments will compensate for static fabrication errors using the WFS&C control loop indicated on Figure F-6. As described later, this will be quasi-static (or very low bandwidth) control utilizing images of stars taken in the *ATLAST-16m* cameras processed on the ground, with actuator voltages uplinked for implementation. This control will also reset both the figure and the alignment of the telescope optical system. The control will optimize the combined WF error of all the optics of the telescope, at all field positions.

Thermal and other environmental effects will be compensated by 2 separate control loops. The first is the Segment Thermal Control (Fig. F-6), which uses temperature sensors attached to the segments, along with local heaters, to keep the segments at a constant temperature and so at a

constant figure. The performance of this local thermal control will likely need to be well below  $1^\circ\text{C}$ , but is not expected to pose a technology challenge.

The second line of defense against environmental effects is provided by metrology of the optics in the telescope. As described below, our baseline approach is a Laser Truss that precisely measures all telescope optics – PM segments, SM, the Instrument Bench – with respect to each other. The Laser Truss will measure at very high bandwidth – 1 kHz or faster – to ensure that it observes all motions of the telescope without losing track of interference fringes.

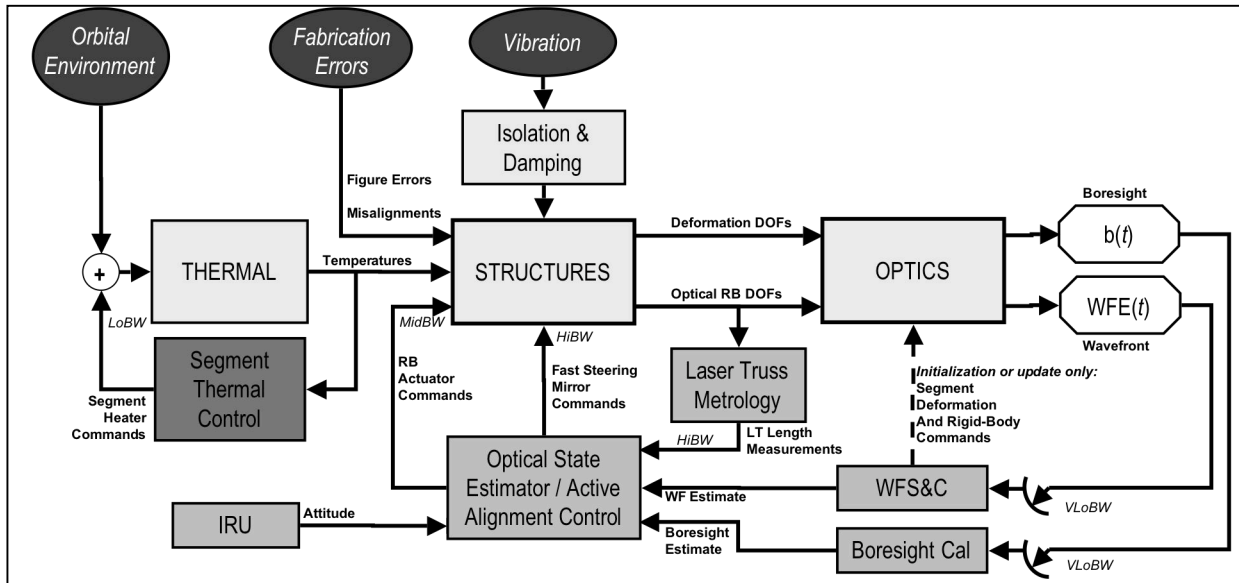


Figure F-6. ATLAST-16m Active Optics block diagram.

We expect that an Inertial Reference Unit will be mounted to the Instrument Bench and measured by the Laser Truss together with the optics. The IRU, composed of star-trackers and gyroscopes, is capable of measuring the telescope inertial attitude to great precision. By including it in the Laser Truss path, we have a means of measuring the optics directly in inertial space. As a result, the Optical State Estimator (OSE) [38] can accurately estimate the inertial pointing direction of the telescope as well as the WF error, from the Laser Truss measurements.

Line-of-sight control must also be provided. *ATLAST-16m* will use a Fast Steering Mirror (FSM) to stabilize its pointing direction to required accuracies. The FSM control loop can be driven directly from the metrology signals plus an Inertial Reference Unit, composed of star-trackers and gyroscopes, and capable of measuring the telescope inertial attitude to a small fraction of a pixel. Using this approach, very high bandwidth control is possible, in an open-loop mode.

A slower but more accurate approach would be to use a Fine Guidance Sensor to guide on a star in a closed loop, as is planned for *JWST*. In general such a star will be dim and will require integration times longer than the Laser Truss time constants, supporting closed loop bandwidths of 10 Hz or so. These signals will be processed by the OSE to optimally blend them with IRU and Laser Truss measurements, to provide both high accuracy and high bandwidth. Our study will determine the requirements that must be met and identify pointing control technology shortfalls that may exist.

The OSE needed for the *ATLAST-16m* is similar to the Optical State Estimator originally proposed for (but not used for) *JWST* Integration and Test. It will utilize Kalman Filter

techniques to combine all sources of information and balance measurement noise against prior knowledge errors. OSE error growth will be limited by periodic WFS&C updates. The OSE signals will be low-pass filtered before control commands are sent to the segment and SM rigid-body actuators that control telescope alignments.

OSE and Active Alignment Controller on-board implementation will depend on the number of states that must be carried, which will depend on the numbers of segments and other optics, the number of deformation modes to be tracked, the numbers of actuators and other considerations. Our study will assess on-board computing requirements as details of the optical design emerge.

**Wavefront Sensing and Control: Initialization and Updates**

*ATLAST-16m* operations will begin after launch and deployment of the telescope PM, SM and sunshade. The segments and the SM will be placed and oriented according to positions measured during ground testing; at this point WF error may be multiple millimeters. Then the telescope will be pointed at a bright, isolated star, and WFS&C initialization operations will be performed to bring the WF error from post-deployment values > 1 mm, to below the diffraction limit at 500 nm wavelength, or 36 nm. The WFS&C initialization of *ATLAST-16m* will be very similar to the initialization of *JWST*, except for three things: first, the presence of a metrology system will provide an accurate position servo mode for commanding displacements of the segments and SM; second, the metrology system may have an absolute mode with 1-2 micron accuracy that will significantly speed up correction of post-deployment errors; third, that the *ATLAST-16m* segments will have many deforming actuators (200-1000 or so vs. 1 for *JWST*), and so higher capture range and higher accuracy WF sensing is required. The latter consideration drives us to include a Shack-Hartmann Camera (SHC) (or a Shack-Hartmann mode in the visible imager) in the *ATLAST-16m* instrument suite. Figure F-7 shows how the very large initial WF error will be reduced by WFS&C.

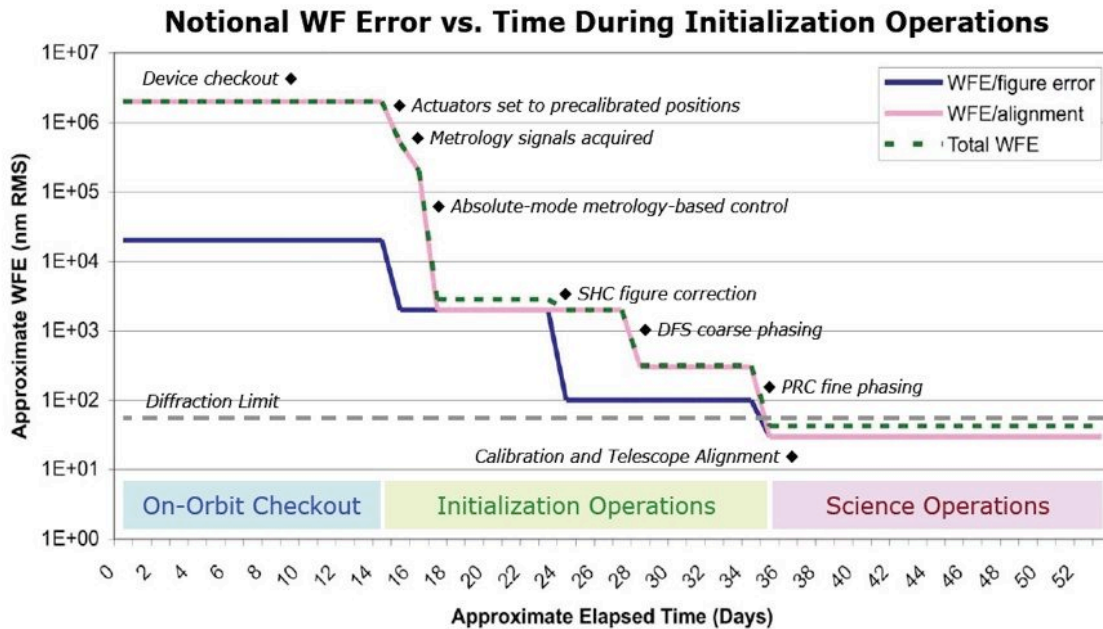


**Figure F-7.** Notional WFE vs. Mission Time during initialization of the *ATLAST-16m* telescope. (SHC=Shack-Hartmann Camera, DFS=Dispersed Fringe Sensing, PRC=Phase Retrieval Camera)

The initial WFS&C operations will likely follow this sequence:

- Metrology system is activated, and metrology signals are acquired, possibly by scanning segments in angle to maximize power return. With the metrology system active, subsequent actuations can be performed in a precise servo mode, with position feedback assuring that commanded displacements are precisely executed.
- Using absolute mode metrology measurements, PM segments and SM are placed within a few microns of their required position.
- Coarse Alignment: with the telescope staring at a bright, isolated star, the segments are scanned in angle to associate segment sub-images with particular segments.
- Shack-Hartmann figure correction. The SHC provides a large capture-range measure of segment figure, but not segment piston errors, as the SHC is insensitive to discontinuities at segment boundaries. This allows the segments' figure errors to be corrected to a reasonable accuracy, but does not establish a phased WF.
- Coarse Phasing: Dispersed-Fringe Sensing (DFS), using the visible camera with an inserted grism, or the visible spectrometer, to phase the segments. DFS is a technique whereby the light from 2 subapertures (segments or groups of segments), with a piston error  $dL$  between them, is interfered at a common focus, and dispersed to create a spectrum (Figure F-8). The wavelength of the light varies monotonically along the spectrum, and where  $2dL$  is an integer multiple of the wavelength, a bright fringe is generated; where  $2dL$  is  $(n + 0.5) \lambda$ , a null is generated. Taken together, the spectrum becomes a fringe pattern whose period is a precise measure of  $dL$ . The slope of the slant angle of the fringe indicates which subaperture is higher than the other, so the DFS measurement is unambiguous. With  $dL$  measured, the subapertures can be moved into phase. DFS techniques are documented in [39]; testing of the DFS on the Keck II Telescope is shown in Fig. F-9 and described in [40].
- Fine Phasing: Phase Retrieval WF sensing. Using the visible imager (the Phase Retrieval Camera or PRC), a sequence of out-of-focus images of the guide star is recorded and downlinked to the ground. These images are then processed using the Modified Gerchberg-Saxton software to produce a detailed WF map, showing the cumulative effect of all of the optical errors of the system [41]. An example using a simulated 36-hex *ATLAST-16m* is provided in Figure F-10. MGS phase retrieval is highly accurate, demonstrating 1/10,000 accuracies in stable, vacuum measurements on the HCIT [42]. It has a dynamic range of over 10<sup>1</sup>, as demonstrated (for instance) on the Advanced Mirror System Demonstrator prototype JWST segments [43]. MGS has been used on many hardware platforms; it was awarded NASA's 2007 Software of the Year Award.
- Multi-Field WF sensing. Phase retrieval is repeated in all of the science cameras, at 5 or more field points, to measure the WF variation across the field of each. This information is used to estimate the misalignment of the PM, SM and Instrument Bench with respect to each other. The SM and the PM segments are realigned as needed and the process is repeated until the telescope is fully aligned. This process also measures the camera-to-camera non-common path WF error, which will be used during WFS&C updates to optimize performance over all instruments. Multi-field WFS is described in [44].

This full procedure will be needed only once, at the beginning of the *ATLAST-16m* mission. A reduced set of measurements (single-field phase retrieval only) will be performed on a regular basis, perhaps weekly, to confirm that the metrology system has not drifted and that the WF error is in specification.

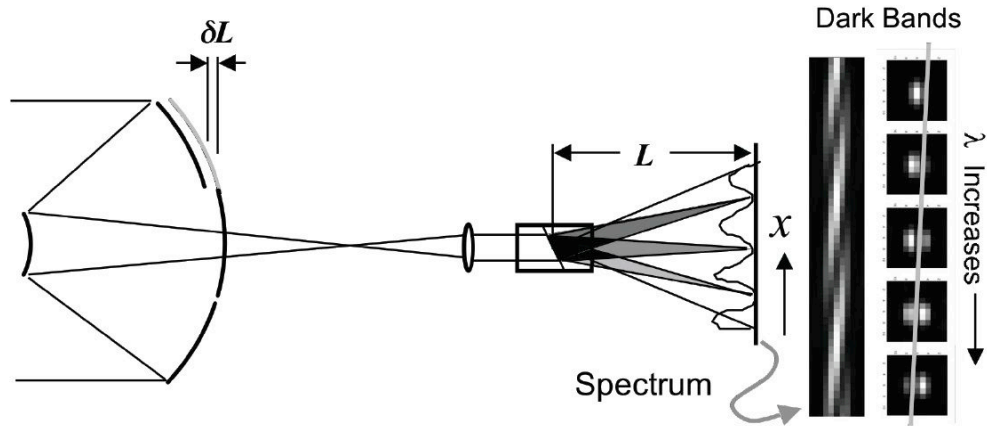


**Figure F-8.** Dispersed Fringe Sensor, showing how a grism inserted into the PRC imaging path modulates sub-aperture phase differences.

### Wavefront Maintenance Control

Initial WF Sensing and Control establishes good optical quality for the telescope; it also establishes the metrology set-point – the 3D configuration settings that will be maintained by position measurements and rigid-body actuator feedback. This Maintenance Control function can be, and has been, performed multiple different ways. The *Keck* Telescopes, for instance, make excellent use of edge sensors, devices inserted between segments that are sensitive to piston differences between segment edges. Ground-based adaptive optics using full-time WF sensing is effective for correction of atmospheric turbulence effects.

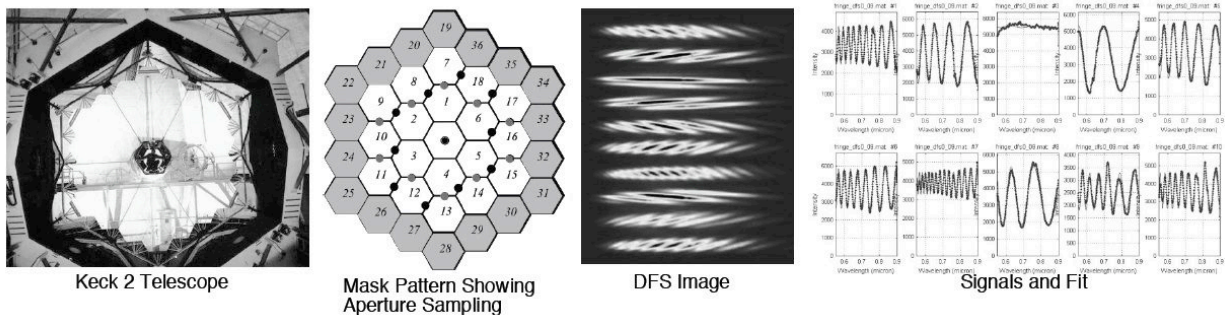


**Figure F-9.** Dispersed Fringe Sensing experiment at the *Keck II* Telescope, showing aperture mask used to select sub-aperture patches for fringe generation, a stellar DFS fringe image, and the trace of the processed signals and the fit to the signals. A *JWST*-style “Dispersed Hartmann” prism array was used to image 10 fringes at a time to reconstruct the phasing of the inner 18 segments.

Our baseline approach is to use a Laser Truss metrology system, formed from multiple Laser Distance Gauges (LDGs) as described in this section. Compared to edge sensors, the LT offers better observability of the segment rigid body errors, and more importantly, it measures the SM and Instrument Bench as well as the PM segments, permitting estimation of all of the optically

significant displacement Degrees of Freedom (DOF). Compared to full-time WF sensing, the LT is useable when there is no guide star in the scene; it also provides measurements that enable preservation of optical quality across the full telescope field.

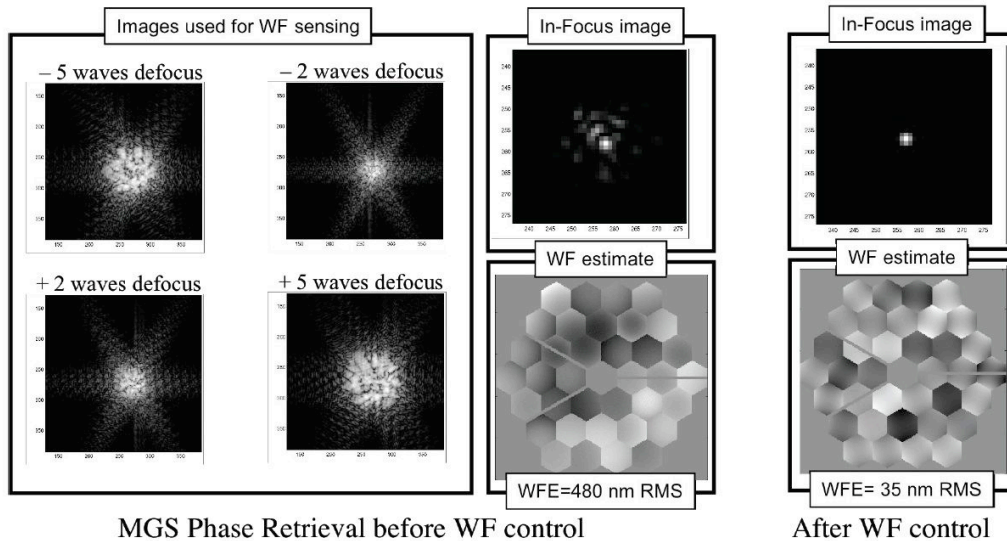


**Figure F-10.** A phase retrieval WF sensing example, showing defocused images taken with a simulated 36-segment telescope, with wavefronts and in-focus images taken before and after WF control.

At the conceptual level, a Laser Distance Gauge (LDG) is a “yardstick,” with “inchmarks” provided by the interference fringes of the laser beam. Changes in the distance  $d$  between the Beam Launcher (BL) and the Corner Cube (CC) are measured as phase shifts between input and output beams. Heterodyne detection techniques provide intrinsic accuracy very much smaller than 1 wave. By “counting fringes,” those accuracies can be extended to large changes in  $d$ . These measured changes can be fed back to actuators that precisely regulate  $d$  to preserve any desired value.

*SIM* has developed LDGs with extremely good accuracy (<100 picometers) in a fringe-counting relative-metrology (“RelMet”) mode; and, using 2 laser frequencies to generate a long synthetic wavelength, *SIM* LDGs provide 5 mm capture range in an “AbsMet” absolute mode. Accuracy of the LDG AbsMet mode is about 1  $\mu\text{m}$ . The *SIM*-derived LDGs can be run at bandwidths in excess of 1 kHz.

Light-weighting of the *SIM* LDG technology has been explored under JPL internal research funding. It was found that the LDG Beam Launcher could be reduced to a mass compatible with mounting directly on an AHM segment. This advantage comes at the cost of reduced performance, with accuracies on the order of 1 nm expected. This performance is adequate for most *ATLAST-16m* requirements, but further improvement would be necessary if the telescope stability is to meet the tightest exoplanet detection WF stability requirements. Other LDG technologies are also under consideration.

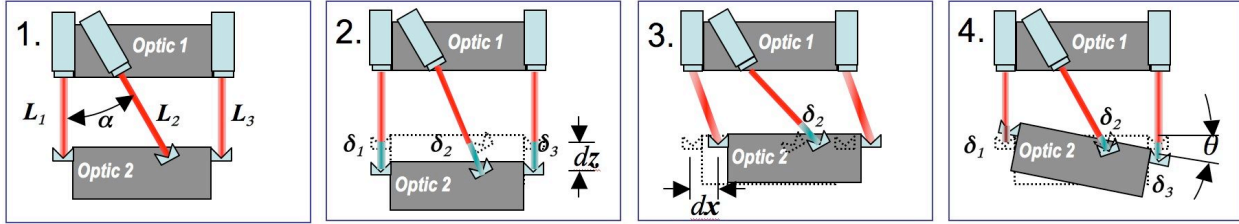


Figure F-11. A 2-dimensional laser truss.

LDGs can be combined in series and in parallel, to measure the relative displacement and rotation of multiple bodies. Figure F-11 shows an example using 3 LDGs to measure the 3 DOFs between 2 2-dimensional bodies. In this simple case, the BLs are attached to Optic 1, illuminating corner cubes on Optic 2. Motions of Optic 2 with respect to Optic 2 include displacement DOFs  $dx$  and  $dz$ , plus rotation  $q$ . These DOFs define the optical state vector  $x = [dx \ dz \ q]^T$  of this system. The measurements along each LDG are  $\delta_1$ ,  $\delta_2$  and  $\delta_3$ , which are related to the DOFs (to first order) by the measurement equation:

$$\delta = \begin{bmatrix} \delta_1 \\ \delta_2 \\ \delta_3 \end{bmatrix} = \begin{bmatrix} 0 & 1 & r_1 \\ \sin(\alpha) & \cos(\alpha) & r_2 \sin(\alpha) \\ 0 & 1 & r_3 \end{bmatrix} \begin{bmatrix} dx \\ dz \\ \theta \end{bmatrix} = Cx$$

Given a particular set of measurements  $d$ , this measurement equation can be inverted to estimate the optical state  $x$ , as:

$$x_{\text{est}} = C^{-1}d$$

This equation defines a simple OSE. The estimates  $x_{\text{est}}$  can be fed back to actuators on Optic 1 and/or Optic 2 to keep the system aligned.

The same approach can be extended to 3 dimensions, by using 6 BLs between each pair of optics to measure the 6 relative DOFs between them. It can also be extended to multiple optics – indeed, to all of the major optical assemblies in *ATLAST-16m* – by providing 6 BLs on each segment, illuminating CCs on the SM; with 6 BLs on the Fold Flat illuminating the SM CCs from below the PM; and with 6 BLs on the Instrument Bench illuminating 3 CCs on the Fold Flat, as sketched in Figure F-12. Finally, adding an Inertial Reference Unit on the Instrument Bench ties the whole thing to inertial space.

This system is described by a measurement equation of the same form as above, but with much larger state and measurement vectors  $x$  and  $d$ . In this case, there will be  $n_{\text{LDG}} = 6 n_{\text{seg}} + 12$  total LDGs measuring the same number of states (3 rotational and 3 translation states per body). The measurement matrix  $C$  can be determined from the kinematics of the telescope structure in the same way as for the 2-D case.

The measurement equation is of full rank for the 3-D laser truss, so inverting the measurement matrix generates an estimate of the optical state. A better approach, where there is measurement noise, process noise, variation (however small) in the geometry of the truss, and additional information to include (such as the occasional WF measurement or boresight calibration), is to use an Optical State Estimator. The *ATLAST-16m* OSE will utilize Kalman Filtering techniques to produce optimal estimates of the full optical state  $x$ , balancing LT and WF sensing

measurement errors vs. prior knowledge of the state to make best use of all available information. For *ATLAST-16m*, the full state will include rigid-body displacements of the optics due to deformation of the underlying support structures, and figure deformation modes of the PM segments. It will likely not include structural dynamics terms.

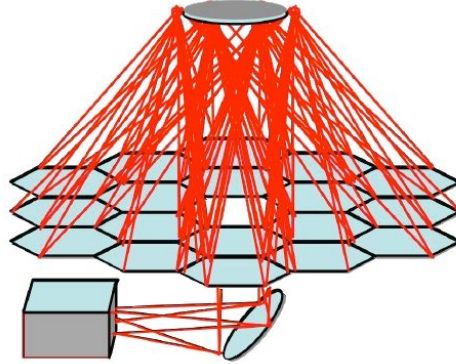


**Figure F-12.** A full 3-dimensional laser truss.

The OSE will likely have multiple time constants, executing the rigid-body part of the estimator at the sampling rate of the Laser Truss, providing updated state estimates at 1 kHz or better to support the fast pointing control loop bandwidths. The state Deformation states of the telescope need not be estimated as fast, as their fundamental response time will be minutes to hours. The OSE will likely not require continuous update of the Kalman gains.

The controls for the RB and deforming actuators will be generated directly from the state estimates. The controls will be formulated to minimize a weighted combination of WF error and actuator effort, subject to constraints such as stroke and voltage limits [45].

The Laser Truss metrology has a number of useful features:

- High accuracy in relative metrology mode. Preliminary research shows that a low-mass package can achieve  $< 1$  nm per LDG.
- High absolute capture range in AbsMet mode,
- The LT observes all of the important RB states. The LT measures the rigid-body states of the PM, SM, other key optics, and the Instrument Bench – enough to accurately estimate all of the DOFs that contribute to full-field WF error.
- Low drift. The LT will require a single laser feeding all LDGs through a fiber manifold. This laser will be actively stabilized to achieve  $10^6$ /day stability, which is sufficient to keep drift-related WF errors in specification.
- Low mass. Beam Launchers and Corner Cubes can safely be attached to lightweight optical structures.
- No on-segment power dissipation.
- Works with any number of segments or other optics, in nearly any configuration, including sparse apertures or missing segments. This feature means that the LT can provide useful support for telescope Integration and Test.

There are challenges to the LT implementation as well, including a need for careful alignment and high “perceived” complexity.

Our preliminary assessment is that the LT is best suited for *ATLAST-16m* metrology, but we will continue to explore other options. We note that next-generation ground-based telescopes such as the Thirty Meter Telescope are developing improved edge sensors [46] that address some of the problems with earlier designs. Other developments in LDG technology are also expected.

We have identified a baseline approach for *ATLAST-16m* active optics and for component technologies. These are sufficiently mature (TRL 4-8) to show feasibility of the baseline approach. Further technology development will be needed to mature some aspects of the baseline approach, especially the lightweight active primary mirror segments and the metrology systems for continuous low-bandwidth optical control.

Other approaches also offer significant promise for *ATLAST-16m* active optics, such as the segment edge sensor work being done for *TMT* and other ground-based telescopes [46], and work on alternative lightweight segments using glass or composite materials.

### ***Wavefront Error Budget for ATLAST-16m***

Active control of the *ATLAST-16m* Primary Mirror Segments and Secondary Mirror provides the ability to compensate large optical errors that might occur during fabrication, assembly, launch, or during operation on orbit. This memorandum quantifies that advantage for the *ATLAST-16m* conceptual design activity.

Figure F-13 presents an error budget for *ATLAST-16m* in spreadsheet form. The budget is based on a representative high-resolution ray-trace optical model, in which starlight is propagated through the beam train to the system exit pupil, where the wavefront error is evaluated. The first derivative of the wavefront error with respect to small perturbations of each optic are computed in the form of sensitivity matrices. These matrices provide a detailed linear model of the wavefront error as a function of a long list of component errors – the Degrees of Freedom summarized in the leftmost column of the spreadsheet. The linear model is used to directly propagate the statistics of each component error to the wavefront, in a covariance analysis of the WF errors. This analysis also generates coefficients for use in the spreadsheet.

The linear model of the optics includes the effect of the Wavefront Sensing and Control system and the Laser Truss metrology system used to compensate drifts in alignment that occur during long observations [23]. In the spreadsheet depicted in Figure F-13, the 1-sigma standard deviation values for each type of component error are entered in the “Inputs” columns. The corresponding impact on WF error is shown in the pre- and post-wavefront control (WFC) columns. The “Initial Alignment” results show the performance immediately after a WF sensing and control update; the “Metrology Control” columns show the effect of thermal drift on WF error during observations; and the rightmost column sums the post-WFC, post-Metrology WF error for each component error. Total performance is rolled up on the bottom row.

9/1/08	Segmented Telescope WFE Budget		Initial Alignment				Metrology Control				Total WFE
	Degree of Freedom		Inputs		RMS WFE (nm)		Drift Inputs		RMS WFE (nm)		Post Metrology RMS WFE (nm)
	Values	Units	Pre WFC	Post WFC	Values	Units	Pre Metrology	Post Metrology			
Optical Telescope Assembly	PM Segment Tilt	5,000	urad	4,287,890	0.0	50	urad	42,879	0.0	0.0	
	PM Segment Piston	2,000,000	nm	3,638,571	0.0	1,000	nm	1,819	0.0	0.0	
	PM Segment Decenter	2,000,000	nm	94,159	0.5	1,000	nm	47	0.0	0.5	
	PM Segment Clocking	500	urad	56	0.1	15	urad	2	0.9	0.9	
	PM Low-order Figure (0-5 cycles/seg)	300	nm	578	5.9	2	nm	4	3.9	7.0	
	PM PSD Figure	6	nm	11	5.5	1	nm	1.8	1.8	5.8	
		0.003	c/mm			0.003	c/mm				
	PM Segment Mandrels	408	nm	816	6.0					6.0	
	PM Print Through	1,000	Pa	18	1.2					1.2	
	PM Thermal	18.0	deg C	1,904	2.9	0.020	deg C	2	2.1	3.6	
PM Nanolaminate Strain	26	deg C	2,218	3.9	0.000	deg C	0	0.0	3.9		
SM Decenter	SM Decenter	2,000,000	nm	258,751	0.0	2,500	nm	323	0.0	0.0	
	SM Piston	2,000,000	nm	2,620,916	0.0	2,000	nm	2,621	0.0	0.0	
	SM Clocking	2,500	urad	0	0.0	2,000	urad	0	0.0	0.0	
	SM Tilt	5,000	urad	1,337,236	0.0	120	urad	32,094	0.0	0.0	
	SM Low-Order Figure	30	nm	38	0.2	1	nm	1	1.3	1.3	
	SM PSD Figure	15	nm	35	2.9	1	nm	1	1.4	3.2	
		0.003	c/mm			0.003	c/mm				
Fold Flat	FF Decenter	2,000,000	nm	0	0.1	2,500	nm	0	0.0	0.1	
	FF Piston	100,000	nm	7,452	0.4	2,000	nm	149	0.0	0.4	
	FF Clocking	5,000	urad	0	0.0	2,500	urad	0	0.0	0.0	
	FF Tilt	100	urad	3,539	0.6	20	urad	708	0.0	0.6	
	FF Low-Order Figure	50	nm	64	0.4	1	nm	1	1.3	1.3	
	FF PSD Figure	10	nm	10	2.0	1	nm	1	0.9	2.2	
		0.005	c/mm			0.005	c/mm				
TM	TM Decenter	500,000	nm	4,813	0.3	2,500	nm	24	0.0	0.3	
	TM Piston	200,000	nm	10,311	0.8	2,000	nm	103	0.0	0.8	
	TM Clocking	5,000	urad	0	0.0	2,500	urad	0	0.0	0.0	
	TM Tilt	100	urad	3,531	0.6	20	urad	706	0.2	0.6	
	TM Low-Order Figure	50	nm	5	0.0	1	nm	0	0.1	0.1	
	TM PSD Figure	33	nm	6	0.6	1	nm	0	0.2	0.6	
		0.005	c/mm			0.005	c/mm				
FSM	FSM Decenter	2,000,000	nm	0	0.1	2,500	nm	0	0.0	0.1	
	FSM Piston	200,000	nm	2	0.8	2,000	nm	0	0.0	0.8	
	FSM Clocking	5,000	urad	0	0.0	2,500	urad	0	0.0	0.0	
	FSM Tilt		urad			50	urad	1	0.0	0.0	
	FSM Low-Order Figure	33	nm	7	0.0	1	nm	0	0.2	0.2	
	FSM PSD Figure	33	nm	17	1.8	1	nm	1	0.5	1.9	
	0.010	c/mm			0.010	c/mm					
Re-Imager	Decenter	100,000	nm	0	0.0	2,500	nm	0	0.0	0.0	
	Piston	200,000	nm	37	0.0	1,000	nm	0	0.2	0.2	
	RoC	0	nm	0	0.0	0	nm	0	0.0	0.0	
	Tilt	2,000	urad	3	0.0	100	urad	0	0.2	0.2	
	Low-Order Figure	33	nm	7	0.0	1	nm	0	0.2	0.2	
	PSD Figure	33	nm	6	0.6	1	nm	0	0.0	0.6	
	0.010	c/mm			0.010	c/mm					
Instrument Bench	Decenter	100,000	nm	0	0.0	2,500	nm	0	0.0	0.0	
	Piston	200,000	nm	50	0.0	1,000	nm	0	0.2	0.2	
	Tilt	2,000	urad	2	0.0	300	urad	0	0.3	0.3	
	Low-Order Figure	33	nm	4	0.0	1	nm	0	0.1	0.1	
	PSD Figure	33	nm	12	0.9	1	nm	0	0.4	1.0	
		0.010	c/mm			0.010	c/mm				
	Mid-f error	0	nm	0	0.0					0.0	
Hi-f error	3	nm	3	3.0					3.0		
Other	4	nm	4	4.0					4.0		
Metrology	Laser SNR		nm						6.0	6.0	
	Laser Frequency Drift		nm								
	Beam Launcher Thermal Drift		nm								
	Misalignment (TBD)										
WFC	WFS Error	3	nm	13	2.4		nm			2.4	
	PM RB Actuator Error	2	nm	0	1.6		nm	0	0.0	1.6	
	PM DM Actuator Error	2	V	0	0.0		units	0	0.0	0.0	
	SM RB Actuator Error										
	PM thermal ΔT	0.000	°C	0	0.0	0.100	°C	7	6.0	6.0	
WFE Summary	PM WFE			5,624,418	11.2			42,918	4.9	12.2	
	Everything Else			2,953,737	7.3			32,218	8.9	11.5	
	Design WFE	10	nm		10.0					10.0	
	Payload WFE									19.5	
	WFE Requirement									20.0	
WFE Margin									2.4%		

Figure F-13. Wavefront Error Budget for ATLAST-16m.

## Advanced Technology Large-Aperture Space Telescope (ATLAST)

The error model shows that the initial WF Sensing and Control system reduces large initial WF errors (6 mm) to very small values (13 nm). It also shows that the Metrology system keeps the drift errors, which uncorrected would be 50 microns, to about 17 nm. Combined, the WF error expected during observations would remain below 20 nm overall.

The component error values shown are a mixture of bottoms-up capabilities and top-down allocations, rolling up to the 20 nm overall WF error. The largest component errors are the initial alignment errors, in the mm/mrad range, reflective of a relatively relaxed assembly process. The correctability of these errors is very high, since these DOFs are directly actuated. The more difficult components are those that are not fully compensated by the WFC and Metrology controls. These include error components whose spatial frequency exceeds the bandpass of the WFC actuators, or segment figure drift that is not observed by the Laser Truss metrology. The error for these terms must be limited by achieving good surface roughness for the optics, and good thermal control to stabilize segment figure over the long term, consistent with the input values.

## **Appendix G: Summary of *ATLAST-9.2m* Design Study**

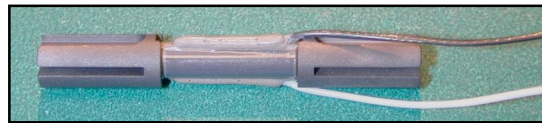
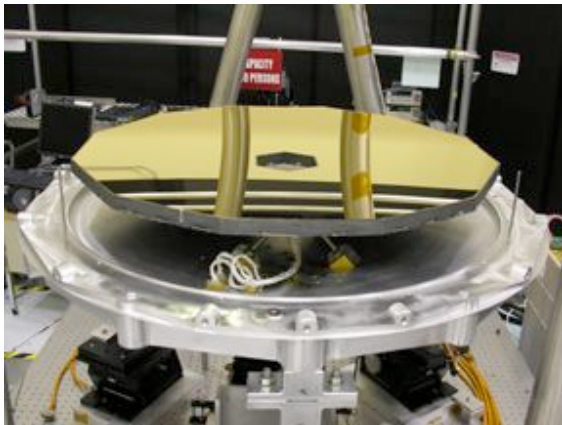
A detailed design study of the *ATLAST-9.2m* concept was performed at the NASA GSFC Integrated Design Center during February and March of 2009. **The key conclusions were summarized earlier but the full details can be found in a separate volume that is available at <http://www.stsci.edu/institute/atlast>** (click on “*ATLAST* Mission Concept Study”).

## Appendix H: Actuated Hybrid Mirrors

Future large optics programs will require a new paradigm for the manufacture of large aperture space telescopes. The technology development of meter class Actuated Hybrid Mirrors (AHM's) specifically addressed the problem as how to provide tens of square meters of optical quality, lightweight space qualifiable optics at reduced cost and time to manufacture. The AHM, shown in Figure H-1, is the result of combing three distinct technologies:

1. A metallic nanolaminate facesheet that provides a high optic quality reflective surface.
2. A Silicon Carbide (SiC) facesheet that provides structural support and houses actuators to provide an adaptive surface figure.
3. A Wavefront sensing system that the provides active figure control.

AHM's are a breakthrough technology demonstration in lightweight, highly actuated primary mirrors for space applications. The AHM replaces passive mass with actuators and controls, while maintaining a high level of optical performance. These AHM mirrors will reduce manufacturing cycle time from years to months. They provide low-scatter, diffraction-limited imaging in the space environment. They will reduce the mass areal density of large mirrors to 12-15 kg/m<sup>2</sup>.



PMN Actuator



Rear Surface Actuation

**Figure H-1.** 75 cm Actuated Hybrid Mirror and associated actuator hardware.

JPL, in conjunction with Lawrence Livermore national Laboratory and Xinetics Inc. (now NGST Xinetics) have been developing AHM over the last several years. Nanolaminate materials are multi-layer metallic foils grown by sputter deposition with atomic-scale control made off of a master convex mandrel. Current material systems have tailorable low thermal expansion and low residual thermal stress to match the SiC substrates thermal expansion. Fabrication time is independent of diameter, typically 3 to 4 days dependent on thickness. Other advantages of nanolaminates are that large surface area nanolaminate foils have been replicated more than 15 times from one high quality figured mandrel tooling without degrading the mandrel quality. On a small scale reflecting surfaces of nanolaminate foils have been demonstrated to replicate the

surface quality of the mandrel tooling with a surface roughness better than 12 Å to 20 Å. This capability can be extended down to the 10-20 nm surface roughness mandrel by investing time in polishing the master mandrels. The flight reflective coating is integrated into the nanolaminate processing. There is no post-reflective coating process. Gold has been demonstrated, and other materials could be used as well.

The SiC substrate provides high stiffness-to-weight structure with excellent thermal stability. Near net shape forming using re-usable replication molds enables the SiC mirror substrates to be made in a few weeks to finished dimensions. Actuators are embedded in the substrate ribs in a manner that eliminates external forces and moments, thus obviating the need for a separate reaction structure. Fabricated from lead-magnesium-niobate (PMN) nanopowders, the low power ceramic actuators enable large mirror deflections with Angstrom level resolution. The PMN actuators are electrostrictive actuators, not piezo-ceramic. Once power is applied, the actuators will change shape and power can be removed from the actuator and the actuator will maintain nanometer dimensional stability. This results in a low power, minimal complexity control electronics. Robotic bonding of AHMs that ensure high quality, reproducible bonding processes are scalable to 2-meter class optics.

AHM Mirrors use Surface Parallel Actuation (SPA) to provide precision mirror shape control without the need for a separate reaction mass. The SPA is capable of correcting the primary mirror for low order and mid spatial frequency errors.

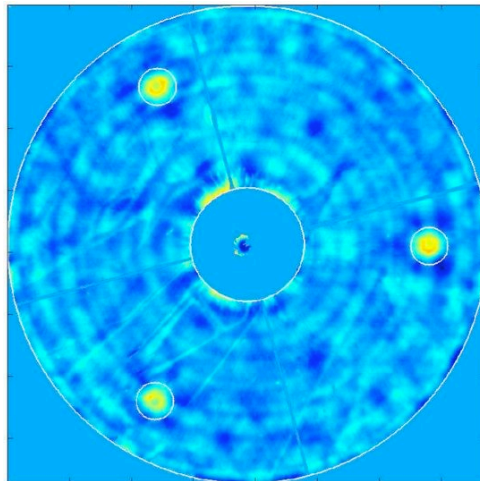


*Figure H-2.* Interferogram of a 75 cm AHM in a Cassegrain telescope configuration.

### **Performance of Actuated Hybrid Mirrors:**

Two 75 cm AHM have been fabricated and optically tested both in air and in vacuum. Figure H-2 shows an interferogram of the mirrors shown in Figure H-1 as part of an Cassegrain telescope configuration. The initial mandrel surface error was 2 microns, with the error mostly being coma and astigmatism. This mirror was tested post-thermal cycling in a vacuum chamber and the figure is driven to a hyperbolic shape for test. The surface figure error is 26.4 nm within 72 cm clear aperture, excluding gravity sag around mounts. Figure H-3 shows the deviates from 50 Volts required for each of 414 actuators. The mean actuator command is 10.3 V from 50 V and

## Advanced Technology Large-Aperture Space Telescope (ATLAST)

the standard deviation is 11.1 V. For these two mirrors, the corrected surface figure error is consistent from the first to the most recent measurements. The streaks observed in the interferogram are due polishing scratches in the master mandrel. With a higher quality master mandrel, a surface figure of 10 nm is achievable for meter class optics. This optic has also been shown to survive a 15 Grms random vibration test and was able to recreate the same optical performance.

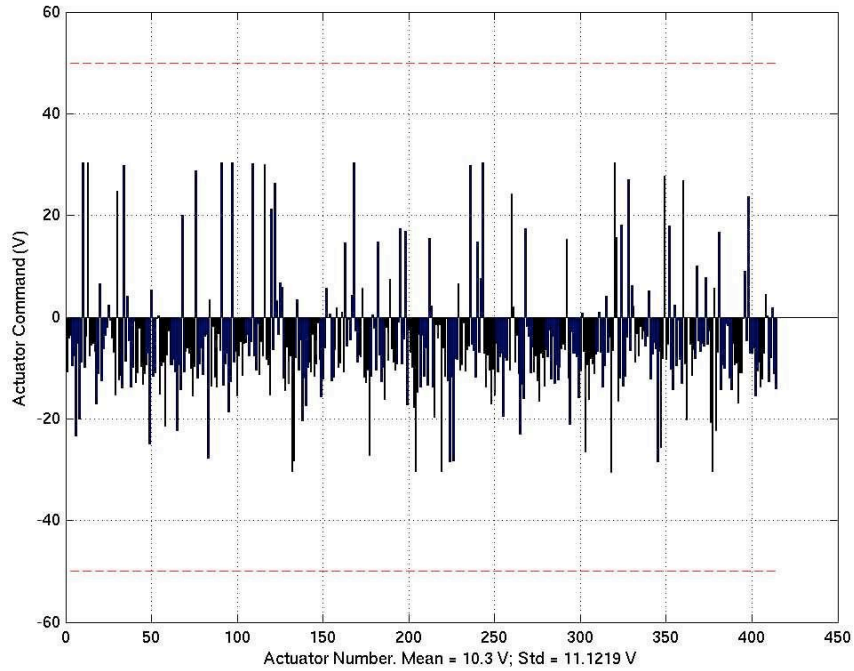


**Figure H-3.** Actuator deviate voltage performance of a 75 cm AHM in a Cassegrain telescope configuration.

## **Appendix I: *ATLAST* Gigapixel Camera: Focal Plane Packaging and Electronics**

Below an *ATLAST* focal plane package and focal plane electronics design unfolds based on basic mosaic operation, configuration, power and mass assumptions. This exercise is important because it demonstrates that the *ATLAST* Gigapixel focal plane array (FPA) packaging and electronics are well within reach of current technology, once a sensor is available.

The greatest design drivers for this focal plane package are the need to minimize the gaps between detector active areas and the thermal and temperature issues related to cryogenic operating temperatures. To minimize the gaps, each component of the focal plane module is configured so that it is no larger than necessary, relative to the active area. For example, the margins around the active area on the detector chip are small. The ceramic printed wiring board (PWB) under the device is larger by just enough to accommodate pads for wire-bonding. The electrical, structural and thermal interfaces for each module lie within the boundary defined by this PWB.

The FPA must use low thermal expansion materials to be compatible with the expansion coefficient of the silicon device as well as to maintain geometric stability. The materials must also be good thermal conductors to achieve the operating temperature and to dissipate the heat generated during operation. There are few material choices that satisfy both requirements, but likely choices would be molybdenum for the metal parts and aluminum nitride for the dielectrics.

The focal plane modules are identical and are highly modular in the FPA mosaic. Each is attached to the baseplate with screws from the back side. Masks to mitigate illumination of device edges and shiny surfaces near the device are also attached from the back. The connectors on each module protrude through the baseplate and are then available for connection to cables to the nearby electronics box without additional interconnects.

The detector and the baseplate are cooled to the operating temperature by the use of a redundant heatpipe pair. Flexible thermal straps help to reduce the temperature gradients across the baseplate. It is assumed that there would be a thermal connection outside of the FPA to a passive radiator sufficiently cold to achieve the FPA operating temperature.

Alignment of the detectors within the FPA would be accomplished at two points in the manufacture of the FPA. First the detector chip would be located carefully when adhesively bonded to the ceramic PWB. Secondly when the module is placed on the baseplate another alignment would be done.

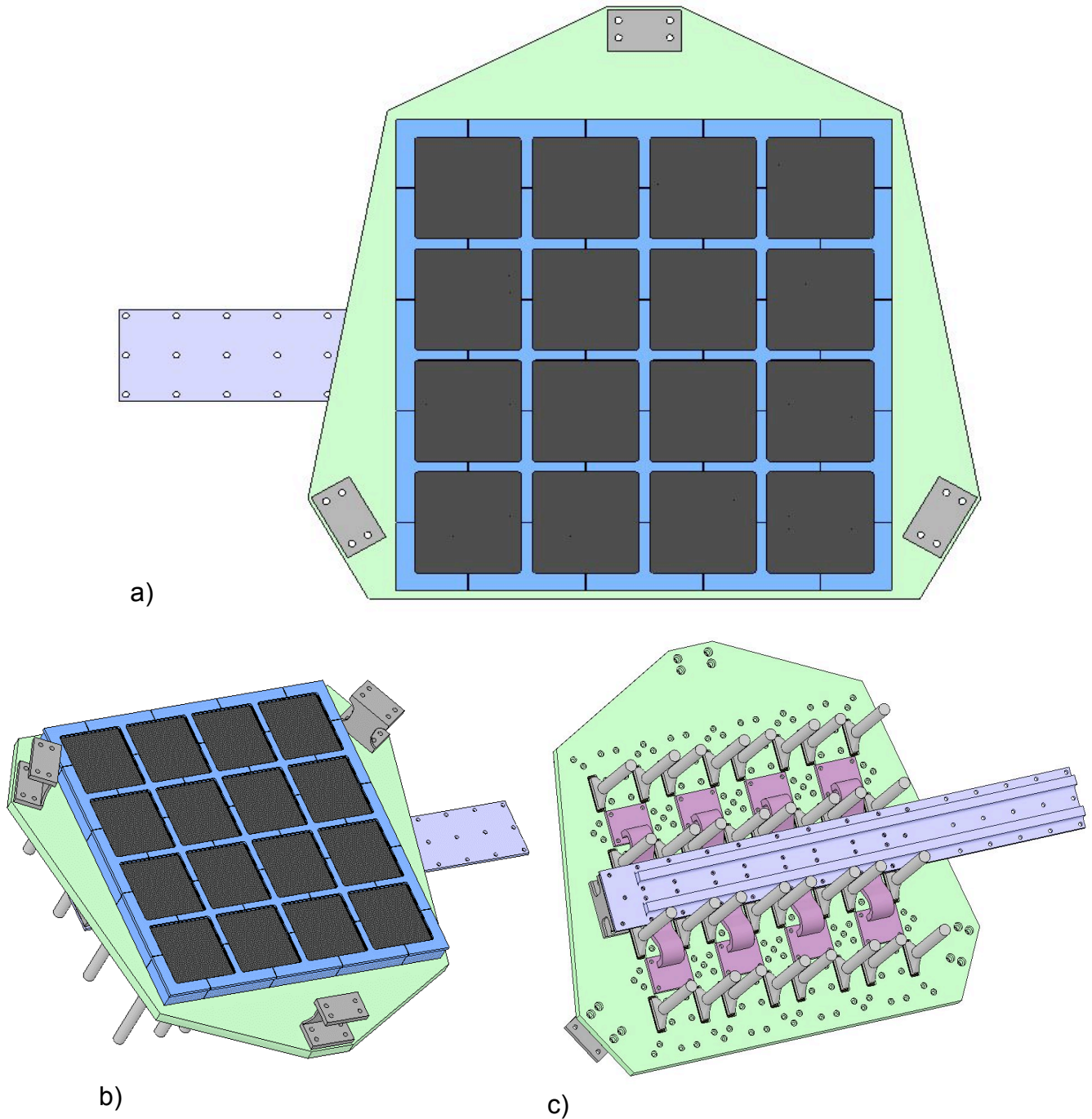


**Figure I-1.** A 32 K x 32 K mosaic focal plane array concept with 16 modules. Each module is 8 K x 8 K in this design (a) top view (b) top view, oblique angle showing three mounting fixtures (c) bottom view showing electrical connections and thermal system. 11/6/2008, E. Freymiller.

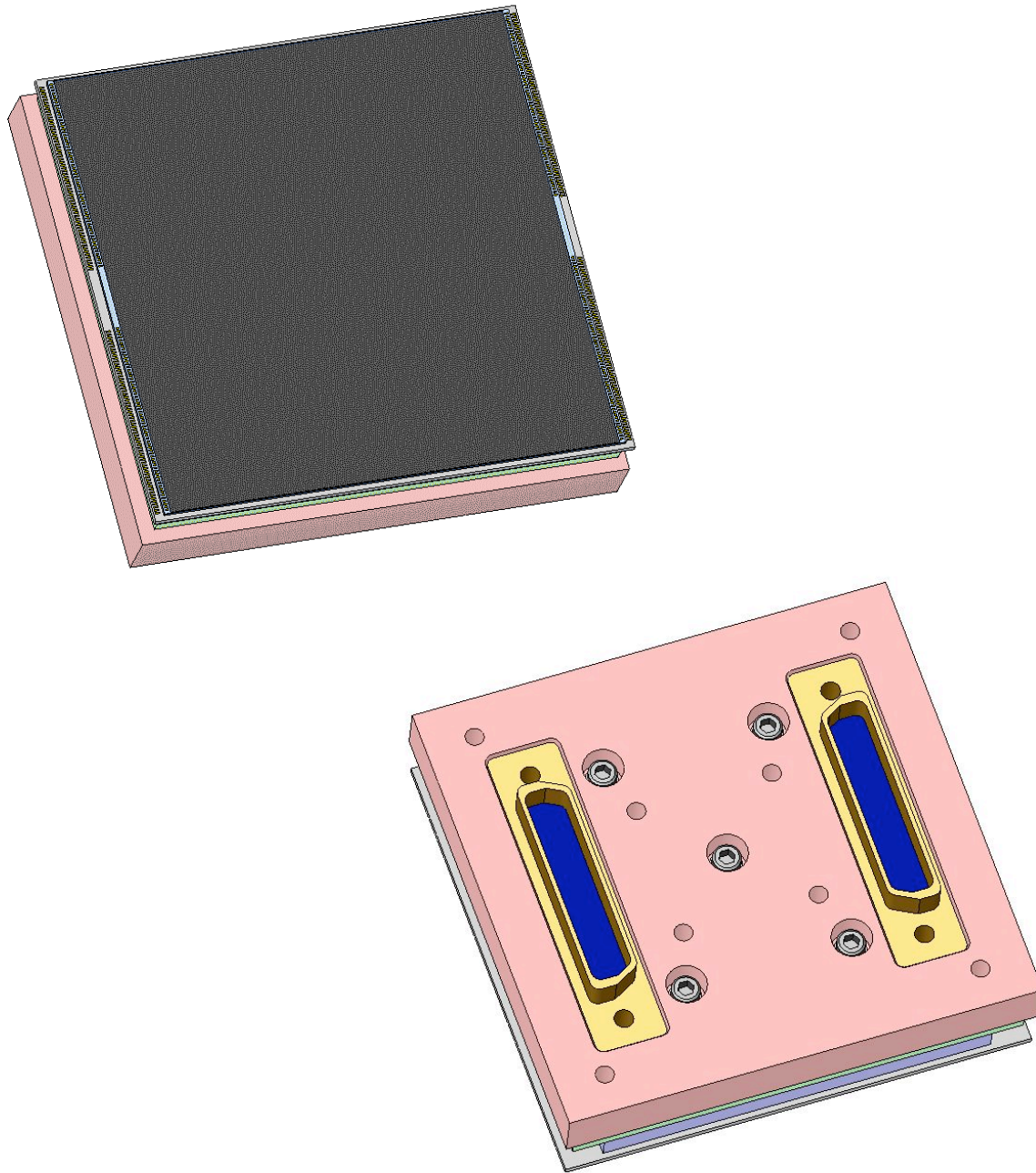


**Figure I-2.** Module front and back sides. The front view shows the detector and the back view show the detector-to-module mounting screws and feed-through electrical D-connectors. 11/6/2008, E. Freymiller

## Advanced Technology Large-Aperture Space Telescope (ATLAST)

The focal plane electronics (FPE) required to operate the 32K x 32K *ATLAST* pixel array assumes that the array was assembled from a 4 x 4 array of 8K x 8K L3CCD die, each chip has 16 outputs with all outputs being readout simultaneously, and the chips are readout sequentially at 1 MHz data rate for a readout time of approximately 4 seconds per chip. By reading the chips separately it is possible to process all the data through a common set of electronics, simplifying the post processing of the data, as was done for the Kepler focal plane array [47].

Assuming CCD mosaic operation common to existing focal plane arrays, this concept will allow a design which can meet an anticipated focal plane system mass requirement of less than 100 kg, including the focal plane array. The weight of the FPE is estimated to be on the order of 45 kg. The focal plane electronics can be designed to operate at approximately 200 Watts.

The design values are based on experience with the *Kepler* focal plane array [47]:

- The *Kepler* Science Module Driver circuit quiescent power is 1.7 Watts. This includes first stage preamps, bias generators & clock drivers in quiescent power condition.
- For each *Kepler* Science Module Driver, circuit power dissipated during the 0.5 second readout period is an additional 3.5 Watts.
- The *Kepler* FPA mass is 22 kg, based on CDR maturity.

The design concept summarized here is presented to demonstrate that a focal plane array package and focal plane electronics are achievable with current technology.

## Appendix J: Summary of Visible Light Detector Technologies for *ATLAST*

This appendix summarizes the detector technology options for the sensors for the wide-field imaging instrument on the *ATLAST* Telescope. A preliminary design for the focal plane calls for a 32K x 32K, photon-counting detector with 9-10  $\mu\text{m}$  pixels. The intended spectral range of the focal plane is 300 nm to 1000 nm. It is likely the device will need to be thinned. There are at least four possible technologies that could be employed to fabricate this sensor: a conventional Charge-coupled Device (CCD), the L3CCD™ devices offered by e2v Technologies, the "Impactron" device designed by Texas Instruments, or a monolithic or a hybrid-Complementary Metal Oxide Semiconductor (CMOS) imager. The technology associated with the L3CCD and the Impactron processes are available today. Here we review all four candidate technologies and discuss how each could be matured to produce an operational focal plane for *ATLAST* in the next decade.

**Table J-1: Requirements for ATLAST Focal Plane Array for a 2020+ mission**

Instrument	Imaging Focal Plane Array 300 nm – 1000 nm
Detector	32K x 32K pixels, 9 $\mu\text{m}$ square pixels High Quantum Efficiency >70% Negligible Read Noise, Low Dark Current Minimize gap between chips Radiation Hardened for operation at SE-L2 5 years minimum lifetime with a goal of 10 years
Operation	1000 second integrations typical ~100 frames per day Optics will dither to eliminate defects Shutter needed for CCD implementation
Design	Designed with modularity for simple integration and test Designed with serviceability in mind

### Requirements of the ATLAST Focal Plane Array

Let us first address the size of the focal plane and consider its requirements and characteristics. Some of these are listed in Table J-1. The current state-of-the-art in CCD technology is the 10,560 x 10,560 STA1600A made by Semiconductor Technology Associates of San Juan Capistrano, CA (see Figure J-1) [66]. This device has 9  $\mu\text{m}$  pixels. This device is optimized for the visible spectrum. Although the device is intended to be operated as a split device with 8 outputs on top and 8 outputs on the bottom, it can be read out as a single chip through either the top or the bottom bank of amplifiers. The well capacity is 80,000 electrons and the horizontal and vertical Charge Transfer Efficiency (CTE) is > 0.999998. As may be seen in the figure, the device occupies an entire 150 mm wafer. Devices have been successfully thinned by Mike Lesser of the Univ. of Arizona Imaging Technology Lab. A thinned device is now

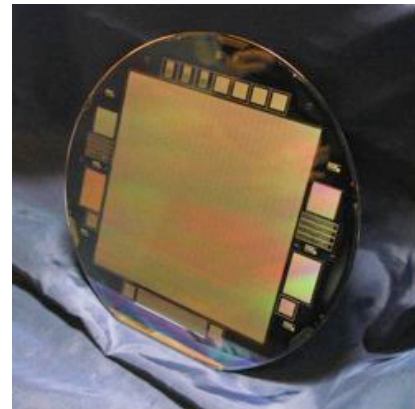


**Figure J-1.** A 10.6K x 10.6K CCD from STA.

in use at the USNO in Flagstaff. AR coatings exist that can provide a very high quantum efficiency across the spectral band of interest.

### Detector Architectures

Although a 10Kx10K device has been made, clearly a 32K x32K device is not in the cards - today. To build a monolithic 32K x 32K device would require a wafer  $\sqrt{2} \times 9 \times 32 \text{ mm} = \sim 450 \text{ mm}$  wafer. Although such a wafer size is on the Silicon roadmap, it will be a while before these wafers and the requisite processing equipment become available [81]. Consequently, the array will need to be assembled from smaller chips. These chips could be either 8K x 8K or 4Kx 4K devices. This would imply that the completed focal plane would be a 4 x 4 or an 8 x 8 array mosaic of these chips. Such mosaics are being assembled today [see Figure J-2]. The devices would need to be thinned to achieve the highest quantum efficiency. A pixel size of 9  $\mu\text{m}$  is assumed. Low dark current and minimum noises are features that are desired. Minimum sized gaps would be desired, although it is anticipated that a step and stare program would be employed to remove defects. Integration times of 1,000 second per exposure would be typical.

For the present, let us assume an 8K x 8K device as the basic building block. It remains now to examine possible architectures for the 8K x 8K devices. The first possibility is a monolithic device with a single output. This is the simplest scheme and would require the least in the way of electronics. It would however require an inordinate amount of time to readout the array: 640 second at 1 Mpixel/second.

The second option, illustrated in Figure J-3, would be to construct the device such that it was segmented into four 4K x 4K subarrays, or eight 2K x 4K sections or 16 1K x 4K subarrays (Figure J-3, right). Each section has its own serial register (along the short dimension) and its own amplifier.

This provides a much more rapid readout and the expense of additional electronics. But it does have the advantage that if one segment goes bad, it need not affect the other segments.

The last option we consider is one where the 8K x 8K is itself segmented into an 8 x 8 array of 1K x 1K CCDs. (See Figure J-4) In this case, each 1K x 1K subarray is connected to and driven by a common set of clocks through a small block of logic circuits associated with each subarray. In addition, each 1K x 1K array has its own output amplifier and each column has a single output amplifier. The amplifier of a single 1K x 1K is connected to the column amplifier. Thus, on a single chip to read it out, the top eight 1K x 1Ks would be connected and readout while the remaining 56 devices are idle. Then the second row of arrays would be addressed and readout, followed by the third, etc.



*Figure J-2.* The Kepler Focal Plane is curved with 42 1K x 1K CCDs.

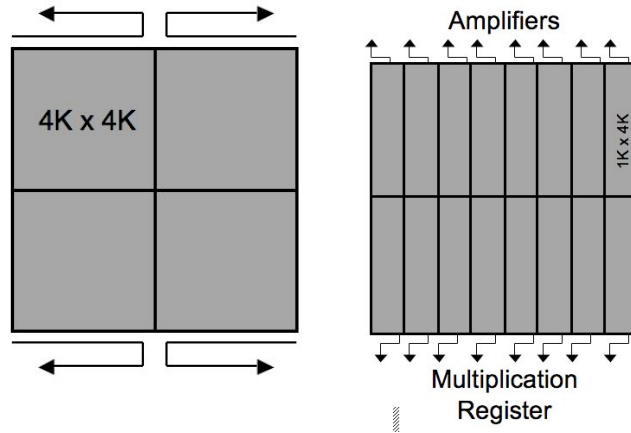


**Figure J-3.** **LEFT:** A typical configuration for a 8K x 8K device. The device has been segmented into four, 4Kx4K quadrants, each with its own serial register. **RIGHT:** Schematic layout of an 8K x 8K CCD segmented into 16 1K x 4K subarrays.

This latter approach is being successfully implemented on the Pan-STARRS Gigapixel arrays. In this case the array is ~5K x 5K and the subarrays are each ~600 x 600 pixels.

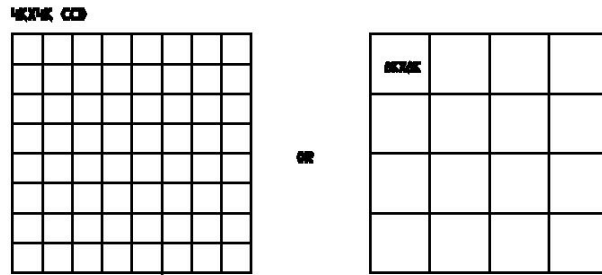


**Figure J-4.** An alternative configuration would be to segment the device into an array of smaller devices, for example, 64 1K x 1K or 16 2K x 2K subarrays each of which can be independently readout.

### Conventional CCDs

The first approach is to consider a conventional CCD. As indicated above 10Kx10K CCDs already exist. So fabricating 8Kx 8K arrays should be doable task now. Such a device could have 8 output amplifiers at the top and 8 output amplifiers at the bottom of the chip. Each amplifier would address a 4K x 1K section of the device (see Figure J-3).

### CCD Pixel Size

The device will be made with three levels of polysilicon gates. The pixels will be 9  $\mu\text{m}$  square and use three phase clocking technology. The use of three levels of poly leads to the highest yields for these very large devices. Although a photolithographic defect on one layer can produce a defective pixel or column, it only shorts electrically two gates that are the same electrical phase. This is not a fatal defect for the device.

**CCD Noise**

Assuming a readout rate of 100 kpixel/second, one can expect the read noise to be 1-3 electrons, rms. Such devices are routinely available today. [79]

**CCD Dark Current**

By employing Multi-pinned Phase (MPP) technology to clock the device, the dark current will be dominated by the generation of carriers within the depletion region. In MPP clocking, one of the phases (usually phase 3) receives an additional p-type implant, altering the channel potential beneath that gate. Then when the parallel clocks are driven into inversion (collecting a number of holes at the surface), there is still a potential well in which to collect the signal charges for that pixel. The holes at the surface; prevent electrons generated by the surface states from being collected as dark current.

Figure J-5 presents calculations of the dark current for a 9 μm pixel as a function of operating temperature. The parameter is the dark current in pA/cm<sup>2</sup> at 300K. It is not unreasonable to expect dark currents in the 10-30 pA/cm<sup>2</sup> range at 300K. At -100C, this translates to a dark current of ~10<sup>-5</sup> electrons/pixel/second. [79]

**CCD Charge Transfer Efficiency (CTE)**

The charge transfer efficiency in today’s devices is in the range of 0.99999 or higher. In a space environment such as seen by Hubble, the CTE degrades at a rate of approximately 0.000016/year. [67] Assume that at the beginning of life the CTE in the horizontal and vertical directions is 0.999998. Table 2 presents the normalized signal size of the most remote pixel after transferring through the device to the nearest output amplifier.

Using the expression for the charge transfer loss, the loss in the signal can be estimated.

$$Signal = S_o * (CTE_H)^{H_{pixels}} * (CTE_V)^{V_{pixels}}$$

where  $S_o$  is the initial signal amplitude.

**Table J-2: CTE estimates for different sized devices and for selected times using the expected degradation for a Hubble like orbit.**

	CTE	1Kx1K	2Kx2K	4Kx1K
BOL	0.999998	0.99591	0.99184	0.98981
1 year	0.999998	0.95967	0.92135	0.90267
5 years	0.999992	0.84887	0.72058	0.66390

For example, the charge retained in a packet that traverses 2K vertical pixels followed by 2K horizontal pixels is 95.97 % of the original packet or a 4% loss after 1 year in such an orbit. There is evidence from the SOHO CCDs that the degradation in CTE is not as severe at the Lagrangian point L1 as in the Hubble orbit. [68].

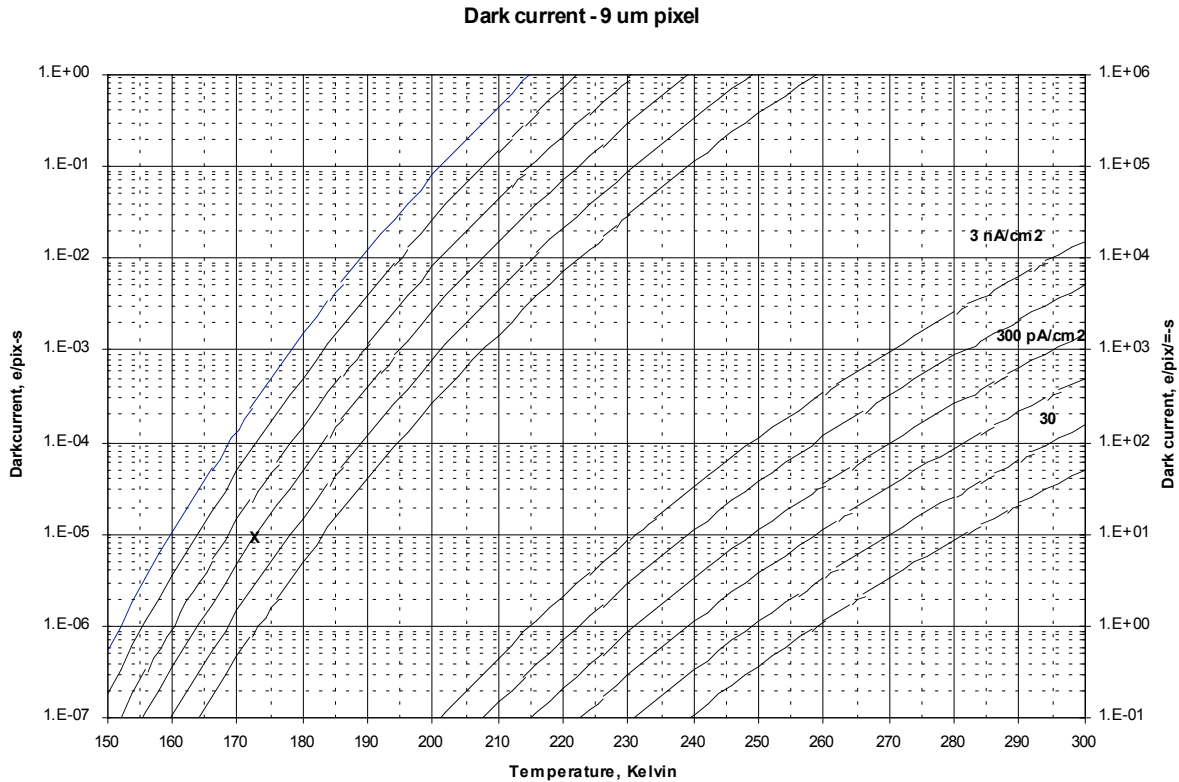


**Figure J-5.** Dark current as a function of temperature for a CCD or CMOS device when the dark current is dominate by generation-recombination current in the depletion region. Dark current equations are found in Reference [79].

### ***CCD Well Capacity***

The well capacity can be expected to be 80,000 electrons for a 9  $\mu\text{m}$  pixel. [79]

### ***CCD Amplifier Gain***

The amplifier gain can reasonably be expected to be 4-8  $\mu\text{V}/\text{e}^-$ . With 16 amplifiers, it would be desirable to have them reasonably matched. With today's processing capabilities, it is possible to expect matching of the gains to within 2-3% within the chip and +5% chip-to-chip within the focal plane. [79]

### ***CCD Mini-channel***

A mini-channel will be employed to help alleviate CTE problems with small charge packets by confining these packets to a smaller volume of Silicon, as it passes down the channel on its way to the output. The mini-channel should be capable of holding greater than 4,000 electrons. [79]

### ***CCD Quantum Efficiency***

In order to achieve high quantum efficiency, the device will need to be thinned. Figure J-9 presents a typical QE curve for a thinned n-channel CCD built on standard p/p+ epitaxial material (the conventional CCD). As shown in the figure, the QE can be quite high, approaching 90-95% at the peak. However the long wavelength response is not as high as it might be. The other two curves in the figure show improved performance in the red. These will be discussed later. Nowever note that with the proper AR coating, it is possible to achieve high quantum efficiency in both the near IR and in the blue portion of the spectrum. [79]

### ***CCD Radiation Effects and Susceptibility***

The CCD is sensitive to radiation effects. In particular, ionizing radiation will give rise to threshold voltage shifts which can lead to dark current increases, well capacity losses, and CTE effects. In addition, proton and other particles can create traps in the channel and depletion region of a pixel, particularly the combination of a Phosphorus atom and a lattice vacancy, the P-V center, leading to degradation in the CTE and an increase in the number of dark current spikes. [79]

Thermal annealing of the device has shown that, to an extent, the effects of the particle radiation can be mitigated, i.e., the dark current spikes can be reduced [67].

### ***CCD Yield***

The size of an 8K x 8K device will be approximately  $\sqrt{2 \times 9 \times 8192} = 104.2$  mm in diagonal. This means that only one device will fit on a 150 mm wafer. Because we are using three phase three levels of poly technology, we should expect to obtain perhaps a 30% yield through thinning and into test. The defect criteria will then determine the final yield. [79]

### ***CCD Power Estimates***

Typical power estimates for conventional CCDs can be of the order of 0.1 W for the integration and 0.2 W for the read out periods. [79]

## **e2v L3CCD™**

The principle of operation of the electron multiplying CCDs is illustrated in Figure J-6a [69]. The layout of a typical frame transfer device is shown in Figure J-6b. In the case of the e2v L3CCD™, it requires four gates in the multiplying register to effect the gain. In this register, one gate is held at a dc voltage while the other three gates are clocked in the normal three phase manner. The dc-biased gate blocks the transfer of charge from a collecting well into its neighbor while the neighboring gate is being biased to a high voltage. Blocking the transfer of charge permits the creation of an electric field sufficiently large to provide a small probability that an electron will cause impact ionization, thus providing two electrons where there was one.

Assuming that the probability of producing a second carrier is  $p/\text{pixel}$  and a multiplication register that is  $N$  pixels long, the gain,  $G$ , seen by each electron is

$$G = (1 + p)^N$$

The zero signal noise will be given by the expression:

$$NES = \left( 2N_d + \frac{N_r^2}{G^2} \right)^{1/2}$$

where  $N_d$  is the dark current in electrons and  $N_r$  is the read noise of the output amplifier in electrons. To reduce the read noise to a negligible level, the gain must be large.

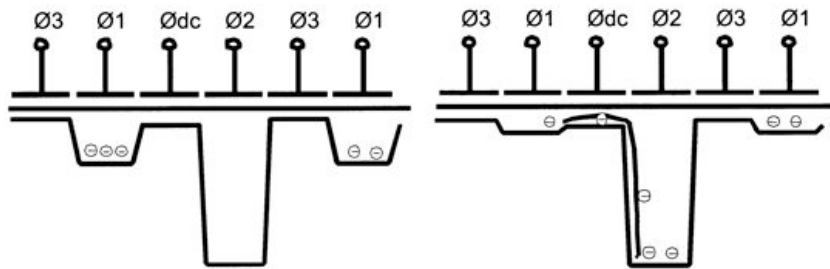


**Figure J-6a.** Principle of operation of the L3CCD [69].

There are two ways to make the gain large: increase  $p$  or increase  $N$ . Figure J-7 illustrates the gain as a function of the positive rail voltage applied to the avalanching well for the e2v CCD65. Note that for large gains, some very large voltages may be required (40-50V). For example, with a probability  $p=0.01$  (a typical value) and 500 pixels in the multiplication register, the gain is 145. To achieve such a high gain, the voltage required to be applied to the avalanche gate is  $\sim 43.4V$  at room temperature. This is in contrast to the normal positive rail of +10 to +15 V. Fortunately as one cools, the voltage required to achieve the same gain decreases. Nevertheless, the voltage is still large.

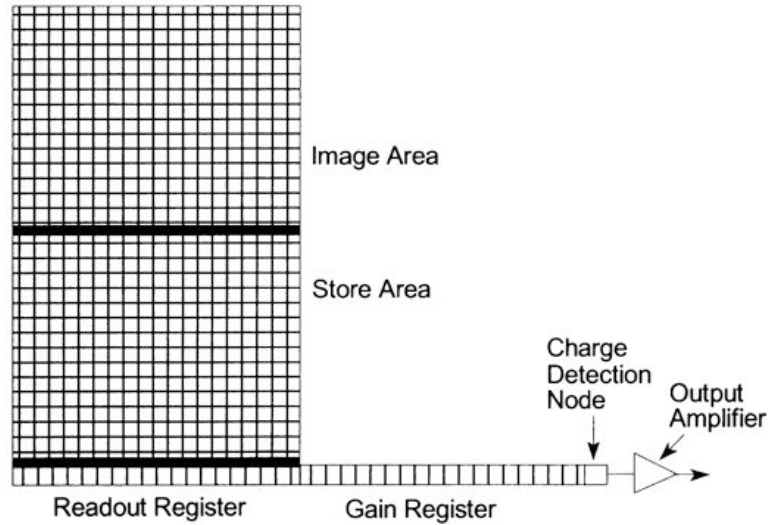


**Figure J-6b.** Typical L3CC layout. The Frame Store character of the device is not a requirement. [69]

We will consider an 8K x 8K device segmented into an array of sixteen 4K x 1K subarrays (See Figure J-3, right).

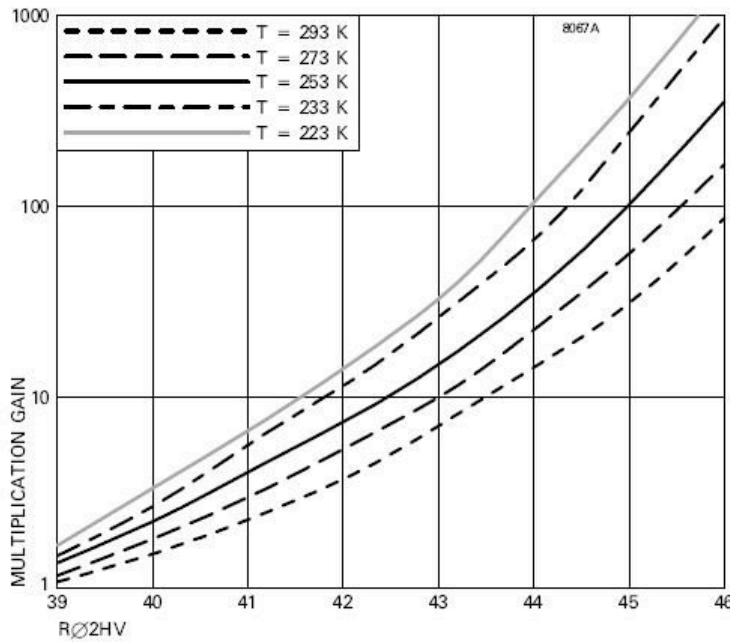


**Figure J-7.** L3CCD gain as a function of the bias applied to the high rail of the receiving well [70].

**L3CCD Pixel Size**

The device will be made with three levels of polysilicon gates. The pixels will be 9 μm square and use three phase clocking technology. The use of three levels of poly leads to the highest yields for these very large devices. Although a photolithographic defect on one layer can

produce a defective pixel or column, it only shorts electrically two gates that are the same electrical phase. This is not a fatal defect for the device.

### ***L3CCD Multiplication Register***

The multiplication register will be approximately 1,000 pixels long. Paralleling the multiplication register will be a second resistor into which excess charge from a given pixel can flow to prevent blooming of the multiplication register by a particularly bright object. The gain does not need to be large as there are 1,000 pixels and the read noise will be small. A gain of 15-20 will probably suffice. However, the high rail on the receiving well will still be large, greater than 38-40 Volts.

It would be a worthwhile project to reduce the required operating voltage.

### ***L3CCD Noise***

The output amplifier will be a low noise, two stage source follower, similar to the amplifier which e2v has used extensively on other devices, e.g., the CCD42-40. Assuming a readout noise of 2-3 electrons rms (typical for e2v devices operating at that readout rate), a gain of around 15 will render the amplifier contribution completely negligible. This will, however, require a high rail of approximately 40 V for the avalanching gate.

### ***L3CCD Dark Current***

The dark current consists of two components: thermally generated charges and clock-induced-charges [71].

The temperature dependence of the thermally induced dark current is given in Figure J-5. This current is due to the generation of charges within the depletion region of the pixels. The dark current of the device operating in the MPP mode is typically  $100 \text{ pA/cm}^2$  at room temperature (300K). For an operating temperature of -100 degrees C, the generation rate is  $1\text{E-}5$  electrons/pixe/second or a dark current of 1 electron/100 pixels for a 1,000 second integration period. Assuming an operating temperature of -120 C, the dark current falls to  $\sim 1\text{E-}7$  electrons/pix-sec.

The clock-induced-charge is, as the name suggests, charge that is generated due to the shape and amplitude of the clock waveforms [71]. It is also known as a spurious charge. Figure J-8 presents curves of clock-induced charge as a function of clock amplitude and illustrates the magnitude of the effect for a typical e2v device. There are two conditions to be considered: MPP and non-MPP modes. Note that the clock-induced-charge is larger if the part is operated in the MPP mode. It is believed that the clock-induced-charge is due to impact ionization by hot holes as they exit the region beneath the gate that is activated. If the clock amplitude is too large or the rise time is too fast, more spurious charge will be generated per pixel. Since the pixels can be read out slowly, there is the opportunity to tailor the clocks and reduce the clock-induced-charge to a minimum.

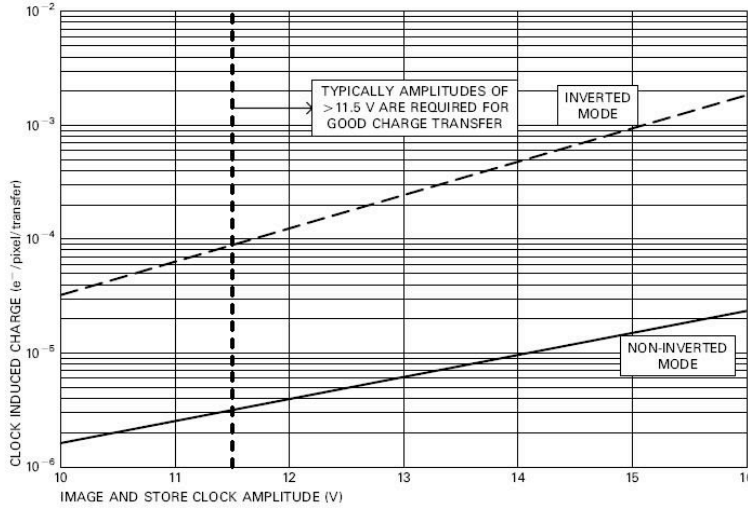


**Figure J-8.** Showing the magnitude of the clock induced charge generated as a function of the parallel clock amplitude [71].

Note that the clock-induced-charge is independent of the integration time. It depends on the transfer of charge packets through the device.

**L3CCD CTE**

The CTE at the beginning of life should be >0.999998 in both the serial and parallel directions. A mini-channel or notch will be included to help with the charge transfer of small charge packets. The capacity of the notch should be approximately 4-8,000 electrons.

Given a typical CTE of 0.999998, the charge retained in the most remote pixel is

$$Signal = S_0(0.999998)^{4096} (0.999998)^{1024} = 0.98981$$

By segmenting the device into an array of subarrays we have improved the overall performance of the FPA.

**L3CCD Well Capacity**

The well capacity of the 9 μm pixel should be ~80,000 electrons. [79]

**L3CCD Quantum Efficiency**

The wavelength range of interest of this device is 300-1000 nm. The desire to image at 1000 nm with high quantum efficiency suggests that a fully depleted CCD or at least a device built on high resistivity substrate should be used. To achieve high QE at 300 nm requires that the device be thinned. Devices of this size and larger have successfully been thinned. The quantum efficiencies that can be obtained with such devices are illustrated in Figure J-9.

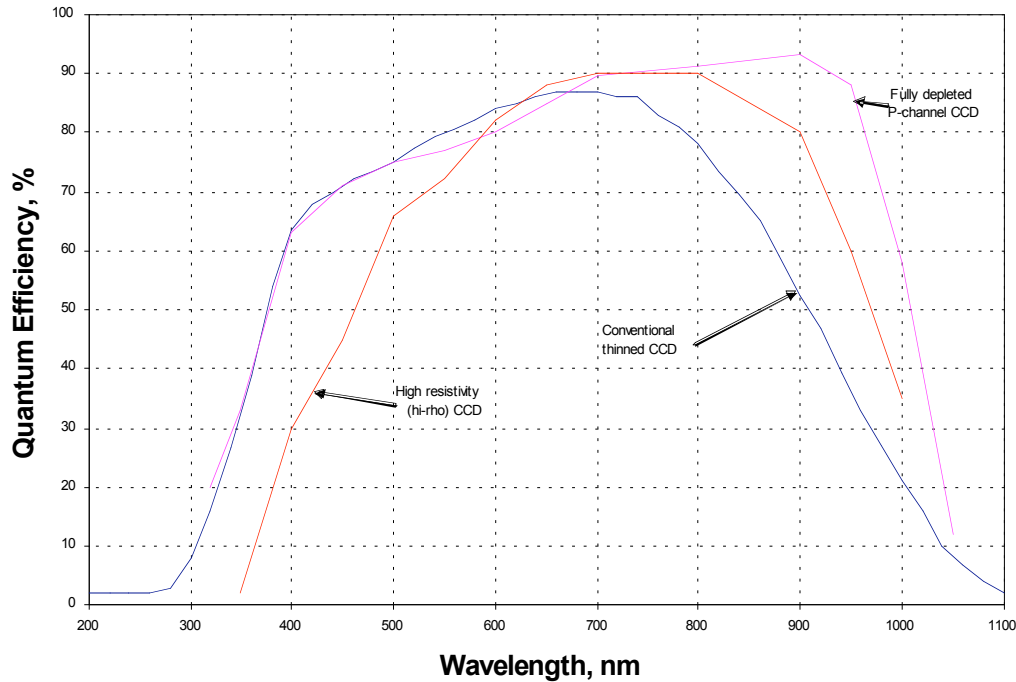


**Figure J-9.** Typical Quantum Efficiency curves for three thinned devices: a conventional CCD, a full depleted, p-channel chip, a device built on high resistivity material. [77,78,79]

### ***L3CCD Amplifier Gain***

Typical gain for the L3CCDs is in the 1-5  $\mu\text{V}/\text{e}^-$  depending on the size signal expected. [69] One should expect a uniformity of 2-3% within a chip and  $\sim 5\%$  uniformity chip-to-chip within a lot.

### ***L3CCD Mini-channel***

A mini-channel will be incorporated in the parallel and serial registers to aide in the transfer of small charge packets. The well capacity of the mini-channel will be  $\sim 4\text{ke} - 8\text{ke}$ . [69]

### ***L3CCD Radiation Effects and Susceptibility***

Because this is a CCD it will be susceptible to a radiation environment. It is susceptible to both ionizing radiation in terms of threshold voltage shifts and to particle damage in the buried channel affecting the CTE. There is evidence, however, that these devices can survive in the environment characteristic of the Lagrangian points for at least 10 years. This is true of the SOHO CCDs which have been operating for  $\sim 15$  years at L1 [68].

### ***L3CCD Yield Issues***

Although it is possible to build an 8K x 8K device, it may be more cost effective to build 4Kx4K devices and create a 8 x 8 mosaic of these devices. Additionally, the four devices may have fewer defects.

### ***L3CCD Aging***

One of the problems that will develop is aging of the CCD due to the large voltage employed to drive the avalanche well [72]. Fortunately, the device will not be operated continuously. Assuming 1000 second integration times and the 41 second readout time, the only time a high voltage should be placed on the avalanche gate is during the readout time. Assuming 1000 second integrations, over a year the device should see about 350 hours of high voltage operation. Fortunately, the gain can be tracked and the voltage adjusted to compensate for any changes in the gain.

### ***L3CCD Power Estimates***

The L3CCD will require approximately double the power of the conventional CCD. [69]

## **“Impactron” from Texas Instruments**

The Impactron is Texas Instruments’ version of the L3CCD™ [73,74]. The device is built using the TI “Virtual Phase” technology in the parallel section and the normal serial register, and two phase clocking in the multiplication register. The advantage of the Virtual Phase (VP) technology is that clocking the CCD requires only a single clock. Each pixel is divided into two sections: a clocked phase and a virtual phase. Within each phase there is a barrier and a well (see Figure J-10a). The doping profiles in the virtual phase are adjusted such that when the clocked phase is turned off, signal charge will flow over the virtual phase barrier into its well and when the clocked phase is turned off the charge will flow over the clocked barrier into the clocked well (see Figure J-10b). The device behaves like a two-phase device except one of the two phases is held at a constant potential.

In the multiplication register, the device operates using the same basic principle as employed with the L3CCD, where the large built in field is allowed to develop before transferring the signal charge into the avalanche well. The largest Impactron made by TI is a 1K x 1K array. It is unknown if TI would be willing to make an 8K x 8K version, or even a 4K x 4K version which could be put into a 8 x 8 mosaic.

### ***Impactron Pixels***

A 9  $\mu\text{m}$  pixel pitch would not create problems for the VP process and technology.

### ***Impactron Resolution Element***

The resolution element would be the same as for the CCD discussed above.

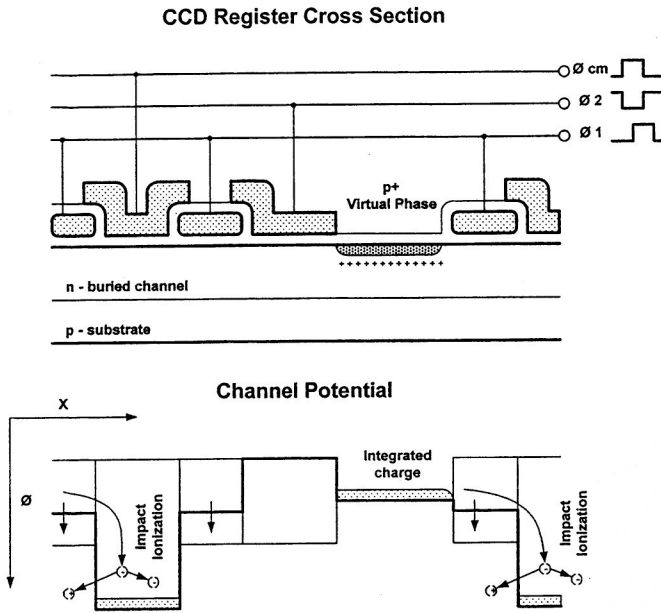


**Figure J-10.** a) Cross section of VP multiplication register illustrating the physical structure. b) Cross section of VP gain register showing the channel potentials during operation [73].

### **Impactron Noise**

The noise factor for the charge multiplication device is given as [74]

$$F^2 = 2 - \frac{1}{M} + \sigma_s^2 N \frac{\left(1 - \frac{1}{M}\right)}{\ln M}$$

where M is the gain/stage,  $\sigma_s$  is the variance of the gain per stage and N is the number of stages. The noise of the device will be given by

$$V_n^2 = V_{na}^2 + M^2 S^2 F^2 N_i$$

where  $V_{na}$  is the amplifier noise, and  $N_i$  is the signal charge. Note for large M the noise factor approaches  $\sqrt{2}$ , the same result that e2v quotes. Again, for large values of the gain the read noise will make a negligible contribution to the total noise.

### **Impactron Dark Current**

The dark current components are similar to the L3CCD™. However, it is not known whether or not the Impactron suffers from the clock-induced noise or spurious charge problem exhibited by the L3CCD.

### **Impactron CTE**

The CTE will be quite high; it will be in the 0.999998 range at BOL.

### ***Impactron Quantum Efficiency***

Even though the Impactron pixel is half uncovered (the ‘virtual phase’ has no poly silicon gate over it, typically it has only oxide and nitride). Still to achieve the highest quantum efficiency, the device will need to be thinned. Any of the standard AR coating may be applied to improve the QE. As with the L3CCD, the device has not been built on thick, high resistivity material, nor has a fully-depleted, p-channel version been fabricated.

### ***Impactron Aging***

Little is known at this time regarding aging of these devices. However, given the lower operating voltages, aging may not be an issue or, if it is an issue, it is likely to be much less of one.

### ***Impactron Radiation Susceptibility***

The radiation sensitivity of the Impactron device will be similar to that of the L3CCD.

### ***Impactron Yield Issues***

Because the TI process involves only a single level of polysilicon in the imaging area the yield can be expected to be quite high, even for an 8Kx8K device.

### ***Impactron Power Requirements***

Since the Impactron utilizes only one level of poly in the parallel section and only two in the serial and gain registers, the power requirements for the chip will be less than either the conventional CCD or the L3CCD.

### ***Impactron Subarray Variation***

As illustrated in Figure J-2, it is possible to divide the 4K x 4K array into a number of subarrays (note that all these subarrays are physically part of one Silicon die). The subarrays could be simple CCDs or they could be similar to L3CCD. In either case, the clock signals required to operate a single subarray would be supplied from the top or the bottom of the column in which the subarray was located. A small logic circuit built into each subarray would control whether or not the clock signals were active in that subarray. The subarrays can thus be independently operated. Arrays of this nature have already been built and are being employed on the Pan STARRS telescopes.

Readout is performed on the individual subarrays when it is deemed time to readout that array. Again, matters are ordered according to columns. At any one time only one array in a column can be readout. This is accomplished by connecting an output amplifier to a column bus, which leads to the output amplifier for that column. In order to do photon counting it is necessary to read out the device fairly rapidly. The reason for this requirement is that the randomness associated with the gain process leads to uncertainty in the number of photons that created a

given signal. Segmenting the array allows one to interrogate the subarrays more rapidly that is possible with the larger devices.

An advantage of this configuration is that those sections that have only faint signals can be integrated for longer periods of time than the average cell while those cells that contain a relatively bright signal can be readout more often thus preventing blooming of the chip, or at least confining it to one segment. A second advantage is that each subarray is separate from all the others. This means that if the segment is bad to begin with, or more importantly, if it were to go degrade significantly during the mission, that subarray can be isolated and ignored while the remainder of the array continues to function normally. Additionally, the effects of CTE degradation will be somewhat mitigated since for the 64 subarray version only 512x512 transfers are required.

### CMOS Arrays

CMOS devices are just now reaching the quality level that they might be considered for some scientific applications. However, achieving the noise levels required by *ATLAST* will require an in pixel gain mechanism that amplifies the signal prior to reading it out, as occurs with the electron multiplying CCDs.

As with the CCD, an 8Kx8K device is feasible. A 8 x 8 mosaic of 4K x 4K chips may be desirable for the reasons given above.

### CMOS Pixels

There are several choices for the pixel architecture [75]. These are referred to as the 3T, 4T, 5T, etc. cell. The number of Field Effect Transistors (FETs) in the cell differentiates them. The 3T cell has 3 FETs: the Reset FET, the Source Follower FET, and the Row Select FET. It is the most basic of the CMOS pixels. The integration site is either a photodiode or a pinned photodiode that is connected directly to the source of the Source Follower. The cells of the image sensor are sampled much like a memory. Each row select transistor connects the pixel to its corresponding column bus structure that ends in a column amplifier. When a given row is selected all pixels in that row connect to the column buses and amplifiers. The amplifiers are sequentially scanned to readout the signal.

A CMOS image sensor for the *ATLAST* application would need to have at least a 3T cell and preferably a 4T or 5T cell. With the basic 3T cell, since the image is stationary, one could readout the device while integrating. The 4T and 5T cells, because of their architecture, in which the output node is separate from the integration node, can be operated in the snap shot mode. In the snap shot mode, the entire image is shifted at once from the integration node to the output node of each pixel. The image is then read out in the normal fashion while integrating the next image. One of the advantages of this method is that one can perform Correlated Double Sampling (CDS) on the data, thus reducing the noise. CDS is not possible with the 3T cell. Another of the advantages of the 4T and 5T cells is that the conversion gain is much higher, because the integration site is separated from the output node. Finally, the extra transistor in the 5T cell can be used to provide connection to an antiblooming sink. [75]

Development effort is need to design gain within the pixel to add a photon counting capability to the device.

### ***CMOS Resolution Element***

The resolution element is again the 3x3 pixel discussed above.

### ***CMOS Noise***

The noise of CMOS detectors has been reduced substantially in the last five years. There are reports of measured noise in the 1-2 electron range, which is competitive with the premium quality CCD noise. Typically, this is achieved by increasing the conversion gain of the on-chip amplifier to the 200-500  $\mu\text{V}/e^-$  range. Since the voltage range of the output amplifier is limited to approximately 1V, such high gains severely limit the well capacity of the pixel. For example with a gain of 500  $\mu\text{V}/e^-$  one could expect a full well of 2,000 electrons. As long as all the signals are low, one can live with such a small well capacity. [75]

### ***CMOS Multiplication Register***

The nature of the device is to address each pixel separately and independently. There will not be a multiplication register. Each pixel will require its own separate multiplication site. As noted above, this is an issue that needs development.

### ***CMOS Dark Current***

The dark current of present day devices can be quite low, comparable with the dark current measured on conventional CCD. Typically, this dark current is due to the generation-recombination in the depletion region of the pixel and near the channel stops. [75]

### ***CMOS Quantum Efficiency***

Assuming that the device would be thinned in order to achieve the highest quantum efficiency, the same AR coating that could be used with the CCDs, would also work with the CMOS device. The result would be a QE comparable to that achievable by the conventional thinned CCD. However, the QE is unlikely to ever be as high as that associated with the fully depleted, p-channel devices. [75]

### ***CMOS Aging***

Little is known regarding the aging of these devices.

### ***CMOS Radiation Susceptibility***

CMOS devices are inherently less susceptible to a radiation environment. They can be made to survive approximately 1 Mrad(Si) of ionizing radiation and minimum changes in the dark current with increasing dose ( $1e11$  p/cm<sup>2</sup>) of proton radiation [76].

### ***CMOS Yield***

Yield should be expected to be relatively high, even for the large devices. [79]

### ***CMOS Power Estimates***

The total power requirements of a CMOS sensor are significantly less than those of a CCD, although more may be dissipated on-chip with a CMOS detector simply because there can be significantly more circuitry on-chip. A typical CMOS array consumes an average power of 200-500 mW, including the horizontal and vertical scanners, the CDS circuit, and the A/D converter(s). Due to power and radiation susceptibility issues and the anticipated increase in availability of CMOS devices, it is likely that CMOS devices will become the future detector of choice. [75]

## **P-channel, Fully-depleted CCDs**

P-channel, full-depleted CCDs have been developed by Lawrence Berkeley National Laboratory (LBNL) [77]. They were developed for the SNAP program which needed very high QE in the NIR region. Instead of an n-type dopant (phosphorous) being implanted into a p-type wafer, a p-type dopant (boron, typically) is implanted into a high resistivity n-type wafer to form the channel of these CCDs. Thus, instead of electrons being collected and transported, it is holes that make up the signal charge.

The high resistivity substrate (5-10 kOhm-cm) implies that the depletion regions below the gates will be quite large. Indeed, the devices are thinned to 200 - 300 microns and a transparent, n-type contact is put on the back surface and biased such that the complete 200 - 300 microns of silicon is fully depleted. The effect is to make the full wafer thickness available to collect hole generated by the incident photons. The effect is particularly dramatic in the red region of the spectrum where quantum efficiencies of greater than 55% at 1,000 nm have been reported.

### ***P-channel CCD Pixel Size***

The device will be made with three levels of polysilicon gates. The pixels will be 9  $\mu$ m square and use three phase clocking technology.

### ***P-channel CCD Noise***

Assuming a readout rate of 100 kpixels/second, one can expect the read noise to be 2-3 electrons. Such devices are available today. [77]

### ***P-channel CCD Multiplication Register***

As currently developed by LBNL, the p-channel devices do not have a gain register.

### ***P-channel CCD Dark Current***

Because of the large depletion region the generation-recombination current can be expected to be significant. As a consequence, the device needs to be operated a lower temperature than other devices considered. Dark currents as low as a few electrons per hour have been reported for devices operating at approximately -130K. [77]

In addition to the generation-recombination current, there will be dark current generated in the surface states. This can be mitigated by operating the device in the MPP or inverted mode. Although with the substrate fully depleted, a connection to the channel stops will likely be needed to provide a ready source of electrons. In the MPP mode, the integration is done with the surface inverted which shields the underlying channel from the surface states and the generation that occurs in these states. During readout, the electrodes momentarily come out of inversion to transfer the charge and then revert to the inverted state. [79]

### ***P-channel CCD CTE***

This is one area in which the p-channel CCD is more effective. As noted above for the n-channel devices, damage caused by energetic particles can disrupt the lattice in the channel and lead to traps. The most effective such trap is the P-V center. Because the channel is formed with a boron implant instead of phosphorous, the p-channel devices are 5 to 10 times harder in a radiation environment than are their n-channel brethren. [77]

As with the n-channel devices, the charge transfer efficiency in today's chips is in the range of 0.99999 or higher. [77]

### ***P-channel CCD Well Capacity***

The well capacity can be expected to be 80,000 electrons for a 9  $\mu\text{m}$  pixel. [79]

### ***P-channel CCD Amplifier Gain***

The amplifier gain can reasonably be expected to be 4-8  $\mu\text{V}/\text{e}^-$ . With 4 amplifiers, it is desired to have them reasonably matched. With today's processing capabilities, it is possible to expect matching of the gains to within  $\pm 2-3\%$  within the chip. [79]

### ***P-channel CCD Mini-channel***

In a radiation environment, protons, neutrons, and heavy ions produce damage to the lattice of the silicon. In particular, these particles displace Silicon atoms from their accustomed place in the lattice producing a vacancy. Some of these vacancies attach themselves to a P atom in the channel region producing a so called P-V center. The P-V center has an energy level in the

forbidden gap of Silicon and acts like a trap. The trap removes charge from the packet in which it was present and releases it into a trailing pixel, thus causing a CTE issue.

A mini-channel will be employed to help alleviate CTE problems with small charge packets by confining these packets to a smaller volume of silicon than the entire channel, as it passes down the channel on its way to the output. The mini-channel should be capable of holding greater than 4,000 electrons. [79]

### ***P-channel CCD Quantum Efficiency***

In order to achieve high quantum efficiency, the device will need to be thinned. Figure J-9 gives a typical QE curve for a thinned, n-channel CCD built on standard p/p+ material. As shown in the figure, the QE can be quite high, approaching 90-95% at the peak. However, the long wavelength response is not as high as desired. [77]

One method of improving the quantum efficiency at long wavelengths is to build the device on thicker, high resistivity material. The thicker material provides more material in which the long wavelength photons can be absorbed and contribute signal instead of passing through the silicon. The LBNL devices have traditionally been built on 5 - 10 kOhm-cm material and thinned to 200 - 300  $\mu\text{m}$ . An n-type contact is applied to the back surface and a bias of 50-100 V is applied causing the entire 200 - 300  $\mu\text{m}$  thick region to be completely depleted. An example of such a device is provided in Figure J-9. Note that the QE at 1,000 nm is in excess of 50%. [77]

### ***P-channel CCD Radiation Effects and Susceptibility***

The CCD is sensitive to radiation effects. In particular, ionizing radiation will give rise to threshold voltage shifts that can lead to dark current increases, well capacity losses, and CTE effects. In addition, as discussed above, proton and other particles can create traps in the channel and depletion region of a pixel leading to degradation in the CTE and to dark current spikes. However, because the device is built with a p-channel, the CTE effects can be somewhat mitigated. [77]. Because the device is so thick (200-300  $\mu\text{m}$ ), it will be a very efficient collector of cosmic ray events. This could be a significant problem for long integrations. [79] Thermal annealing of the device has shown that, to an extent, the effects of the particle radiation on the dark current can be mitigated, i.e., the dark current spikes can be reduced. [80]

### ***P-channel CCD Yield***

Functioning 2K x 4K devices have been demonstrated. [77]

### ***P-channel CCD Power Estimates***

The power requirement for a p-channel device should be similar to the requirements for the standard CCD given above. [77]

### Future Work

A useful enterprise for improving the device would be to marry the low light level technology with the p-channel process. This could provide a photon counting CCD that has significantly higher radiation tolerance than is available today.

**Table J-3: Sensor Characteristics**

	CCD	L3CCD	Impactron	CMOS	p-channel
<b>9 micron pixel</b>	Demonstrated	Demonstrated	Demonstrated	Demonstrated	Possible
<b>8K x 8K format</b>	Demonstrated	Demonstrated	Demonstrated	Demonstrated	Possible
<b>Gain</b>	No	Yes	Yes	Development needed	No
<b>No. Outputs</b>	8-16	8-16	8-16	8-16	8-16
<b>Read noise</b>	1-3 e- rms	~0 e-	~0 e-	TBD	2-3 e- rms
<b>DarkCurrent @ 300K</b>	< 100 pA/cm <sup>2</sup>	< 100 pA/cm <sup>2</sup>			
<b>QE (350-1000 nm)</b>	>70-90% with AR coating development	70-95% with AR coating development			
<b>Radiation Tolerance</b>	Low	Low	Low	High	Medium
<b>Random Access</b>	No	No	No	Yes	No
<b>Power</b>	Medium	High	Medium	Low	Medium
<b>High Voltage</b>	No	Yes	Yes	No	Yes

### Summary of Technologies

The advantages, concerns and development needs of four candidates have been discussed and are summarized below.

#### Conventional CCD

Advantages:

- Low noise
- Very low dark current
- Main stream technology
- High yield
- High quantum efficiency
- Large formats available (e.g. 2k x 2k, 4k x 4k, & 8k x 8k)
- Relatively low cost for a custom design
- TRL = 9

Concerns:

- CTE degradation under radiation exposure
- No on-chip gain to eliminate read noise
- Frequently requires more complex support electronics
- Sequential readout only (no random access of pixels)

Needed Development:

- None

#### Electron Multiplying CCD: e2v L3CCD

Advantages:

- Gain register provides effectively 0 read noise
- Low dark current
- High quantum Efficiency
- 2K x 2K available now

Concerns:

- Need to read out at high speed to do photon counting
- Gain register requires a ~40 V clock
- Spurious charge
- Single source for these parts
- TRL = 5 to 6

Needed Development:

- Second source
- Reduce the magnitude of the voltage swing in gain register
- Develop larger devices
- Bring to TRL 9.

**Electron Multiplying CCD: TI Impactron**

Advantages:

- Gain register provides effectively 0 read noise
- High quantum Efficiency
- Low dark current
- Photon counting

Concerns:

- High voltage needed on one serial phase
- High speed readout to maintain photon counting
- Single source
- TRL = 4 to 5

Needed development:

- Larger devices
- Thinned versions
- Second source
- Bring to TRL Level 6

**CMOS (monolithic)**

Advantages:

- Multiple sources – mainstream technology
- Low dark current
- Harder in a radiation environment
- Very high unit cell gains can yield lower input referred noise
- Windowed readout modes available

Concerns:

- Lower quantum efficiency than other technologies
- Very high gains demonstrated by only a couple of vendors
- Custom designs can be very expensive
- Backside CMOS is at TRL = 5 to 6

## Advanced Technology Large-Aperture Space Telescope (ATLAST)

### Needed Development:

- Mature backside processing – multiple vendors
- Develop in-pixel gain

### **P-channel, Fully-depleted CCD**

#### Advantages:

- 3-10X harder in a radiation environment than n-channel devices
- Very high red quantum efficiency especially in the NIR
- Low noise

#### Concerns:

- Cosmic ray events
- High dark current
- No gain mechanism to eliminate the read noise
- Limited sources
- TRL 5 to 6

#### Needed Development:

- Bring to TRL 9

At present, it would be possible to build the 32K x 32K focal plane using off the shelf 4K x 4K conventional CCDs. This would require sacrificing some noise performance and the ability to do single photon counting. The L3CCD and Impactron technologies are ready and available, but the desired device size has never been built to our knowledge. Consequently, they would need to be custom devices. The longer term solution may be the CMOS detector due to radiation hardness, expected availability and power/mass/volume considerations.

A roadmap is proposed for two of the device families. The developmental projects that would need to be undertaken to produce the L3CCD-base focal plane array system are:

1. Perform the trade study between a mosaic of 4K x 4K or 8K x 8K chips.
2. Execute a program to reduce the effects of the high voltage on the serial phase to reduce aging effects, improve reliability, reduce on-chip power dissipation, and simplify the drive electronics.
3. Develop the AR coating to achieve 70-90% QE from 350-900 nm.
4. Design and fabricate the chip(s) for the focal plane array.
5. Develop a second vendor source.
6. Collect qualification, performance, environmental and radiation data on fabricated devices.
7. Develop the FPA package.
8. Design the mating low-noise focal plane electronics.

There are some features that need to be developed to make the CMOS detector a viable low noise candidate:

1. Improve the ROIC design to reduce read noise
2. Mature back-side processing
3. Develop the AR coating to achieve 70% QE
4. Design and fabricate devices
5. Collect qualification, performance, environmental and radiation data on fabricated devices
6. Develop a second vendor source
7. Package development
8. Low noise electronics development

Of course, both device types will need to be qualified to TRL 9.

## Appendix K: Evaluation of Coronagraphic Techniques for *ATLAST*

In this appendix we discuss various coronagraphic options for *ATLAST*, excluding the visible nulling coronagraph. This documents our conclusion that for a segmented telescope, a nulling coronagraph is the only currently viable option for achieving the high contrast required to study exoplanets in the Habitable Zones of nearby stars. For a monolithic telescope, several coronagraphic techniques are possible.

### *Classical Lyot coronagraphs (amplitude focal plane masks)*

The most thoroughly studied stellar light suppression system is the classical Lyot coronagraph. While originally developed for solar observations, it has been adapted for high contrast imaging around stars. The basic design (Figure K-1) incorporates an amplitude mask at an intermediate focus that blocks the core of the stellar PSF. After this occulter, additional optics form an image of the entrance pupil (usually the primary mirror). Because of filtering of the wavefront by the occulter, light in this pupil is concentrated around any edges (e.g. entrance aperture, secondary obscuration and spiders, segment gaps). Another mask, the *Lyot stop*, blocks these bright regions but is otherwise clear. Light from a source not located behind the focal plane occulter, such as a planet, does not get filtered and appears in the pupil as a uniform distribution of flux. It can pass through the clear regions of the Lyot stop, though with some reduction.

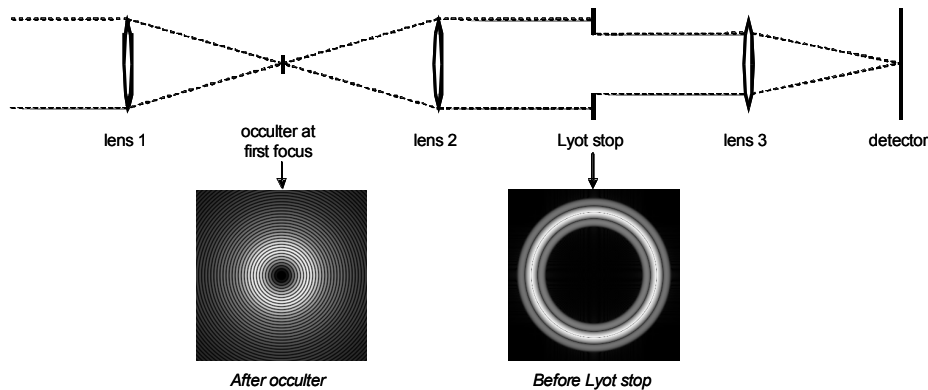


**Figure K-1.** Schematic layout of a simple Lyot coronagraph. Light enters the system from the left side. In this example, the Lyot stop would mask everything in the pupil outside of the central dark region.

There is a relationship between the size and shape of the occulter and the profile of the light around the edges of the subsequent reimaged pupil (hereafter called the *pupil leakage profile*), and this is critical to understanding the limitation of the Lyot coronagraph when applied to segmented and obscured systems. As the occulter size increases, the leakage profile becomes narrower. While this provides for higher throughput because the Lyot stop can be more open, it limits the inner radius at which sources may be detected near the star. Any Lyot coronagraph design requires a compromise between throughput and inner working angle (IWA).

The shape of the occulter transmission profile also affects the leakage profile (Figure K-2). The most basic occulter is a hard-edge circular spot. While easy to manufacture, it does create a leakage profile with considerable ringing that extends well into the darker regions of the reimaged pupil. This creates a floor that cannot be reduced by shrinking the Lyot stop.

Occulters with graded transmissions can reduce the ringing and provide higher contrast performance and greater throughput than the similarly-sized hard edge masks. By convention, the inner working angle of a graded occulter is defined as the radius at which it has 50% intensity transmission. A class of graded mask called a *band-limited occulter* [50] can theoretically produce a leakage profile with finite extent, so that in combination with an appropriate Lyot stop all the light from a star is suppressed. Such masks also provide reduced sensitivities to low-order aberrations [51]. To date, these occulters have produced the highest coronagraphic contrasts measured in a laboratory setting ( $\sim 6 \times 10^{-10}$  in a 10% bandpass on the High Contrast Imaging Testbed at JPL; [52]). The Lyot stop transmission is generally lower with more aberration-tolerant, higher-order occulters. Band-limited occulters that combine both amplitude and phase terms (via dielectric coatings) have been devised that have narrower leakage profiles [52].

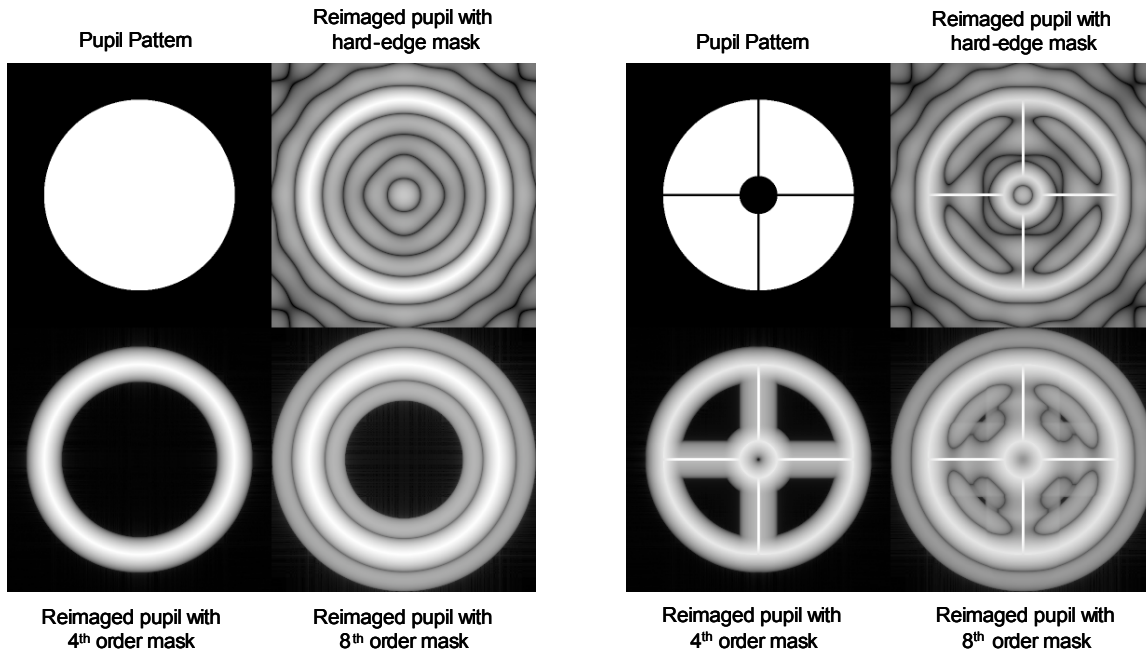


**Figure K-2.** Computed images of the intensity in the reimaged pupil plane after masking by an occulter in the prior image plane. The image contrast is adjusted to emphasize low-level features. The masks have a HWHM of  $4\lambda/D$  ( $4\lambda/D$  radius for the hard-edge occulter). The images are the same size.

Due to the leakage profile, even a small obscuration can affect a large area of the pupil, and the region that must be masked by the Lyot stop to obtain the required contrast may cause an unacceptable loss of throughput. In cases where the leakage profiles overlap, it may be impossible to obtain the necessary contrast (Figure K-3). The amount of light in the image plane due to unmasked leakage from obscurations is proportional to the square of the obscuration's area. In segmented pupils, the leakage profiles can easily overlap, even for large band-limited occulters. For moderate contrast imaging ( $>10^{-5}$ ) using ground-based telescopes without extreme

adaptive optics, where scattered light from uncontrolled wavefront errors is greater than the leakage, this may not be a limiting factor. The same is true for coronagraphs on the James Webb Space Telescope, which has no deformable mirrors to reduce wavefront errors caused by imperfect optics.

Any material that may be used to create the graded transmission occulter will introduce a phase change that is generally proportional to the transmission. This makes it more difficult to obtain a broadband dark field using a deformable mirror. Dielectric coatings that compensate for these phase shifts have been proposed and will be implemented soon on the High Contrast Imaging Testbed (HCIT) at JPL.

### *Feasibility with a Segmented ATLAST*

None: With a segmented aperture like that assumed for the 9.2m or 16m *ATLAST*, the overlapping leakage profiles prevent a Lyot coronagraph from achieving  $10^{-10}$  contrast for any reasonably-sized occulter. The situation simply gets worse with a central obscuration and spiders.

### *Feasibility with a Monolithic ATLAST*

Possible with unobscured, not with obscured: A Lyot coronagraph with a band-limited occulter would be feasible with an unobscured, off-axis telescope. With an on-axis, centrally-obscured scope, the throughput would be too low for a  $4\lambda/D$  occulter size with an 8<sup>th</sup>-order occulter, but perhaps feasible for a 4<sup>th</sup>-order. Note that the TPF-C program chose an 8<sup>th</sup>-order over a 4<sup>th</sup>-order occulter to bring the aberration tolerances into the realm of feasibility.

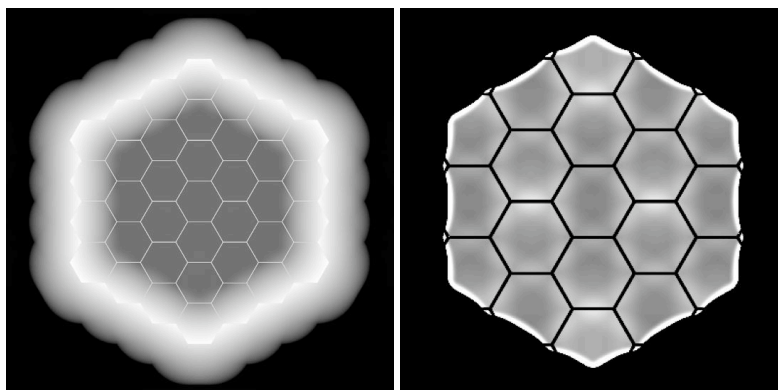


**Figure K-3.** **LEFT:** Intensity at the reimaged pupil plane after a 4<sup>th</sup> order band-limited occulter for a segmented aperture. The image has been stretched to show the low-level light that fills the interior of the segments due to overlapping leakage profiles. The interior needs to be completely dark to achieve  $10^{-10}$  contrast. **RIGHT:** Interior region of the pupil after masking of the segments and outer aperture, as would be done in the first stage of a multi-stage coronagraphic system. This demonstrates that the interior light is not suitably uniform to allow such a system to achieve  $10^{-10}$  contrast.

### ***Multi-stage Lyot coronagraphs***

With a segmented pupil and a Lyot coronagraph, leakage profiles will overlap and fill the interior of the segments with light, as seen in the reimaged pupil. After masking with the Lyot stop, the pupil resembles a sparse aperture with quasi-uniform illumination. This can be used as the pupil for a subsequent imaging system feeding another coronagraph [53]. This method only works on highly segmented telescopes as it requires the leakage profiles to overlap significantly to provide the nearly-uniform pupil illumination. The application of two coronagraphs significantly reduces the throughput and resolution of the system.

This method is not suitable for a segmented *ATLAST* as it requires small segments, and even if *ATLAST* had them, the overlapping pupil leakage profiles would not be sufficiently uniform to allow the second coronagraph to provide  $10^{-10}$  contrast (Figure K-3, left hand image).

#### ***Feasibility with a Segmented ATLAST***

None: The output pupil of the first stage of a coronagraph on a segmented telescope is not sufficiently uniform for additional stages to achieve  $10^{-10}$  contrast.

#### ***Feasibility with a Monolithic ATLAST***

Possible with unobscured, not with obscured: A multi-stage coronagraph would work successfully on an unobscured telescope, though the additional elements create unnecessary complexity, given that single-stage coronagraphs are feasible. On an obscured telescope, the output pupil from the 1<sup>st</sup> stage of the coronagraph is not sufficiently uniform for additional stages to provide sufficient contrast.

### ***Lyot coronagraphs with focal plane phase masks***

A variation of the Lyot coronagraph replaces the amplitude focal plane mask with one that alters phase instead. Phase masks can theoretically allow imaging closer to the star ( $1 - 2\lambda/D$ ) and with higher throughput than amplitude masks. The most studied are the four-quadrant and optical vortex masks.

Phase masks are not compatible with obscured or segmented telescopes at the contrast levels required for *ATLAST*. As shown in Figure K-4, phase masks have pupil leakage profiles like “normal” Lyot coronagraphs, except the profile is highly asymmetric. For an unobscured aperture, the leakage is confined outside of the pupil, allowing for a very “open” Lyot stop with high throughput. However, when obscurations are introduced, leakage fills the pupil interior, so shrinking the Lyot stop will not help.

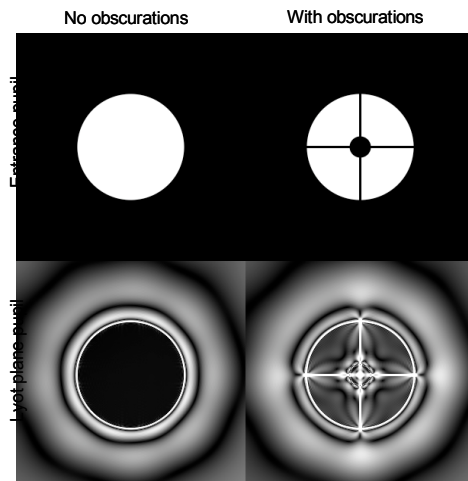


**Figure K-4.** (Top) Entrance pupil patterns. (Bottom) Corresponding intensity patterns at the reimagined pupil following an optical vortex phase mask (charge=4) placed in the focal plane.

### ***Feasibility with a Segmented ATLAST***

None: Leakage from segments fill the interior of the reimagined pupil with light that cannot be blocked with a Lyot stop.

### ***Feasibility with a Monolithic ATLAST***

Possible with unobscured, not with obscured: Pupil leakage with an obscured telescope is too great to remove using the Lyot stop. With an unobscured telescope, phase masks are viable. The best contender is the optical vortex, which may be implemented using different schemes. Some utilize stepped masks to implement the phase shift, but fabrication issues are significant. The most promising technique utilizes subwavelength gratings [54]. The aberration sensitivity of these masks is dependent on the number of  $2\pi$  phase shifts (the charge) they impose. In general, phase masks are sensitive to registration with the star and require rapid tip-tilt correction.

### ***Pupil apodization***

By tapering the transmission in the entrance pupil (either at the entrance pupil or a reimagined version of it) so that throughput decreases to zero at the outer radius, the ringing in the wings of the diffraction pattern can be greatly reduced. If the pupil is segmented or obscured, then each clear subaperture must be individually apodized.

The primary disadvantage of apodization is the large decrease in throughput. Also, it increases the core width of the point spread function, reducing its sharpness and contrast. It is currently not possible to create an apodized transmission mask, even for an unobscured system, that provides  $10^{-10}$  contrast over a broad passband.

An alternative method of apodization, called phased induced amplitude apodization (PIAA), remaps the pupil using two mirrors [55]. One mirror remaps the pupil to form the required apodization and the second compensates for the path differences the remapping induces. A mild conventional apodizer is also required to reduce diffraction effects caused by the PIAA mirrors, which have large curvatures at the outer radii [56]. The system creates a PSF with suppressed wings whose core is then blocked by an occulter. A subsequent set of inverse PIAA optics reverses the remapping to reform a “normal” image with the star greatly suppressed. PIAA has the potential to provide high-throughput imaging at inner radii of  $1-2 \lambda/D$ .

### ***Feasibility with a Segmented ATLAST***

None: The segmented nature of the 16m precludes apodization. Each segment would need to be apodized, resulting in a huge transmission reduction as well as a large impact on resolution. The PIAA design, which significantly distorts the pupil, cannot handle segments or a central obscuration and deliver  $10^{-10}$  contrast performance.

### ***Feasibility with a Monolithic ATLAST***

Possible with unobscured, unlikely with obscured (PIAA not possible): Apodization using a transmission mask is theoretically feasible with an unobscured telescope, but fabrication and transmission-induced phase offsets (see the Lyot coronagraph section) make broadband PSF suppression difficult. The PIAA concept would work with an unobscured system. PIAA optics are difficult to manufacture and are very sensitive to alignment errors. Small working angles are possible, but rapid low-order wavefront sensing is required. PIAA can effectively apodize a circular pupil, but not obscurations within the pupil.

### ***Phase modification in the pupil***

By manipulating the phase of the wavefront in a pupil, either with a deformable mirror or a spatially-varying phase plate, diffracted light can be made to interfere with itself at the image plane. The suppression occurs in a region limited at its outer radius by the number of actuators across the pupil or the maximum spatial frequency in the phase plate [57]. A DM can suppress both the diffraction pattern and scattered light from wavefront errors. While the analysis has not yet been done, this method is unlikely to be applicable to broadband  $10^{-10}$  contrast observations due to the required high DM stroke, significant polychromatic diffraction variations, and sensitivity to alignment.

### ***Shaped Pupils***

By altering the shape of the pupil, diffraction can be confined to selected regions of the PSF. Light diffracts perpendicular to an edge. A flat edge diffracts light into a spike (like the diffraction spikes from the secondary support spiders). A circular aperture or obscuration can be thought of as an arrangement of infinitely small straight edges arranged in a circle, so that the

corresponding diffraction spikes are uniformly distributed in azimuth. A square aperture will have a PSF comprising a square core and narrow diffraction spikes perpendicular to the edges, with a very low level of light along the diagonal extents, providing an intrinsically high-contrast capability compared to a circular aperture.

More advanced shaped apertures have been devised that utilize the diffracted light to create dark regions of very high contrast ( $10^{-10}$ ). By altering the shapes, the dark regions can be tailored for specified inner working angles, bandpass widths, and other desired characteristics. Experiments on HCIT have provided contrasts in the  $10^{-9}$  range over 10% bandpasses.

Shaped pupils have some notable advantages over other starlight suppression methods. They are essentially immune to pointing errors – the position of the PSF will change, but the dark zones will be unaffected. They can operate over very broad passbands. They are also relatively easy to fabricate, and are easy to use by placing them in a pupil plane.

The shaped pupil also has some serious disadvantages. They have low transmission, and they significantly reduce the resolution of the telescope. The light that would otherwise fall inside the dark regions is instead concentrated into bright cones that must be blocked by a focal plane mask as early as possible to prevent additional scatter by subsequent optics and detector saturation. This cone of light also prevents imaging over a significant portion of the field. The dark region close to the star is especially limited in azimuth.

On a segmented telescope, a pupil-plane mask containing multiple shaped pupils, one for each segment, would be required. This would result in both a very low transmission and a significant loss of resolution.

### ***Feasibility with a Segmented ATLAST***

None: Each segment would require a shaped pupil, and the resulting loss of throughput and resolution would be too great to make an effective planet imager.

### ***Feasibility with a Monolithic ATLAST***

Possible: With an unobscured system, a wide variety of shape pupils can be designed to meet specific inner working angle and contrast needs. With an obscured system, the unobscured subapertures would each have a corresponding shaped aperture. Because the shaped pupil masks are easy to manufacture and implement (just by putting a mask in a pupil wheel, for instance), they make good backup suppression systems. The throughput, low resolution, and limited dark fields are drawbacks, making other coronagraphs (notably for the unobscured systems) more effective.

### ***Off-axis vs. On-axis Lyot Coronagraphy and a Comparison to the VNC Performance with a Segmented Telescope***

A conventional on-axis telescope with a multi-vaned spider supporting a secondary mirror prohibits the use of most coronagraphic techniques except some that operate only in pupil space (e.g. the visible nuller, shaped pupils). The interferometric techniques (VNC, pupil swapping, AIC) provide only 2<sup>nd</sup> or 4<sup>th</sup> order rejection of low-order aberrations and stellar disc leakage, and they are very complex to implement. Shaped pupils, while easy to create, provide low throughput.

Lyot coronagraphs utilizing a band-limited mask in the image plane and a Lyot stop in a pupil plane are simple to implement and can provide 8<sup>th</sup> order aberration rejection, significantly reducing the requirements on the telescope pointing and optics. However, any obscurations in the pupil present problems for coronagraphy. Lyot coronagraphs (classical, band-limited, and image-plane phase masks (e.g. optical vortex, four quadrant) modify the wavefront at an intermediate focus. At a subsequent reimaged pupil, this results in a concentration of residual starlight outside of the pupil or around obscurations within it (spiders, secondary mirror). This light is blocked with a pupil-plane mask (Lyot stop), which has apertures that allow light from off-axis sources (planets) to pass through to the final image plane. Depending on the size and design of the image plane mask, the light around the obscurations may extend over a large area of the pupil and may overlap so much that it becomes impossible to stop down enough of the pupil to achieve the necessary amount of diffraction suppression without reducing throughput to nearly zero.

It becomes clear that to optimize both throughput and contrast with a Lyot coronagraph an off-axis design is optimal as the only region that needs to be masked by the Lyot stop is around the pupil edge. If obscurations are unavoidable, the simplest pupils are best. Presented here are quick evaluations of 4<sup>th</sup> and 8<sup>th</sup> order band-limited Lyot coronagraphs when used on unobscured and obscured systems proposed for the *ATLAST-8m*. The performance estimates are compared to that for the *ATLAST-16m* with a visible nulling coronagraph.

### **Simulations**

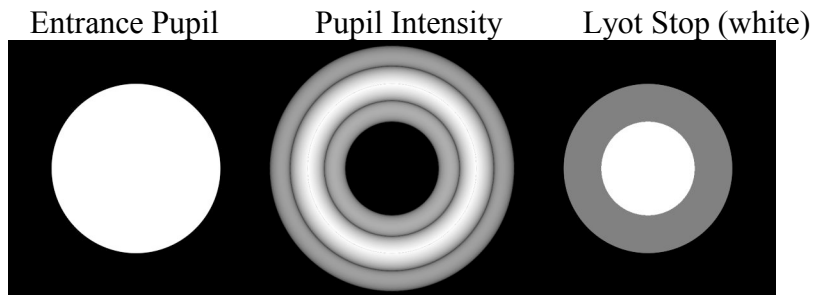
To demonstrate the effects of the obscurations, we computed the pupil plane intensities after occulting the star with a band-limited mask. In the figures that follow, the entrance pupil is shown on the left. Any subapertures appear in white superposed on the grey entrance pupil. The intensity distribution of an occulted star at the reimaged pupil plane, prior to the Lyot stop, is shown in the middle panel. On the right is shown the clear region of the Lyot stop (white) superposed on the entrance pupil (grey/black). The occulters used for the images are all 8<sup>th</sup> order band-limited masks with HWHM=51.5 mas ( $4\lambda/D$ ,  $\lambda=500$  nm,  $D=8$ m). A 20% central obscuration is used for the on-axis cases. The pixel sampling is 5.15 mas (slightly better than Nyquist).

Except for the off-axis cases using circular/elliptical occulters, linear occulters are used for the more complex pupils. They provide better throughput because the Lyot stop only needs to reduce the pupil size along one direction. The linear occulter can mask a single diffraction spike,

allowing for high contrast imaging when a one-dimensional support is used for the secondary. The tradeoff is that a linear occulter does not provide a 360° field around the star. This is significant when working near the inner working angle (IWA) where linear occulter masks a large fraction of the local area. If roll subtraction is needed to remove the instrumental background contribution, then a planet at the IWA will be behind the occulter at one of the two rolls. In this case only one roll provides useful planet signal. With a circular occulter both rolls provide planet signal, decreasing the total integration time spent on the star.

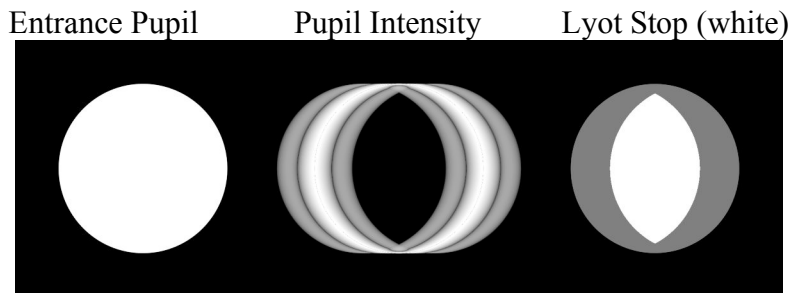
### Off-Axis Circular/Elliptical Primary with Circular/Elliptical Occulting Mask

The simplest pupil configuration is a circular off-axis system with no obscurations. This allows a circular occulting mask to be used and provides 360° field coverage at any usable radius. An 8m off-axis circular primary cannot fit in an Ares V due to space needed along the side for the secondary tower, but an elliptical 8m x 6m can. The elliptical system uses an elliptical occulter that has the same IWA along the resulting elongated PSF's minor axis as the circular system's IWA.



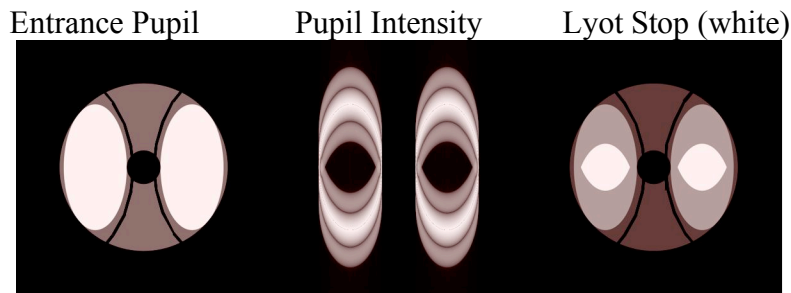
### Off-Axis Circular/Elliptical Primary with Linear Occulting Mask

By using a linear (bar) occulter instead of a circular one, the effective pupil shear introduced by the mask is confined to one direction. This improves the throughput and resolution relative to the same system with a circular occulter. However, the linear mask will block the image of a planet near the inner working angle when the telescope is rolled for background subtraction, so only one of the two roll orientations is useful for integrating planet signal. With an elliptical primary, the long axis of the occulter is placed along the long axis of the elongated PSF.



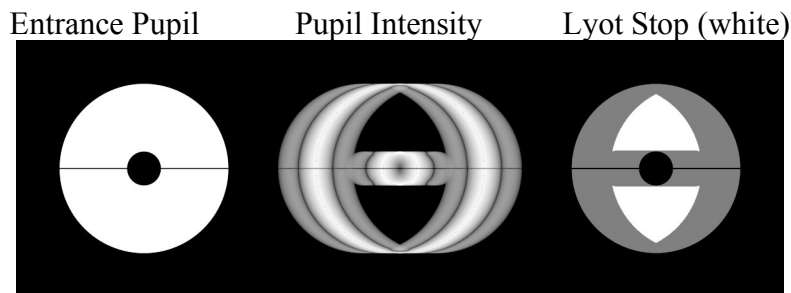
### On-Axis with Arced Spiders, Elliptical Subapertures, and Linear Occulting Mask

One way of providing a larger unobscured pupil region in an on-axis system is to bend the spiders, as suggested by Phil Stahl. The arced vanes provide two unobscured, elliptical regions, each about 6m by 3m in size. The secondary mirror obscuration hides between the two ellipses. These apertures would be implemented by placing an aperture mask at an image of the entrance pupil at a location prior to the coronagraph. This could be at the 1<sup>st</sup> deformable mirror, though this prevents the use of selectable pupil masks (the pupil mask must be at a sharp pupil image). It is necessary to use a linear occulting mask to provide the maximum throughput. Optical modeling shows that it is not necessary to use separate coronagraphs for each elliptical subaperture. The small apertures produce a broad planet PSF with a fringe pattern superposed.



### On-Axis with Linear Spiders

A more efficient on-axis configuration supports the secondary mirror with struts aligned only along one direction. These create a diffraction spikes along one direction in the image plane. A linear occulter is aligned with the spikes, essentially masking out the contribution of the spider to the diffraction pattern. After the occulter a two-aperture Lyot stop can be used. This system provides much better throughput and PSF quality than the two-ellipse one, but it may not be possible to support the secondary with just two spiders along one direction. Note that things fall apart if another spider is added at any angle not aligned with the other spiders.



## Advanced Technology Large-Aperture Space Telescope (ATLAST)

**Table K-1: Statistics for 8m System with an 8<sup>th</sup>-Order Occulter (V=5.5 G2V Star)**

	Off-Axis with Circular Occulter	Off-Axis with Linear Occulter	8x6m Off-Axis w/Elliptical Occulter	8x6m Off-Axis w/Linear Occulter	On-Axis with Linear Occulter	Two 6x3m Ellipses w/Linear Occulter
Lyot Stop Throughput	30%	42%	20%	30%	29%	14%
PSF FWHM (mas)	24	26 x 16	26 x 35	27 x 22	28 x 14	46 x 49
PSF Peak Value	0.012	0.023	0.005	0.011	0.010	0.003
PSF Sharpness	0.018	0.025	0.011	0.017	0.012	0.006
SNR=10 time (no zodi)	16 hr	12 hr	23 hr	16 hr	19 hr	37 hr
@ IWA	24 hr	19 hr	35 hr	25 hr	29 hr	54 hr
(with 2 rolls)	(24 hr)	(38 hr)	(>35 hr)	(50 hr)	(58 hr)	(108 hr)
SNR=10 time (1 zodi)	33 hr	24 hr	53 hr	34 hr	42 hr	87 hr
@ IWA	49 hr	36 hr	77 hr	50 hr	61 hr	125 hr
(with 2 rolls)	(49 hr)	(72 hr)	(>77 hr)	(100 hr)	(122 hr)	(250 hr)
SNR=10 time (10 zodi)	99 hr	70 hr	157 hr	102 hr	124 hr	257 hr
@ IWA	142 hr	101 hr	225 hr	146 hr	178 hr	366 hr
(with 2 rolls)	(142 hr)	(202 hr)	(>225 hr)	(292 hr)	(356 hr)	(732 hr)

**Table 2: Statistics for 8m System with a 4<sup>th</sup>-Order Occulter (V=5.5 G2V Star)**

	Off-Axis with Circular Occulter	Off-Axis with Linear Occulter	8x6m Off-Axis w/Elliptical Occulter	8x6m Off-Axis w/Linear Occulter	On-Axis with Linear Occulter	Two 6x3m Ellipses w/Linear Occulter
Lyot Stop Throughput	49%	62%	37%	46%	52%	29%
PSF FWHM (mas)	19	19 x 15	19 x 26	20 x 19	18 x 14	11 x 30
PSF Peak Value	0.030	0.049	0.017	0.026	0.035	0.011
PSF Sharpness	0.028	0.036	0.021	0.027	0.022	0.013
SNR=10 time (no zodi)	11 hr	9 hr	13 hr	11 hr	12 hr	18 hr
@ IWA	17 hr	15 hr	21 hr	18 hr	19 hr	28 hr
(with 2 rolls)	(34 hr)	(30 hr)	(>42 hr)	(36 hr)	(38 hr)	(56 hr)
SNR=10 time (1 zodi)	21 hr	16 hr	27 hr	22 hr	23 hr	40 hr
@ IWA	31 hr	25 hr	41 hr	33 hr	35 hr	59 hr
(with 2 rolls)	(31 hr)	(50 hr)	(>41 hr)	(66 hr)	(70 hr)	(118 hr)
SNR=10 time (10 zodi)	61 hr	47 hr	82 hr	64 hr	67 hr	119 hr
@ IWA	88 hr	69 hr	118 hr	93 hr	97 hr	171 hr
(with 2 rolls)	(88 hr)	(138 hr)	(>118 hr)	(186 hr)	(194 hr)	(342 hr)

**Lyot Stop Throughput** = Percentage of planet light that passes through Lyot stop relative to an unobscured circular aperture

**PSF FWHM** = Full width at half maximum intensity of PSF

**PSF Peak Value** = Fraction of total flux in peak pixel of the PSF including throughput reduction due to Lyot stop but no reflectivity losses

**PSF Sharpness** = measure of PSF distribution; SNR is proportional to sqrt(sharpness) for matched filters.

**SNR 10 time:** Time required to achieve SNR=10 measurement (matched filter) of a planet signal in one bin of an R=70 spectrum for a  $10^{-10}$  contrast planet around a star with 1x and 10x solar zodiacal depth disk. For values at the inner working angle (IWA), the 50% occulter throughput reduction at that radius is included and the values in parentheses indicate the time required to get both the planet signal and then the background separately via roll subtraction; some configurations, like the linear occulter, obtain planet signal at the IWA at only one roll.

**Assumptions:** Instrumental background contrast =  $10^{-10}$ , 12 reflections, 97% reflectivity per surface, 90% CCD QE, mean solar Zodi=23 mag/arcsec<sup>2</sup>, V=0 G2V star flux is  $10^7$  photons/sec/cm<sup>2</sup>/μm @ 500 nm.

### Impact of Configuration on Exposure Times

The shape of the planetary PSF is determined by the Lyot stop. The more the pupil is masked, the larger and less “sharp” the PSF becomes. The larger the PSF, the greater the amount of extended background light (sky, exozodiacal disk) is included within the PSF core. This has an effect on the exposure time required to achieve a given signal-to-noise level. The times required to achieve an SNR=10 in the matched-filter case over an R=70 spectral resolution bandpass bin are given in Tables 1 and 2 for the 8<sup>th</sup> and 4<sup>th</sup> order occulter (zero read noise assumed and *no losses are assumed from reflections within a spectrograph*). When working at the inner working angle, the 50% transmission reduction at that radius due to the occulter is included. A circular occulter allows integration of the planet signal at the IWA at both roll angles when roll subtraction is used, but a linear occulter does not. So, the IWA exposure times include, in parentheses, the time required to achieve the planet SNR and get a background image at a second roll.

A 4<sup>th</sup>-order occulter provides shorter exposure times relative to an 8<sup>th</sup>-order but at the cost of greatly increased sensitivity to low-order aberrations and leakage from partially-resolved stellar discs. Regardless of occulter order, the two-ellipse configuration is by far the worst, with exposure times 2-3x longer than the best off-axis case. The off-axis linear occulter system provides the best performance at first glance, but the off-axis circular occulter wins when roll subtraction is necessary for extracting the planet signal from the background near the IWA. While the on-axis linear occulter appears viable in terms of exposure time, it does have half the efficiency at the IWA when rolls are included.

This highlights the issue of the assumed method of extraction of the planet signal from the background at the IWA. If roll subtraction must be used, then a circular occulter on an off-axis system is much more efficient than other configurations. If, however, the planet’s spectral features can be extracted by filtering the planet+background spectrum rather than rolling, then an on-axis system with a linear occulter requires only a small increase in exposure time.

### Comparison to the 16m VNC

Similar performance estimates have been computed for the segmented *ATLAST-16m* telescope with a visible nulling coronagraph. The VNC pupil shears result in a 50% loss of light, with additional losses due to the many reflections and transmissions from the numerous VNC optics (no fibers were used). The segment-sized pupil shears produce an IWA of  $3\lambda/D$  (19.3 mas @ 500 nm). The pixel sampling is 2.6 mas (proportional to the 8m sampling given the larger aperture), and there are 22 reflections @ 97% and 10 transmissions @ 99% efficiency. Note that the VNC has an aberration sensitivity similar to a 4<sup>th</sup> order Lyot coronagraph. Also, the IWA of the 16m is less than half that of the 8m, so 8m IWA values should be compared to non-IWA 16m values.

## Advanced Technology Large-Aperture Space Telescope (ATLAST)

The interferometric nature of the VNC results in a fringe pattern of high and low transmission on the sky. A planet at a known location relative to the star must be placed in a high-transmission fringe by rolling the telescope. When a second roll is required for subtraction, there may or may not be another high-throughput fringe available at that roll and radius from the star, so it is possible that the exposure time will need to be doubled for planets that are large distances from the star. Planets near the IWA will probably need double the exposure time due to the elongated shape of the fringe transmission pattern.

**Table K-3: Statistics for *ATLAST-16m* with VNC (V=5.5 G2V Star)**

VNC Lyot Throughput =	50%
PSF FWHM =	8 x 9 mas
PSF Peak Value =	0.023
PSF Sharpness =	0.0135
SNR=10 time (no zodi) =	5 hr (10 hr?)
@ IWA =	9 hr (18 hr)
SNR=10 time (1 zodi) =	8 hr (16 hr?)
@ IWA =	14 hr (28 hr)
SNR=10 time (10 zodi) =	24 hr (48 hr?)
@ IWA =	37 hr (74 hr)

The 16m with VNC is about twice as efficient as the best case 8m. Because of the reduced throughput of the VNC due to the numerous reflections and the reduction of sharpness due to the large effective central obscuration in the sheared output, the efficiency of the 16m is much lower than one would expect by just scaling the 8m results. Because of the higher resolution of the 16m and the 4<sup>th</sup>-order aberration sensitivity of the VNC, the pointing requirements are much tighter, especially if the stellar radius is >0.5 mas. It is also not possible to use an 8<sup>th</sup> order occulter on the segmented 16m.

## Appendix L: *ATLAST* Starshade Design and Technology

An external occulter offers some key advantages for starlight suppression. These are:

1. Much less stringent constraints on the required wavefront quality provided by the telescope optical assembly, which means terrestrial-size exoplanet characterization can be performed using more conventional telescope design (e.g., on-axis secondary).
2. Decoupling between the inner working angle (IWA) and telescope aperture that results in a somewhat smaller IWA than can typically be achieved with an internal coronagraph.
3. There is no outer working angle limit. Outer working angle is limited only by the fields of view of the telescope's scientific instruments.
4. A starshade has 100% transmission for objects beyond its projected geometric diameter, providing at least a factor of 2 better throughput than a typical internal coronagraphic system.
5. The IWA of an external occulter can be adjusted **on orbit** to tailor the observation to different separations between a star and planet.

Northrop Grumman Aerospace Systems (NGAS) performed a detailed study of the starshade sizing, orbital constraints, mass limits, and launch vehicle requirements for the *ATLAST* concept. The results of that trade study are summarized here. Figure L-1 shows the NGAS concept for a starshade and its spacecraft that was developed for the New Worlds Observer (*NWO*) mission concept study. The *ATLAST* concepts would look similar.

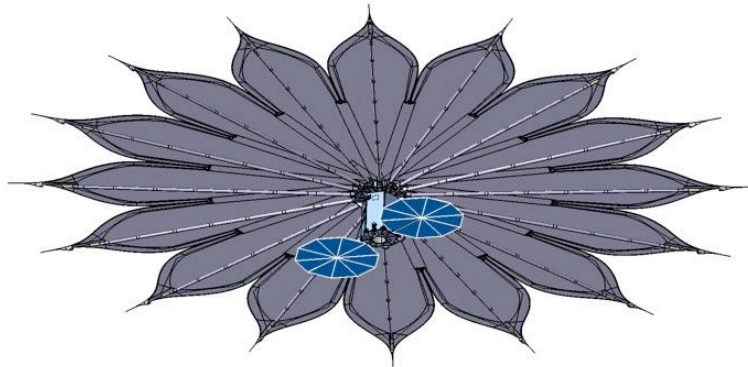


**Figure L-1.** Baseline Starshade design known as the "Blooming Onion." This is the design being proposed for the *NWO* mission concept. The *NWO* starshade has a diameter of 50 meters. The view here shows the anti-telescope side of the starshade.

### *Starshade Sizing*

In general, starshades work better at **shorter** wavelengths.

- Starshade size is a fast function of wavelength if all other requirements are the same.
- However, the star/planet contrast ratio requirement goes down for longer wavelengths.
- Starshades provide higher suppression at shorter wavelengths and lower suppression at longer wavelengths.

The contrast ratio in the image plane at the location of a planet is expected to 10 to 100 times better than the suppression ratio in Table L-1 below. For this study, the suppression factor is

## Advanced Technology Large-Aperture Space Telescope (ATLAST)

defined as the ratio of the integral of remaining starlight to the amount detected over the same band pass without a starshade. This remaining starlight will be spread over many image pixels, leading to a significantly higher contrast level.

Starshade size and distance is also a strong function of the IWA:

- Planets can be detected at least 20% inwards of the geometrical IWA of the starshade.
- This augmented IWA can be enhanced even more in the blue due to the higher suppression.

We sized starshades for the *ATLAST-8m* and *ATLAST-16m* using the requirements listed below. These values are highly requirements dependent; we made some judgment calls to ensure consistency. The initial requirements were suppression= $10^{-10}$ , IWA= $3\lambda/D$ , and wavelength range up to 1100 nm. These requirements, appropriate for an internal coronagraph, are not always appropriate for obtaining the optimal science from a starshade. For example, the *ATLAST-8m* IWA at  $3\lambda/D$  is 58 mas, which is very large and leads to a starshade not much bigger than that designed for the 4-m *NWO* telescope. With an external occulter we can take advantage of the fact that the starshade and the telescope are disconnected to push the IWA closer to  $2\lambda/D$  or  $\sim 40$  mas. We did not consider IWA smaller than this because the PSF of the telescope will lead to too much confusion between the residual stellar light and the planet.

**Table L-1: Starshade Requirements and Parameters for ATLAST Concepts**

Requirements				Derived Values		
$D_{tel}$ (m)	IWA (mas)	$\lambda_{max}$ (nm)	Suppression at $\lambda_{max}$	Starshade size (m)	Starshade distance (1000 km)	Notes
8	58	1000	1E-9	56	80	Specified requirements – similar to New World Observer
8	39	1000	1E-9	<b>80</b>	<b>165</b>	Changed IWA to $2\lambda/D$
8	58	1000	1E-7	45	63	Relaxed supp -- smaller than <i>NWO</i>
16	29	1000	1E-9	110	320	Specified requirements
16	40	1100	1E-9	<b>90</b>	<b>185</b>	Relaxed IWA req.
16	29	1000	1E-7	90	250	Relaxed suppression req.

Another adjustment is due to the fact that a planet with a contrast to the central star of  $10^{-10}$  can be seen even if the integral residual stellar light is at a level of  $\sim 10^{-8}$  to  $10^{-9}$ . The main reason for this is that the starlight is extended over many pixels and only 1% to 10% of the residual starlight ends up on the image pixel at the location of the planet. We therefore slightly adjusted the initial requirements to account for areas where the starshade could exceed the desired science return and to take into account constraints on starshade size and distance. **We ended up choosing an 80-m starshade at 165,000 km for *ATLAST-8m* and a 90-m starshade at 185,000 km for *ATLAST-16m*. These both have an IWA $\sim 40$  mas, which is about  $2\lambda/D$  for the 8-m and  $4\lambda/D$  for the 16-m (at 760 nm).** These sizes should be optimized once detailed science requirements

are established. Figure L-2 shows the suppression factor as a function of wavelength for the chosen *ATLAST* starshade parameters.

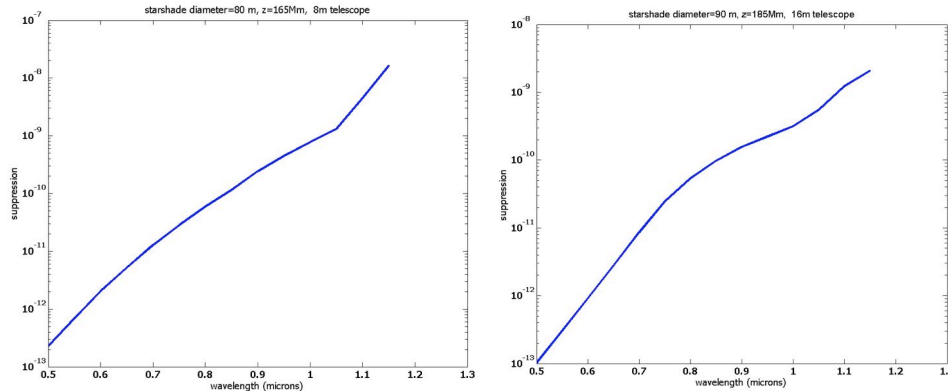
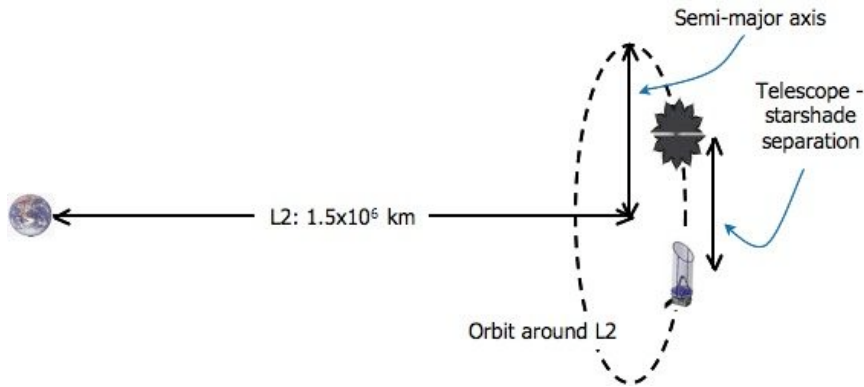


**Figure L-2. Left:** Suppression vs wavelength for the 80-m shade selected for *ATLAST-8m*. **Right:** Same plot but for the 90-m shade selected for *ATLAST-16m*. Starshade Orbits

### Starshade Orbits

A family of solutions exists for orbits around SE-L2. SE-L2 orbits require  $\sim 5$  m/s of  $\Delta v$  per year to maintain the orbit. Ideal starshade orbits start at orbits with semi-major axis much larger than the starshade-telescope separation, as indicated in Figure L-3. For large starshade separation, orbits should have the following characteristics:

- Narrow ellipse to maximize straight sections,
- Major to minor axis ratio approx. 1:0.3,
- Inclined to avoid eclipse & penumbra



The *ATLAST* starshades have optimal separations of 165,000 km and 185,000 km for the 8-m and 16-m, respectively.

#### Orbital limits:

- Semi-major axis should be  $\sim 400,000$  km or larger
- Semi-major axis should be  $\sim 900,000$  km or smaller

#### Ideal semi-major axis

size is between **600,000 km to 800,000 km**. Larger orbits require more fuel for station-keeping and the station-keeping error increases risk of rapid deorbit (kick out). Smaller orbits may incur eclipse and penumbra shadowing that significantly limits the field of regard and look direction and, hence, limit the usable portion of the orbit. **The current restriction on the maximum starshade – telescope separation is  $\sim 300,000$  km**. The usable portion of orbit remains high, at least 50% and the total field of regard is a full  $4\pi$  steradians.

***Starshade Targeting Efficiency***

To determine how efficiently we can target nearby solar-like star systems for observation, we select spectral type F,G,K stars from the Hipparcos catalog and identify, for both *ATLAST-8m* and *ATLAST-16m* those stars whose Habitable Zone (HZ) exceeds an inner working angle (IWA) of  $3\lambda/D$  at 760 nm (the O<sub>2</sub> absorption feature). As a detection goal, we assume that each star has an Earth-twin in its HZ (with  $\Delta\text{mag} = 25$ ), realizing that super Earths will be easier targets. We include plausible instrumental efficiencies and noise properties, and assume a 3-zodi background (local plus exosolar). We also include residual background from the star as an additional noise source. The goal of this exercise was to determine how many stars could be observed in a 5-year timeframe without exceeding 25% of the total observing time available (i.e., leaving ~75% of the time available for general astrophysics programs). The number of stars that can be observed depends on the time it takes for the starshade to maneuver into position. The *NWO* starshade uses 2 NEXT SEP thrusters. For the purposes of this observation modeling activity, we ran the simulations assuming the *ATLAST* starshade had 4, 8, and 16 such thrusters. The results are shown in Table L-2. The average slew times to the next target are longer for the 8-m telescope because the mean angular separation between possible target stars is larger (the 16-m has a higher density of target stars over the sky that it can observe)

While *ATLAST* can search for exoplanets to larger distances than smaller telescopes, we believe that *ATLAST's* most valuable contribution to exoplanet science would be to fully characterize known planetary systems. We expect that the detection of extrasolar planets will be well advanced by the time of the *ATLAST* launch and full characterization would provide higher return than searches. With the resolution and the collecting area of a 16-m telescope, *ATLAST* could observe individual exosolar systems for weeks. It could get high resolution spectra ( $R > 1000$ ) of all the planets in the system, watch for diurnal variations in their brightness and spectra, measure their polarization, etc.

**Table L-2: Maximum Number of Targets Observable with *ATLAST* and a Single Starshade**

Telescope Aperture (m)	Number of thrusters	Time for Avg. slew	Avg. observation cadence	Total observations in 5 years	Percent of time spent observing
8	4	17.7 days	~20 days	93	10
8	8	13.1 days	~15 days	122	13
8	16	10 days	~12 days	153	16
16	4	11.2 days	~13 days	138	15
16	8	8.3 days	~10 days	177	19
16	16	6.3 days	~7 days	218	24

Long observing sessions optimize the starshade's operational constraints. The most fuel-intensive part of a starshade's operation is moving from one star to the next. If the starshade were used to focus on the top few (tens to ~100) targets there would be less need for advanced thrusters with very high throughput and large amounts of fuel. Hence, a starshade that is

optimized for more extended visits to fewer targets (with the goal of producing higher SNR, higher spectral resolution data) would look quite different from a starshade designed to maximize the number of targets observed over the lifetime of the mission. This more specialized starshade system would compare very favorably with other options for starlight suppression.

***Starshade Fuel Consumption Considerations***

The main issues for the ATLAST starshade propulsion system are:

- Total propellant throughput
  - Both as a mass of fuel needed and as a thruster wear-out issue
- Adequate thrust generation to push starshade + fuel
  - Generally, getting more thrust out of a system means more input power

Existing thruster technology, such as NASA’s Evolutionary Xenon Thruster (NEXT), can be adequate. The NEXT thrusters are (almost) available technology. Northrop Grumman anticipates that the next generation of NEXT thruster could be more mass efficient. Furthermore, with some technology development, the thrust output for next generation ion thrusters can be adjusted to ATLAST performance needs. This would yield shortened slew times and/or increase mission cadence. The main challenge for getting higher thrust output is getting better fuel throughput. In all cases, the main technology hurdle associated with starshade engines is generating enough thrust.

***Table L-3: ATLAST Starshade Thruster Fuel Throughput and Mass Fraction***

	<b>4 Thrusters</b>	<b>6 Thrusters</b>	<b>8 Thrusters</b>
Nominal Throughput	2000 kg	3000 kg	4000 kg
Max. Throughput	2920 kg	4380 kg	5840 kg
Max. ΔV	10.68 km/s	14.57 km/s	17.86 km/s
# exoplanet targets (optimized)	100	127	140
Fuel mass fraction	< 30%	33%	38%

The NEXT system currently has a ~500 kg Xenon throughput baseline, with an estimated 730 kg wear-out limit per thruster. Using this baseline, Table L-3 shows the performance that could be achieved for an ATLAST starshade with the indicated number of thrusters. Systems that use more than 8 thrusters are limited by their fuel mass fraction, so to increase performance, the specific impulse needs to improve.

***Starshade Launch Vehicle Requirements***

For the less stringent IWA=58 mas requirement, the 56-m starshade for the ATLAST-8m telescope is essentially the same as that for NWO, so it can be accommodated within existing LVs. However, to get the 80-m starshade (IWA=40 mas) into orbit in a single launch, we will require increased fuel capability: the Delta IV Heavy may be needed to lift extra fuel mass. The

## Advanced Technology Large-Aperture Space Telescope (ATLAST)

two biggest challenges in flying the 80-90 meter-class starshades required for *ATLAST* are mass and volume. We estimate we will need a volume upgrade to the Delta IV H in order to launch the *ATLAST* starshades. The current Delta IV H capacity restricts us to ~75-m class starshade if we attempt to fly it using a single launch. If we assume a Delta IV H with a 7-m fairing, we can resolve the volume issue. If we assume two launches for the starshade, and dock (and autonomously assemble) the two components in orbit, we can resolve the mass issue. The latter dual launch can be accomplished using one Delta IV H and one Atlas 551. The Delta IV would carry the starshade assembly and the Atlas 551 would carry its propellant module. An additional 2000 kg of payload mass might be required for docking hardware and fuel. If the launch mass for the Delta IV H was improved from 9000 kg to about 14000 kg, a single launch option is possible for the 90-m starshade (assuming also that the fairing has a 7-m diameter). Two docking and assembly locations are possible: SE-L2 or Cis-lunar.

In conclusion, starshade designs contemplated for 4-m class telescopes scale well to be used with the aperture sizes considered for *ATLAST*. The required technology is a well-understood extension of existing materials and techniques (no “*miracles*” required). The starshade for the 8-meter version of *ATLAST* can be accommodated on existing launch vehicles. The 16-meter version fits well within an Ares V launch vehicle and might be launched on upgraded versions of existing launchers. Lower density material and lower mass deployable mechanisms might enable larger starshades on existing launch vehicles.

## Appendix M: Exoplanet Science with *ATLAST* 8-m and 16-m Concepts

With more than 300 known extrasolar planets, there is a general consensus that terrestrial-mass planets should exist around nearby stars and that some will be located in the habitable zone and be capable of supporting life. Spectral signatures of water vapor, molecular oxygen, carbon dioxide, and methane are available in the optical and near-infrared, offering a suitably-designed large telescope the opportunity to search for habitable environments and life [48]. Because the Earth's atmosphere absorbs all these diagnostic spectral lines, creates high sky backgrounds, and is insufficiently stable for ultra-high contrast imaging, ***only large space telescopes can provide the performance needed to study exo-Earths directly.*** NASA has never designed a space telescope mission around the central goal of high contrast imaging; coronagraphs have always been a "requirements afterthought" to general-purpose observatories. In the *ATLAST* study, standing on the foundations laid by the earlier Terrestrial Planet Finder Coronagraph (*TPF-C*) design work, we considered what a large, optimized, coronagraphic space telescope could accomplish in exoplanet science and general astrophysics.

A general-purpose space telescope can be employed in transiting planet studies. While only a tiny fraction of the planets present can be studied in this way, there is an imperative to learn what we can from all such systems that nature presents to us. If sufficient dynamic range and photometric stability were provided for, an *ATLAST*-class telescope would make major contributions to the study of transiting planets identified by other facilities. Precision lightcurves that resolve the presence of rings, moons, or extended atmospheres could be obtained, and well as spectra for strongly-absorbing species such as neutral sodium. However, even the large aperture of *ATLAST* will not gather enough photons to measure the trace species needed to diagnose habitability and life in a transiting terrestrial planet: a month of integration time (spread over hundreds of transits) would be needed to produce  $S/N=10$  transmission spectra of an Earth-sized HZ planet transiting a nearby M star. The primary approach for *ATLAST* exoplanet studies must therefore be spatially-resolved, high contrast spectroscopy.

Several architecture options are available for high contrast imaging with *ATLAST*. Internal coronagraphs are the most technically mature today, but require active wavefront control and high telescope stability. External occulter concepts offer the potential of higher throughputs, but require a second spacecraft and greater operational complexity. Technology requirements for each are discussed elsewhere in this report.

As a guide to future engineering decisions, we conducted a quantitative assessment of the exoplanet science performance of five different *ATLAST* configurations. The five differ in the range of primary mirror size and coronagraph type assumed, which in turn determine the system throughput and inner working angle to which a planet can be imaged. Details on the architecture options are given below. Input to the calculation is the actual list of nearby stars as measured by the Hipparcos satellite; appropriate sky backgrounds, detector noise and dark current; and residual stellar speckles that we assume have been suppressed to  $10^{-10}$  the brightness of the central star. Since spectroscopy is *ATLAST*'s primary exoplanet science goal, we calculate for each star ( $d < 25$  pc) the integration time required to detect an Earth-sized planet in the habitable zone in an  $R=70$  spectral resolution element at  $S/N=10$ . For the internal coronagraphs, complete freedom to roll the telescope to an optimal orientation is assumed. The results (in terms of the number of stars where the above-mentioned spectroscopy could be done in  $\leq 0.5$

## Advanced Technology Large-Aperture Space Telescope (ATLAST)

Msec or 6 days) are shown in Table M-1. An exozodiacal background of 1 zodi equivalent is assumed; all the numbers decrease (particularly for the 8-m apertures) at higher exozodi levels. The Habitable Zone (HZ) radius is 1 AU scaled by the square root of the stellar luminosity.

**Table M-1. The Number of Nearby Stars where the Habitable Zone Radius is Accessible for Exo-Earth Spectroscopy vs. ATLAST Configuration**

Configuration ID	ATLAST Configuration	Number of stars
I	8x6 m elliptical off-axis monolith with proven Lyot Coronagraph	65
II	8 m on-axis monolith with Visible Nulling Coronagraph	47
III	8 m on-axis monolith with Formation-flying External Occultor	240
IV	16 m on-axis segmented with Visible Nulling Coronagraph	319
V	16 m on-axis segmented with Formation-flying External Occultor	603

*Note:* A 4 m telescope and Lyot coronagraph would access the HZ for 9 stars

The minimum number of accessible stars to guarantee exoEarth detections is unknown, pending the results of the *Kepler* mission. Since current astrometric mission concepts only contemplate screening ~100 stars, configurations III., IV., and V. above would have to dedicate large amounts of mission time to searching the additional unscreened stars at multiple epochs. Multiple visits will be needed even in the subset of stars astrometrically identified to host Earth-like planets, as their orbital phases will not be known precisely enough to predict the epochs of maximum elongation. External occultor configurations III. and V. will be limited in the number of stars (and number of epochs per star) they can observe by the fuel supply and transit times needed for repositioning; this is not reflected in the numbers given above.

Despite the uncertainties, it is clear that a suitably designed *ATLAST* telescope will be capable of discovering and characterizing a large number of nearby planetary systems. Giant planets in 1-15 AU orbits will be readily detected, and exozodiacal/exoKuiper dust structures can be studied for the resonant imprints of planets too small or dim to detect any other way. In the brightest and nearest Earthlike planets, synoptic photometry will reveal the planet's rotation period. Color changes over rotational and seasonal timescales may allow the presence of oceans, clouds, continents, and vegetated zones to be inferred.

*ATLAST* CONFIGURATION NOTES AND ASSUMPTIONS FOR EXOPLANET SCIENCE  
PERFORMANCE

The performance assumptions for the five telescope/coronagraph combinations treated in this study are given in Table M-2. The inner working angle (IWA) is calculated for  $3 \lambda / D$  at 0.76 nm wavelength, corresponding to the molecular O<sub>2</sub> A-band biomarker. The reflective, pupil, and mask throughputs correspond to the fraction of total light that persists after losses at multiple reflecting surfaces, pupil stops, and focal plane masks.

**Table M-2. Performance Assumptions for Five *ATLAST* Configurations**

Parameter	<i>ATLAST</i> Configuration				
	I. 8x6 m Lyot	II. 8m VNC	III. 8m Occ.	IV. 16m VNC	V. 16m Occ.
IWA (mas)	59	59	59	30	30
Reflective Throughput	0.75	0.50	0.90	0.50	0.90
Pupil Throughput	0.50	0.50	0.90	0.50	0.90
Mask Throughput	0.50	0.50	1.00	0.50	1.00
Aperture Correction	0.43	0.33	0.75	0.33	0.75

1. A Lyot coronagraph with precision wavefront control is the most technologically ready high-contrast instrument; developments in the JPL High Contrast Imaging Testbed have demonstrated  $10^{-9}$  contrast at  $3\lambda/D$  inner working angle in the visible, for bandpasses now exceeding 10% [49]. A continued development program should lead to a demonstration of  $10^{-10}$  contrast by 2011. A monolithic, off-axis telescope is strongly preferred for the Lyot coronagraph: segmentation and central obscuration produce sharp edges in the pupil whose diffraction must be suppressed by pupil masking, significantly lowering the system throughput. For highly segmented designs, the masking needed to suppress diffraction in support of  $10^{-10}$  contrast is unachievable. For this reason, the JPL *TPF-C* study baselined a monolithic, off-axis telescope primary. *ATLAST* extends this to an 8m circular monolith. However, current estimates indicate that an off-axis 8-m monolith cannot be packaged for launch within the Ares V fairing. For this reason, an 8x6 m off-axis elliptical monolith is selected as the best telescope configuration for a Lyot coronagraph instrument. The telescope must be highly stable against thermal drifts or vibrations that would alter the wavefront on timescales of hours.
2. A circular on-axis monolith is the simplest *ATLAST* 8m telescope configuration. While a Lyot coronagraph could be considered here (with lower throughput than for Configuration I.), a Visible Nulling Coronagraph (VNC; in which the pupil diffraction is nulled out with a

## Advanced Technology Large-Aperture Space Telescope (ATLAST)

sheared version of itself) would suppress the diffraction without masking of the central and spider obscurations. The VNC is a complex coronagraph concept that will require significant development and testbed demonstration to bring it to technical readiness. The telescope stability and wavefront control requirements for the VNC are comparable to those of the Lyot coronagraph.

3. This telescope configuration is the same as in II. above. However, since an external occulter would be used, the stability and optical wavefront requirements would be those of an ordinary telescope.
4. The 16m primary must be segmented due to launch vehicle fairing constraints. Given this, there is no advantage to eliminating pupil obscurations by using an off-axis telescope. The VNC is baselined here with an on-axis telescope, and with the stability and wavefront control requirements common to configurations I. and II. It is unlikely that a segmented primary of this size could be dimensionally controlled to the required accuracy, and thus a high-stroke deformable mirror would be required to clean up the wavefront that is input to the VNC.
5. This is also a 16m segmented on-axis telescope, to be used with an external occulter coronagraph. Like configuration III, simple diffraction-limited performance would be sufficient.

## Appendix N: *ATLAST* Communications and Telemetry Considerations

The data volume estimated for *ATLAST* is in the ballpark of 200 Gbytes/day. This large data volume must be transmitted to Earth from SE-L2, decoded, and stored for analysis. Based on an analysis performed for our study by Roger Linfield of Ball Aerospace, we believe that *ATLAST* data could reliably be transmitted to Earth in the 26 GHz Ka-band. Linfield’s analysis is summarized below. A data rate of approximately 100 Mbits/sec and a daily downlink pass of approximately 3 hours would be required. The most straightforward and least risky approach is to use an on-board high gain antenna of 120 cm diameter, twice the size of the antenna on *JWST*. Such an antenna would reduce the *ATLAST* observing efficiency, due to the need to adjust the antenna pointing either continuously or in steps during a downlink pass. An alternative is to develop a higher power (~200 W output power and 400 – 500 W input power) 26 GHz transmitter. Such a space-qualified transmitter is not currently available, but its use would allow the data downlink with a 60 cm diameter antenna, and the impact on science operations would be minimal.

### The *JWST* telemetry plan

The anticipated *JWST* data volume is ~ 229 Gbits/day, after lossless on-board compression by a factor ~2 (current simulations predict a factor of 1.7). Using a 60 cm diameter telemetry antenna, the data will be transmitted to Earth at 26 GHz carrier frequency (Ka-band) and received by 34-m diameter Deep Space Network (DSN) antennas. The planned data rate is 28 Mbits/s, with options for lower rates of 14 or 7 Mbits/s. A rate of 28 Mbits/s will allow the transmission of 229 Gbits in 2.3 hours (i.e. one DSN pass per day). A value of 2.7 hours is quoted in some documents, perhaps because of some non-science data and overhead (e.g. data headers). All three DSN sites (California, Spain, and Australia) are being equipped with 26 GHz high rate downlink capability, with the last such modification scheduled for October, 2010.

The on-board Ka-band transmitter will have an input power of 111 W and an output RF power of 50 W. Analysis of the link margin [1] predicts a 4 dB margin even under “adverse” weather and elevation angle conditions at the DSN site.

### Enhancements to allow *ATLAST* telemetry

If we assume the same 1.7:1 lossless data compression as for *JWST*, we can shrink the daily *ATLAST* 200 Gbytes (= 1600 Gbits) to 940 Gbits, a factor of 4.1 larger than for *JWST*. There are several possible ways to transmit this daily volume of data to Earth.

#### 1. More DSN time

If we increased the DSN tracking time from 2.7 hours per day (plus overhead setup time) to 11 hours per day, we could transmit the higher data volume. The onboard antenna and electronics, plus the ground system, could remain the same, so no new technology would be needed. However, the DSN loading would increase substantially. In many cases, antennas at two DSN sites would be needed each day, as the spacecraft would drop below the minimum tracking elevation at the first site. ***A large DSN loading for a long duration science mission is not optimal.*** A small increase from the 2.7 hours/day might be acceptable, but we investigate other alternatives.

If we do not increase the DSN time, then we need to transmit data at a higher rate. This will require on-board hardware changes from the JWST telemetry system. I assume that we want the same SNR per bit as for JWST, but with a four times higher bit rate, and a corresponding four times higher RF bandwidth. The noise per bit will be  $\propto \sqrt{BW \cdot t}$ , where  $BW$  is the RF bandwidth and  $t$  is the integration time per bit. The two are inversely related, so their product will be unchanged. For the signal, the integration time will be four times smaller, so we need four times larger power received at the ground. This can be obtained by a four times larger collecting area, or by four times larger effective radiated power (or a combination of the two).

## 2. More DSN collecting area

One 34 m DSN antenna is a substantial resource, and we could not request two except under unusual circumstances. The 70 m antennas cannot support Ka-band telemetry. There has been considerable discussion about building arrays of  $\sim 12$  m diameter, receive-only antennas at the three DSN complexes. Such arrays could potentially give larger effective collecting area than a 34 m antenna in a cost-effective manner. Unfortunately, NASA has shelved plans for a possible DSN array, due to the required capital construction costs. *We should not count on more collecting area than a single 34-m DSN antenna.*

## 3. More downlink power

If we could increase the transmitter power by a factor of four, we could achieve the higher data rate. One drawback is that the required electrical input power would increase to approximately 500 W. A second drawback is the lack of technical maturity for a long-life (5 – 10 years) high power transmitter at 26 GHz designed to operate in space. There has been a 200 W (output power) 32 GHz transmitter developed for potential space use [58]. This development effort suggests that a suitable 26 GHz transmitter could be designed and built for use by *ATLAST*.

## 4. More downlink gain

If we doubled the diameter of our high gain telemetry antenna to 120 cm, the gain would increase by a factor of four, and the power received on the ground would increase by the same factor. The technical maturity of such an on-board antenna is very high (Voyager has a 3.7 m diameter high gain antenna, and Cassini has a 4 m antenna). The pointing requirement is definitely achievable: 10% of the full beamwidth of a 120 cm antenna at 26 GHz is about 3 arcminutes. *A larger downlink antenna is the preferred solution for the ATLAST telemetry challenge.*

### Potential concerns with this proposed solution

Although the SNR scaling works for the proposed *ATLAST* solution, there are three obvious concerns.

1. **The four times larger downlink rate (compared to *JWST*) requires a four times larger RF bandwidth. Can we get the required frequency allocation?**

The international frequency allocation table (accessible on the FCC website [59]) states that the 25.5 – 27.0 GHz band is for space-to-Earth use. The proposed ~100 Mbit/s downlink poses no conflict with the allocation spectrum. The Lunar Reconnaissance Orbiter (*LRO*) plans to downlink 100 Mbit/s to a ground station in White Sands, NM [60], with information on the *LRO* website [61] stating that the spacecraft has 100 – 300 Mbit/s Ka-band downlink capability. It would appear that we could get the frequency allocation.

## **2. Can DSN antennas and data systems handle this large bit rate?**

The three DSN antennas being equipped for *JWST* downlink can definitely handle 28 Mbit/s. Can they handle a larger data rate? Linfield was not able to confirm that they can currently do this. However, the capability is at least nearly ready. An official DSN document [62] states that the 26 GHz IF (i.e. after down-conversion) is connected directly to a high-rate telemetry receiver. Therefore, the front-end electronics of the antenna are almost certainly compatible with a 100 Mbit/s rate. A published paper [63] mentions the “IN-SPEC Cortex” digital receiver, which can handle data rates up to 2 Gbits/s and is “under consideration” by the *JWST* Project. A DSN research paper from 2006 [64] describes a design for a telemetry receiver capable of handling data rates >150 Mbits/s. Clearly, the technology is mature and the DSN is looking into implementing it. It could be available for *ATLAST* with advanced planning and perhaps some additional funding. *LRO* is planning to use at least 100 Mbit/s, and perhaps up to 300 Mbit/s downlink at 26 GHz with a White Sands antenna, so there already exists at least one ground station that could handle *ATLAST* data.

## **3. What are the consequences of the smaller beamwidth of a 120 cm on-board antenna, compared to the 60 cm antenna of *JWST*?**

Pointing a 120 cm Ka-band antenna to <10% of its 30 arcminute beam width is easily within current technology. However, there is a problem. The plan for *JWST* is to slew the downlink antenna just before a telemetry pass and fix its position for the entire pass [65]. The motivation is to avoid disturbing the telescope pointing during science observations. With the distance and dynamics of the L2 halo orbit, the maximum pointing error will be 0.4°, leading to a 1.5 dB SNR loss. With a 120 cm antenna, the corresponding SNR loss from pointing would be ≈6 dB. Another approach to antenna pointing would be needed. Since the required pointing stability of *ATLAST* is several times more stringent than for *JWST* (due to a larger aperture and shorter observing wavelengths), we assume that antenna motion during science observations is not possible. We could halt science operations during downlink (clearly undesirable, but feasible). We could schedule short (~1000 – 2000 sec) observations during the downlink, and step the antenna pointing before each of these short observations.

If it should prove feasible to achieve the four times higher downlink rate (relative to *JWST*) by increasing the transmitter output power to 200 W, then a 60 cm antenna could be used, and the antenna pointing could be fixed during an entire downlink pass. In this case, the observing efficiency would not be significantly affected by downlink operations.

### **Additional option 1: Phased array on-board antenna**

If the downlink antenna were a phased-array, it would not need to be physically steered during a tracking pass. However, the number of elements in such an array would be prohibitive. Very roughly, you want one element every half-wavelength in a two-dimensional array. For our 26 GHz frequency (1.15 cm wavelength) and a 120 cm diameter array, ~30,000 elements would be needed. Each element would need its own electronics, including a 26 GHz transmitter. *We believe a phased-array is not a feasible option for ATLAST.*

#### **Additional option 2: Optical (laser) communication**

Optical communication (using lasers) has been considered for future space communications. The available bandwidth is far greater than in the RF, so the fundamental telemetry rate limit is much greater. For some Earth orbit to ground communications applications, the desired telemetry rate is greater than the available RF allocation bandwidth, and optical comm. is the only option. For *ATLAST*, we will not be limited by radio frequency allocation. Therefore, we would only consider optical comm. if it had advantages in cost and risk, in comparison to RF telemetry. Estimating the cost of optical comm. from L2 is difficult, since optical comm. is not currently being done beyond Earth orbit. It took approximately 30 years, starting in the late 1970s, for the DSN to advance from X-band (8 GHz) to Ka-band (25 – 35 GHz) for operational space missions. The benefits of Ka-band were obvious, and the technologies to transmit and receive Ka-band signals, plus to point antennas, were in hand in the 1970s. Major change happens very slowly in the DSN. The change from Ka-band to optical comm. is much more drastic than from X-band to Ka-band, and the DSN has not committed to optical comm. for any future space mission beyond Earth orbit. *It would be unwise to plan for optical (laser-based) communications for ATLAST.*

## Appendix O: Servicing Benefits for *ATLAST*

An architecture that enables in-space servicing is compatible with long-range goals of achieving larger and more capable observatories in the future. There are four specific examples of on-orbit servicing that will benefit *ATLAST*:

1. Replenishment of expendables. The two most familiar commodities are fuel for maneuvering or station-keeping, and cryogenic fluids or solids for cooling. Refilling the tank periodically will keep the mission alive.
2. Replacement of limited-lifetime items. Many of the “utilities”, such as solar arrays, batteries, gyroscopes and reaction wheels tend to wear out after several years of operation in the space environment. Their demise may be predictable, or can be anticipated by observing a deterioration of their performance. Replacing them with fresh units restores the full capabilities.
3. Replacement of degraded or failed components. Components may also fail because of isolated events such as radiation damage to electronics, failure of a solder joint or printed circuit, particulate interference with a mechanism or contamination of a thermal control surface. Again, replacing the troublesome items may restore full performance.
4. Upgrading with newer technology. *ALAST* is being conceived many years before it will be built. Many of the critical subsystems contain technologies that are considered adequate and low risk now, but whose performance will be surpassed by subsequent generations of devices. Examples of technological opportunities include entire instruments, focal plane arrays, cryo-coolers, guidance sensors, computers and memory modules.

Servicing will be most productive and cost-effective if it is part of the design philosophy from the beginning. To enable future servicing, either by human crews or by robotic agents, the interfaces between the service provider and recipient need to be defined, documented and agreed to, and built into the system from the start.

Designing for serviceability will have benefits during the pre-launch development and testing. The system will feature modularity, accessibility and clean interfaces. A system designed to be a cooperative recipient of servicing will have clear markings, navigation and metrology aids, hand holds and safe attachment points. While intended to enable in-orbit replacement, this partitioning will also provide flexibility in procurement strategies, assembly sequences and system-level integration and test.

A mission intended to be serviced in space may be simpler to design, build and test. It may be acceptable for expendable resources that will be replenished to have less margin to begin with. Subsystems that will be replaced after  $n$  years may use a different approach to reliability and redundancy than those required to last  $2*n$  years. Single string systems may be acceptable in cases where normal practice would require dual string architectures.

The assurance of servicing high-value, long-lived space systems (like *ATLAST*) after launch may enable savings in mass, complexity, testing, development time and cost.

# Advanced Technology Large-Aperture Space Telescope (ATLAST)

## References

- [1] Kasting, J. et al., “*Exoplanet Characterization and the Search for Life*,” Astro2010 Science White Paper, [NRC Astro2010 SWP Website](#)
- [2] Lunine, J. I., et al., 2008, arXiv:0808.2754
- [3] Des Marais, D. J., et al. 2002, *Astrobiology*, 2, 153
- [4] Woolf, N. J., Smith, P. S., Traub, W. A., & Jucks, K. W. 2002, *ApJ.*, 574, 430
- [5] Seager, S., Turner, E. L., Schafer, J., & Ford, E. B. 2005, *Astrobiology*, 5, 372
- [6] Ford, E. B., Seager, S., & Turner, E. L. 2003, *Scientific Frontiers in Research on Extrasolar Planets*, 294, 639.
- [7] Birnboim, Y., & Deckel, A. 2003, *MNRAS* 345, 349
- [8] Keres, D., et al. 2003, *MNRAS*, 363, 2
- [9] Cen, R., & Ostriker, J.P. 2006, *ApJ*, 650, 560.
- [10] Jimenez, R. et al., 2008, arXiv:0811.4134
- [11] Sembach, K. et al., “*The Cosmic Web*,” Astro2010 Science White Paper, [NRC Astro2010 SWP Website](#)
- [12] Bertone, S., Schaye, J., & Dolag, K. 2008, *Space Science Reviews*, 134, 295.
- [13] Giavalisco, M. et al., “*The Quest for a Physical Understanding of Galaxies Across Cosmic Time*,” Astro2010 Science White Paper, [NRC Astro2010 SWP Website](#)
- [14] Sembach, K. et al., “*Technology Investments to Meet the Needs of Astronomy at Ultraviolet Wavelengths in the 21st Century*,” Astro2010 Technology Development White Paper.
- [15] Calzetti, D. et al., “*Is the Initial Stellar Mass Function Universal?*”, Astro2010 Science White Paper, [NRC Astro2010 SWP Website](#)
- [16] Brown, T. et al., “*The History of Star Formation in Galaxies*,” Astro2010 Science White Paper, [NRC Astro2010 SWP Website](#)
- [17] Mountain, M. et al., “*Optical Astronomy: The Prospects for Ground-Based AO and Space-Based Observations in the coming Decades*,” Astro2010 Technology Development White Paper.
- [18] Berkefeld, T., Glindemann, A., and Hippler, S., *Exp. Astron.*, **11**, 1–21 (2001).
- [19] Andersen, D., et al. , *PASP*, **118**, 1574–1590 (2006).
- [20] Ammons, S.M., et al. , *Proc. SPIE*, **6272**, (2006).
- [21] H. P. Stahl, P. Sumrall, and R. Hopkins, “*Ares V Launch Vehicle: an Enabling Capability for Future Space Science Missions*”, Acta Astronautica Elsevier Ltd., 2009, doi:10.1016/j.actaastro.2008.12.017
- [22] Hickey, G. S., Lih, S.-S., Barbee, T. W., Jr., 2002, *SPIE*, 4849, 63. (“*Development of Nanolaminate Thin Shell Mirrors*”)
- [23] D. Redding, P. Eisenhardt, G. Hickey, K. Stapelfeldt, W. Traub, M. Werner, “*Active Optics for a 16-Meter Advanced Technology Large Aperture Space Telescope (ATLAST)*,” *SPIE* 7010 (2008).
- [24] Strafford, D. N., DeSmitt, S. M., Kupinski, P. T., & Sebring, T. A., 2006, *SPIE*, 6273, 0R. (“*Development of Lightweight, Stiff, Stable, Replicated Glass Mirrors for the Cornell Caltech Atacama Telescope (CCAT)*”)
- [25] Werner, M. et al., “*Active Space Telescope Systems – A New Paradigm*,” Astro2010 Technology Development White Paper.
- [26] Levine, M. et al., “*Overview of Technologies for Direct Optical Imaging of Exoplanets*,” Astro2010 Technology Development White Paper.
- [27] *Space Mission Analysis and Design*, ed. J. Wertz and W. Larson, Kluwer Academic Publishers, 1991, pp. 314-315
- [28] Patrick Jelinsky, SNAP Reaction Wheel Size, 12/20/2004, p. 5, <http://snap.lbl.gov/pub/bscw.cgi/S49d0b4a1/d118194/SNAP-TECH-04025.doc>
- [29] Bong Wie, *Space Vehicle Dynamics and Control*, AIAA Education Series, 1998, pp. 419-422.
- [30] U.S. Patent 7,270,304 B2, “*Isolating Positioning Boom for Instrument Platforms*”, granted September 18, 2007.
- [31] Martin, N. F., Iyata, R. A., Chapman, S. C., Irwin, M., & Lewis, G. F. 2007, *MNRAS*, 380, 281.
- [32] Simon, J. D., & Geha, M. 2007, *ApJ*, 670, 313.
- [33] Strigari, L. E., Bullock, J. S., Kaplinghat, M., Simon, J. D., Geha, M., Willman, B., & Walker, M. G. 2008a, *Nature*, 454, 1096.
- [34] Strigari, L. E., Bullock, J. S., & Kaplinghat, M. 2007a, *ApJ*, 657, L1.
- [35] B. H. Dean, D. L. Aronstein, J. S. Smith, R. Shiri, and D. S. Acton, “*Phase Retrieval Algorithm for JWST Flight and Testbed Telescope*,” *Proc. SPIE* **6265**, 626511 (2006)
- [36] M. G. Löfdahl, R. L. Kendrick, A. Harwit, K. E. Mitchell, A. L. Duncan, J. H. Seldin, R. G. Paxman, and D. S. Acton, *Proc. SPIE* **3356**, 1190 (1998).
- [37] B. H. Dean & C. W. Bowers, “*Diversity selection for phase-diverse phase retrieval*,” *JOSA A* **20**, 1490 (2003).

- [38] David C. Redding, Norbert Sigrist, J.Z. Lou, Y. Zhang, P. Atcheson, S. Acton, W. Hayden, "Optical State Estimation Using Wavefront Data," Proc. SPIE 5523 (2004).
- [39] Fang Shi, Scott A. Basinger, and David C. Redding, "Performance of dispersed fringe sensor in the presence of segmented mirror aberrations: modeling and simulation," Proc. SPIE 6265 (2006).
- [40] Fang Shi, Catherine Ohara, Gary Chanan, Mitchell Troy, and David Redding, "Experimental Verification of Dispersed Fringe Sensing as a Segment Phasing Technique Using the Keck Telescope," Applied Optics, vol. 43, 4474 – 4481 (2004).
- [41] David Redding, Scott A. Basinger, Sidd Bikkannavar, David Cohen, Joseph J. Green, Catherine Ohara and Fang Shi, "How Defocused Images Are Used To Measure Phase: An Explanation of the Modified Gerchberg-Saxton Phase Retrieval Software," Technical Support Package, JPL New Technology Report, NPO 43857 (2007).
- [42] J. Green, S. Basinger, D. Cohen, A. Neissner, D. Redding, S. Shaklan and J. Trauger, "Demonstration of Extreme Wavefront Sensing Performance on the TPF High Contrast Imaging Testbed," Proc. SPIE 5170 (2003).
- [43] C. Ohara, S. Basinger, D. Cohen, J. Faust, J. Green, A. Lowman, D. Redding, F. Shi, "Phase Retrieval Camera Optical Testing of the Advanced Mirror System Demonstrator," SPIE 5487 (2004).
- [44] John Z. Lou, David Redding, Norbert Sigrist and Scott Basinger, "Adaptive Telescope Multi-Field Wavefront Control with a Kalman Filter," SPIE Astronomical Instrumentation, Marseille (2008).
- [45] Erkin Sidick, Scott A. Basinger, and David C. Redding, "An Improved Wavefront Control Algorithm for Large Space Telescopes," SPIE Astronomical Instrumentation, Marseille (2008).
- [46] Shelton, C., Mast, T., Chanan, G., Nelson, J., Roberts, L., Troy, M., Sirota, M., Byoung-Joon Seo, MacDonald, D., "Advances in Edge Sensors for the Thirty Meter Telescope Primary Mirror," Proc. SPIE 7012-35 (2008).
- [47] Argabright, V., et al, Proc. SPIE, **7010**, 70102L (2008)
- [48] Traub, W. et al. 2009, Response to Request for Information (RFI) to *Astro2010*, the Astronomy and Astrophysics Decadal Survey
- [49] Trauger, J. & Traub, W. 2007, Nature 446, 771
- [50] Kuchner & Traub, ApJ, 570, 900 (2002)
- [51] Kuchner et al., ApJ, 628, 466 (2005)
- [52] Moody et al., Proc. SPIE, 7010, 70103P (2008)
- [53] Yaitskova, Proc. SPIE, 5905, 292 (2005)
- [54] Mawet et al., Proc. SPIE, 6693, 66931M (2007).
- [55] Guyon et al., ApJ, 622, 744 (2005)
- [56] Vanderbei, ApJ, 636, 538 (2006)
- [57] Codona, Proc. SPIE, 5490, 379 (2004).
- [58] "High Power and Efficiency Space Traveling-Wave Tube Amplifiers With Reduced Size and Mass for NASA Missions," R. N. Simons, J. D. Wilson, and D. A. Force, NASA/TM-2008-215220, <http://www.docstoc.com/docs/895827/High-Power-and-Efficiency-Space-Traveling-Wave-Tube>
- [59] Federal Communications Commission Radio Spectrum Home Page, [www.fcc.gov/oet/spectrum](http://www.fcc.gov/oet/spectrum)
- [60] "Mission Design and Operations Considerations for NASA's Lunar Reconnaissance Orbiter," M. B. Houghton, C. R. Tooley, and R. S. Saylor, Jr. [http://lunar.gsfc.nasa.gov/library/IAC-07-C1\\_7\\_06.pdf](http://lunar.gsfc.nasa.gov/library/IAC-07-C1_7_06.pdf)
- [61] <http://lunar.gsfc.nasa.gov/spacecraft.html>
- [62] <http://deepspace.jpl.nasa.gov/dsndocs/810-005/206/206A.pdf>
- [63] M. K. Cheng, M. Lyubarev, M. A. Nakashima, K. S. Andrews, and D. Lee, "Integrated Performance of Next Generation High Data Rate Receiver and AR4JA LDPC Codec for Space Communications," *AIAA SpaceOps 2008*, Heidelberg, Germany, May 12-16, 2008.
- [64] "Real-Time Wideband Telemetry Receiver Architecture and Performance," K. Andrews, J. Gin, N. Lay, K. Quirk, and M. Srinivasan, Aug. 15, 2006. [http://tda.jpl.nasa.gov/progress\\_report/42-166/166H.pdf](http://tda.jpl.nasa.gov/progress_report/42-166/166H.pdf)
- [65] "Lunar, L1, and L2 – A Communications guide based on the James Webb Space Telescope experience," J. Gal-Edd, B. Seaton, C. Fatig, and A. Johns, paper AIAA 2006-5787, SpaceOps 2006 Conference.
- [66] R. Bredthauer, private communication.
- [67] M. Sirianni and M. Mutchler, "Radiation damage in Hubble CCDs," in Scientific Detectors for Astronomy 2005, Ed. J.E. Beletic, J.W. Beletic, and P. Amico pp. 171-178 (Springer; Dordrecht;2006)
- [68] R. Howard, B. Au, private communication.
- [69] P. Jarrem, et al., "The LLCCD: low light imaging without the need for and intensifier," Proc. SPIE 4306. pp 178-186, 2001.

## Advanced Technology Large-Aperture Space Telescope (ATLAST)

- [70] E2v CCD data sheet, <http://www.e2v.com/products/imaging-devices/space---scientific-imaging/capabilities-and-technical-information/>.
- [71] Low Light Tech Note 4, e2v, "Dark signal and clock-induced charge," <http://www.e2v.com/products/imaging-devices/l3vision-cameras---sensors/datasheets-and-technical-papers/>.
- [72] Low light Tech Note 5, "An overview of the Aging Characteristics of L3Vision™ sensors," <http://www.e2v.com/products/imaging-devices/l3vision-cameras---sensors/datasheets-and-technical-papers/>.
- [73] J. Hyneczek, "Impactron – a new solid state image intensifier," IEEE Trans on Electron Dev., ED-48, pp 2238-2241, Oct. 2001.
- [74] J. Hyneczek and T. Nishiwaki, "Excess noise and other important characteristics of low light level imaging using charge multiplying CCDs," IEEE Trans. on Electron Dev., ED-50, pg 239-245, Jan. 2003.
- [75] J. Janesick, J. Andrews and T. Elliott, "Fundamental performance differences between CMOS and CCD imagers; Part I," Proc. SPIE 6276, paper 6276-77 (Orlando, 2006).
- [76] J. Bogaerts et al., "Total Dose and Displacement Damage Effects in a Radiation Hardening CMOS APS", (Trans Electron Devices, ED-50, pp 84-90, 2003).
- [77] S.E. Holland, "Fully depleted, back-illuminated charge-coupled devices fabricated on high-resistivity Silicon," Trans. Electron Devices, ED-50, pp.225-238 (2003)
- [78] B. Burke et al., "Development of the Orthogonal-Transfer Array", Proc. SPIE 6068 J-1 (2006).
- [79] J. Janesick, "Scientific Charge-Coupled Devices", SPIE Press Monograph Vol. PM 83 (2001).
- [80] M. Sirianni et al., "Performance of the Advanced Camera for Survey CCDs after two years on orbit", Proc. SPIE 5499, 173 (2004).
- [81] <http://www.itrs.net/reports.html>, 2007 Edition.